Additional production of deuterium and helium-3 by high-energy protons and antiprotons in the early Universe

E. V. Sedel'nikov

Institute of Mathematical Modeling, Russian Academy of Sciences, 125047 Moscow, Russia

(Submitted 23 March 1999)
Pis'ma Zh. Éksp. Teor. Fiz. **69**, No. 9, 609–613 (May 1999)

The results of calculations of ^{3}He, ^{3}H, and D production as a result of the disintegration of primordial ^{4}He by high-energy protons and antiprotons in the early Universe are reported. It is shown that for primary particle energies $E_{p,\bar{p}} > 0.2$ GeV the main role in ^{3}He, ^{3}H, and D production is played by the secondary proton cascade that develops in the cosmological plasma and which destroys ^{4}He most intensively at $E \sim 75$ MeV. At the current state of the experimental data one can calculate the number of nuclei produced to within 10%, and investigation of the inelastic p^4He interaction channels at $E \sim 75$ MeV will make it possible to improve substantially the accuracy of calculations of the additional production of light elements. © *1999 American Institute of Physics.* [S0021-3640(99)00109-7]

PACS numbers: 26.35.+c, 98.80.Ft, 25.40.Ep, 27.10.+h, 25.43.+t

The additional production of the nuclei of light elements in the interaction of high-energy protons and antiprotons with the cosmological plasma produced during primordial nucleosynthesis is being studied in the literature in connection with the possibility of placing limits on the density of sources of such particles associated with the (hypothetical) physics of the very early Universe. Thus the requirement that the amount of D and ^{3}He produced not exceed their observed abundance in the present-day Universe makes it possible to obtain limits on the parametersof the grand unification models,[1] and on the density of primordial black holes.[2] The investigation of the possible evolution of the chemical composition in the early Universe is also of independent interest for cosmology.

A high-energy proton (antiproton) interacting with a plasma initiates secondary hadron and electromagnetic cascades in the plasma. The additional production of ^{3}He, ^{3}H, and D as a result of the disintegration of primordial ^{4}He by an electromagnetic cascade has its own complicated and specific character and can serve to tighten the limits on the particle sources. This is a subject for a separate paper.

Continuing the investigation of nonequilibrium cosmological nucleosynthesis (NCN) in the early Universe with the participation of nucleons,[3] this letter reports the results of calculations using a more complicated model reflecting the current state of the experimental data. (In the present case nonequilibrium means that the energy of the particles that break up ^{4}He is much greater than the average thermal energy of the equilibrium particles in the cosmological plasma.)

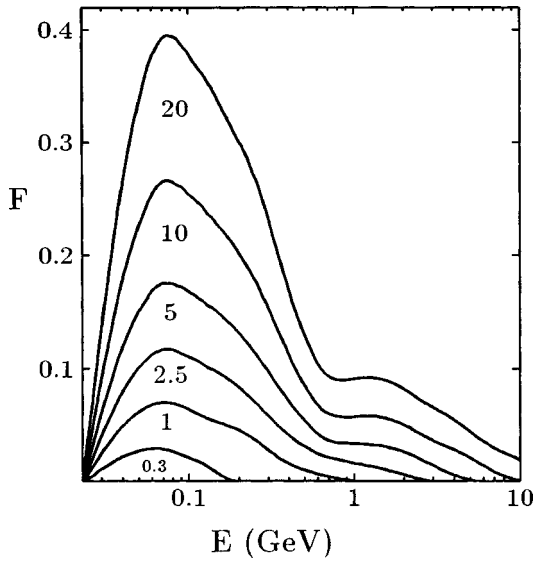

FIG. 1. The factor $f_p[\sigma^{\rm inel}_{p^4{\rm He}} n_{^4{\rm He}}/\Sigma^{\rm tot}_p]$, determining the intensity of ^{4}He disintegration by a proton-initiated secondary cascade. The numbers beneath the curves are the energy of the primary proton, in GeV.

We are studying a uniform cosmological plasma consisting of hydrogen and helium-4 nuclei and electrons ($n_{^4{\rm He}} = 0.1 n_{^1{\rm H}}, n_e = n_{^1{\rm H}}$). The primordial ^{4}He is disintegrated by the primary particle and by the secondary proton cascade initiated by the primary particle. The energy distribution of the protons in the secondary cascade is described by the function f_p ($f_{\bar{p}}$) such that $\int f_{p(\bar{p})} dE$ is the total number of nonequilibrium secondary protons produced by the primary proton (antiproton). The number of nuclei of the element A (^{3}He, ^{3}H, or D) produced by a secondary proton cascade initiated by a proton can be expressed as

$$n_{\rm A} = \int f_p \frac{\sigma_{p^4{\rm He}\to {\rm AX}} n_{^4{\rm He}}}{\Sigma^{\rm tot}_p} dE = \int f_p \frac{\sigma^{\rm inel}_{p^4{\rm He}} n_{^4{\rm He}}}{\Sigma^{\rm tot}_p} \frac{\sigma_{p^4{\rm He}\to {\rm AX}}}{\sigma^{\rm inel}_{p^4{\rm He}}} dE,$$

where $\Sigma^{\rm tot}_p$ is the total macroscopic proton–plasma interaction cross section, viz.,

$$\Sigma^{\rm tot}_p = [\sigma^{\rm tot}_{pp} + \sigma_{\rm Coulomb}] n_{^1{\rm H}} + [\sigma^{\rm tot}_{p^4{\rm He}}] n_{^4{\rm He}},$$

and similarly for an antiproton with f_p replaced by $f_{\bar{p}}$.

The amount of primordial ^{4}He disintegrated by the cascade is proportional to the product $f_p[\sigma^{\rm inel}_{p^4{\rm He}} n_{^4{\rm He}}/\Sigma^{\rm tot}_p]$. This product as a function of the secondary-proton energy is displayed in Fig. 1 for a number of values of the primary proton energy. For an antiproton-initiated cascade the form of the curves $f_{\bar{p}}[\sigma^{\rm inel}_{p^4{\rm He}} n_{^4{\rm He}}/\Sigma^{\rm tot}_p]$ is essentially identical, but the cascade is less energetic (a substantial fraction of the energy goes into the annihilation channel). One can see from Fig. 1 that the secondary proton cascade destroys ^{4}He most intensively in the energy range $E_p \approx 60$–100 MeV (this is also valid for an antiproton-initiated cascade).

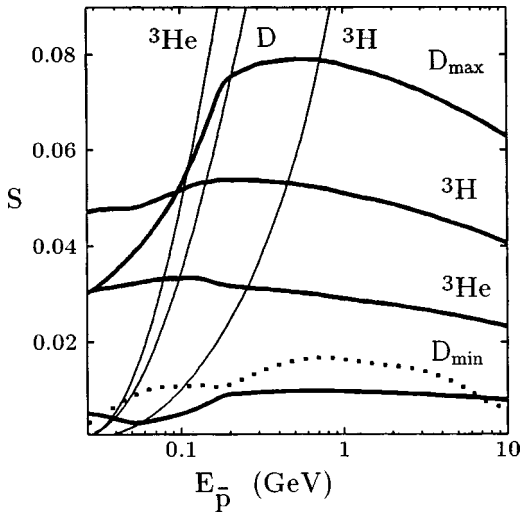

FIG. 2. Amount of ^{3}He, ^{3}H, and D nuclei additionally produced by a primary antiproton (thick lines) and by the proton cascade initiated by the primary antiproton (thin lines) as a function of the antiproton energy. The amount of deuterium produced in the reaction $\bar{p}^4$He $\rightarrow$ DX is shown for the minimum D_{min} and maximum D_{max} estimates of the D yield in $\bar{p}^4$He annihilation.[4] The dotted line shows the amount of ^{3}He nuclei produced in the reaction $\bar{p}^4$He $\rightarrow \bar{p}^3$HeX.

For studying the relation between the contributions to the additional production of ^{3}He, ^{3}H, and D from the primary particle itself and from the secondary proton cascade which it initiates, the antiproton case is more important — see Fig. 2. In explanation of the figure, it should be mentioned that experimental data on the yield of fragments in $\bar{p}^4$He annihilation exist only for ^{3}He, that the tritium yieldcan be estimated with a large error by making additional assumptions, and that the the estimated deuterium yield varies over very wide limits.[4] Tritium decays with a half-life $\sim$12 yr into ^{3}He. For $E_{\bar{p}} > 100$ MeV the production of ^{3}He + ^{3}H by the secondary cascade starts to exceed the ^{3}He + ^{3}H production due to the annihilation of the primary antiproton. For $E_{\bar{p}} > 40$ MeV the production of deuterium by the secondary cascade exceeds the minimum estimate of D production by $\bar{p}^4$He annihilation, and for $E_{\bar{p}} > 0.2$ GeV it exceeds the maximum estimate. The inelastic nonannihilation $\bar{p}^4$He interaction does not play a large role anywhere in the energy range.

On the whole, the existing experimental data for the $\bar{p}^4$He interaction are inadequate for constructing a reliable model of the additional ^{3}He + ^{3}H and D production in NCN processes initiated in the early Universe by antiprotons with energy $E_{\bar{p}} < 0.2$ GeV.

Models of $\bar{p}^4$ He annihilation, with additional theoretical assumptions made in order to estimate the ^{3}H and D yields, are being discussed in the literature (see, for example, Ref. 5). Such an estimate is especially important for the problem of annihilation of antimatter in the early Universe. Annihilation occurs at thermal energies, and the secondary cascade can be completely neglected. The yield of ^{3}He, ^{3}H, and D will be determined directly by the yield of these fragments in the annihilation channel of the $\bar{p}^4$He interac-

tion. The Coulomb interaction and, after recombination of the Universe, the radiative capture and rescattering by nuclear bound states[6] play an important role in the annihilation of slow antiprotons, greatly increasing the total annihilation cross section. The Coulomb interaction increases the percentage of annihilations on helium nuclei, and this increases interest in the experimental investigation of the ^{3}H and D yield in $\bar{p}^4$He annihilation.

If the primary particle is a proton, then up to energies $E_p \sim 0.25$ GeV the production of ^{3}He + ^{3}H and D occurs mainly through the disintegration of ^{4}He by the primary proton itself. Disintegration by a secondary proton cascade dominates at higher energies.

At energies where the production is due to a secondary cascade (or, in the case when the primary particle is a proton, at arbitrary energies), the model makesit possible to calculate to within 8–10% the number of ^{3}He, ^{3}H, and D nuclei additionally produced in NCN processes. Because of a lack of reliable experimental data for $E_p < 0.2$ GeV, this computational accuracy is determined by the variations in the estimated cross sections for the inelastic $\bar{p}^4$He interaction channels. The experimental data on inelastic p^4He interaction channels were discussed in detail in a 1972 review.[7] For $E_p < 0.2$ GeV the situation remains essentially the same as it was then. However, as is clear from Fig. 1, this range is the most important for NCN. In this connection attention should be turned to the method developed at The Institute of Theoretical and Experimental Physics (Moscow) and the Joint Institute of Nuclear Research (Dubna) for working with accelerated ^{4}He nuclei bombarding a proton target. This method will make it possible to distinguish the inelastic p^4He interaction channels efficiently. The experimental data[8,9] obtained using this method make it possible to fit reliably the cross sections for inelastic p^4He interaction channels for $E_p > 0.2$ GeV.

The total amount of additional ^{3}He + ^{3}H and D produced (by the primary particle and by the secondary cascade) is shown in Fig. 3. The number of nuclei produced by the proton is presented as bands in accordance with the computational accuracy indicated above. Similarly, the amount of ^{3}He + ^{3}H produced by an antiproton is shown as a band of possible energies. The experimental data on the ^{3}He yield and the minimum and maximum estimates of the ^{3}H yield in $\bar{p}^4$He annihilation were used in the calculation; the calculation of deuterium production by an antiproton is presented by two curves: for the minimum (D_{min}) and maximum (D_{max}) estimate of the D yield in the $\bar{p}^4$He annihilation channel.[4]

An estimate of the ratio $S_D/(S_{^3He+^3H})$ of the amount of deuterium produced in NCN to the total amount of helium-3 and tritium produced is very interesting for cosmological applications. At energies where the disintegration of ^{4}He is due to the secondary proton cascade it can be estimated that $S_D/(S_{^3He+^3H}) = 0.55 \pm 0.08$. In the case of a primary proton, as its energy decreases this ratio approaches 1, since in the near-threshold energy range the reaction $p^4\mathrm{He} \rightarrow \mathrm{D}^3\mathrm{He}$ dominates in the inelastic p^4He interaction. For the annihilation of slow protons it can only be said that the total ^{3}He + ^{3}H production is greater than the production of D.

The following problems are important for further refinement of the model: 1) investigation of inelastic p^4He interaction channels by the method of accelerated ^{4}He nuclei with energy $E_p \sim 75$ MeV, and 2) the experimental determination of the ^{3}H and D yields in $\bar{p}^4$He annihilation, which falls outside the scope of our needs here. From the standpoint

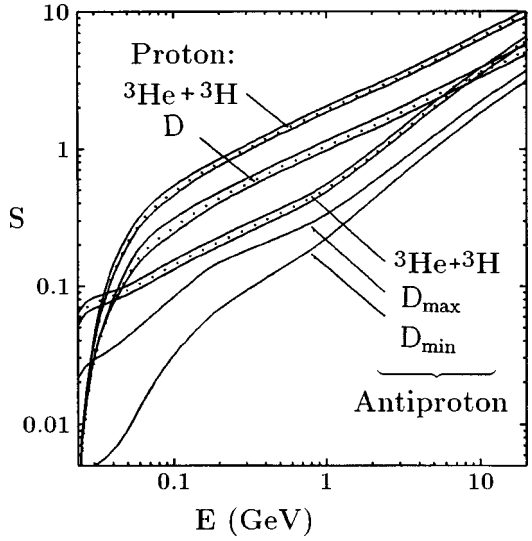

FIG. 3. Total amounts of ^{3}He + ^{3}H and D nuclei additionally produced (by the primary particle and by the secondary cascade) in NCN by a proton and antiproton as a function of their energy.

of the present investigation, the energy range $E_{\bar{p}} < 0.2$ GeV is of primary interest; specifically, for the problem of annihilation of antimatter in the Universe it is especially important to investigate $\bar{p}^4$He annihilation at rest.

I thank M. Yu. Khlopov, L. A. Kondratyuk, and V. I. Kukulin for a helpful discussion, I. M. Sobol', whom I consultated concerning the Monte Carlo method used, and Yu. L. Levitan for his interest in this work.

[1] M. Yu. Khlopov and V. M. Chechetkin, Fiz. Elem. Chastits At. Yadra **18**, 627 (1987) [Sov. J. Part. Nucl. **18**, 267 (1987)]; M. Yu. Khlopov and A. D. Linde, Phys. Lett. B **138**, 265 (1984); V. M. Chechetkin, M. Yu. Khlopov, M. G. Sapozhnikov, and Ya. B. Zeldovich, Phys. Rev. Lett. **118**, 329 (1982); V. M. Chechetkin, M. Yu. Khlopov, and M. G. Sapozhnikov, Riv. Nuovo Cimento **5**, 1 (1982).
[2] Ya. B. Zel'dovich, A. A. Starobinskiĭ, M. Yu. Khlopov, and V. M. Chechetkin, Pis'ma Astron. Zh. **3**, 208 (1977) [Sov. Astron. Lett. **3**, 110 (1977)]; E. V. Sedel'nikov, Pis'ma Astron. Zh. **12**, 889 (1996) [Astron. Lett. **22**, 797 (1996)].
[3] Yu. L. Levitan, I. N. Sobol', M. Yu. Khlopov, and V. M. Chechetkin, Yad. Fiz. **47**, 168 (1988) [Sov. J. Nucl. Phys. **47**, 109 (1988)]; M. Yu. Khlopov, Yu. L. Levitan, E. V. Sedel'nikov, and I. M. Sobol', Yad. Fiz. **57**, 1466 (1994); E. V. Sedel'nikov, S. S. Filippov, and M. Yu. Khlopov, Yad. Fiz. **58**, 280 (1995); E. V. Sedel'nikov, Yu. L. Levitan, and I. M. Sobol', IMM RAN Preprint No. 1 [in Russian], Institute of Mathematical Modeling, Russian Academy of Sciences, Moscow (1996).
[4] F. Balestra, S. Bossolasco, M. P. Bussa *et al.*, Nuovo Cimento A **100**, 323 (1988).
[5] A. A. Sibirtsev, Yad. Fiz. **55**, 965 (1992) [Sov. J. Nucl. Phys. **55**, 541 (1992)]; Y. Sakamoto *et al.*, Nucl. Phys. B **8**, 271 (1989); V. I. Nazaruk, Yad. Fiz. **46**, 80 (1987) [Sov. J. Nucl. Phys. **46**, 51 (1987)].
[6] D. L. Morgan Jr. and V. W. Hughes, Phys. Rev. D **2**, 1389 (1970).
[7] J. P. Meyer, Astron. Astrophys., Suppl. Ser. **7**, 417 (1972).
[8] S. K. Abdullin, A. V. Blinov, I. A. Vanyushin *et al.*, Yad. Fiz. **56**, 204 (1993); A. V. Blinov, V. E. Grechko, S. M. Zombikovskiĭ*et al.*, Yad. Fiz. **58**, 1814 (1995).
[9] H. Braun, Yu. Glavachova, V. V. Glagolev *et al.*, Yad. Fiz. **59**, 2001 (1996).

Translated by M. E. Alferieff

Record energy of a giant shower

E. E. Antonov, L. G. Dedenko,* and Yu. P. Pyt'ev
M. V. Lomonosov Moscow State University, 119899 Moscow, Russia

A. V. Glushkov, M. I. Pravdin, and I. E. Sleptsov
Institute of Cosmophysical Studies and Aeronomy, Siberian Branch of the Russian Academy of Sciences, 677891 Yakutsk, Russia

T. M. Roganova and G. F. Fedorova
M. V. Lomonosov Scientific-Research Institute of Nuclear Physics, Moscow State University, 119899 Moscow, Russia

(Submitted 26 March 1999)
Pis'ma Zh. Éksp. Teor. Fiz. **69**, No. 9, 614–619 (10 May 1999)

According to a reliable ($\chi_1^2=0.93$ with 36 degrees of freedom) interpretation of the readings of all triggered detector stations in a giant shower, detected at the Yakutsk array on May 7, 1989 at 13 h 23 min Greenwich time, in terms of the quark–gluon strings model with the geomagnetic field taken into account, the energy of this shower was 3×10^{20} eV. © *1999 American Institute of Physics.*
[S0021-3640(99)00209-1]

PACS numbers: 96.40.Pq, 13.85.Tp

1. Introduction

After the possible existence of giant air showers (GASs) was first mentioned,[1–3] observations of three GASs with energies estimated to be much greater than $E_0\sim10^{20}$ eV were reported.[4–6] For this reason, the Greisen–Zatsepin–Kuz'min (GZK) prediction[7,8] of a possible cutoff of the energy spectrum of primary cosmic ray particles due to their interaction with the microwave relic radiation can be regarded supporting the hypothesis of a local distribution of sources of superhigh-energy particles (within ~30 Mpc). The detection of six new showers with energies exceeding 10^{20} eV has recently been reported.[9] These facts can all be interpreted as possible evidence of the existence of either new forms of matter (topological defects), or hypothetical ultraheavy particles, or unknown mechanisms of charged-particle acceleration in nearby sources, or previously unknown processes and objects. Thus one can talk about the discovery of a new phenomenon — GASs with energies above 10^{20} eV.

In view of the critical importance of this phenomenon, the validity, reliability, and accuracy of estimates of the energy and directions of arrival of a GAS become especially important. In the present work we have proposed and implemented a new method for obtaining such estimates on the basis of an interpretation of the readings of all detectors in terms of the quark–gluon strings (QGS) model,[10] taking external factors (geomagnetic field) and the normalization of certain computational parameters of the showers into account in accordance with the experimental data.

2. New method for obtaining estimates

The experimental data are interpreted in several steps. First, the zenith angle θ and azimuthal angle ϕ characterizing the direction of the GAS axis are estimated from the data from the time channel of the readings of the detectors. We have shown[11] that interpreting the data in terms of not the planar-front model but rather the computed spatiotemporal structure of the shower for various types of detected particles decreases the error in the angle estimates from several degrees to $\sim 1.5°$ using the minimum-χ^2 method and to $\sim 0.5°$ for the minimax method. Specifically, for the Yakutsk GAS, which consisted of muons, we obtained by the minimax method the estimates $\theta = 58.2° \pm 0.5°$ and $\phi = 164.2° \pm 0.4°$. The value of χ_1^2 decreases from ~ 2.2 to ~ 0.4 with 14 degrees of freedom, i.e., the reliability of the interpretation increases substantially.

The next step is to determine the coordinates X and Y of the point of intersection of the shower axis and the plane of the array and the parameter $\rho(600,\theta)$ (the charged-particle densities 600 m from the shower axis) on the basis of the adopted symmetric spatial distribution function (SDF) of particles in a plane perpendicular to the shower axis (in what follows, the shower plane). In our view this procedure introduces into the detector readings additional errors due to the transition from the array plane to the shower plane. Another important source of possible errors is the fact that the quality of such an interpretation is virtually ignored. The particle SDF adopted may not correspond to the actual particle distribution for some reason, but the result of the interpretation — the value of the parameter $\rho(600,\theta)$ — will be adopted. For example, for the standard interpretation of the data on the Yakutsk GAS $\chi_{21}^2 = 39.1$ (reliability less than 1%). It is obvious that the estimates of the parameter $\rho(600,\theta)$ and the coordinates of the shower axis obtained in this case are suboptimal.

We propose that the readings of all detectors in the array plane be interpreted on the basis of the computed SDF of the detected particles using a selected model taking account of external factors (the geomagnetic field). The results should be estimates of the energy E_0 and the coordinates X and Y of the shower axis in the array plane. Thus we arrive at the problem of minimizing

$$\chi_{n-3}^2 = \sum_{i=1}^{n} \left(\frac{\rho_t - \rho_{exp}}{\sigma} \right)^2, \tag{1}$$

where n is the number of triggered detectors and ρ_{exp} and ρ_t are, respectively, the detected and computed particle densities, on the set of possible values of X, Y, and E_0. It is obvious that even the ''best'' model and various approximations do not necessarily correspond to the data at the highest energies. For this reason, a procedure was adopted whereby the computed characteristics of the GAS are normalized to the experimental data obtained using the calorimetric determination method,[12] i.e., in accordance with the law of conservation of energy. The details of this normalization are described in Sec. 3.

Figure 1 shows for the Yakutsk GAS a ''grid'' of ratios z of the muon densities calculated with and without the geomagnetic field **B**. The $z = 1$ plane corresponds to $\mathbf{B} = 0$; the points with error bars correspond to the experimental data for GAS,[4] divided by the computed densities in the $\mathbf{B} = 0$ approximation. It is evident from Fig. 1 that the experimental points cluster around the ''grid.'' Thus the the geomagnetic field greatly degrades the azimuthal symmetry of the muon SDF, and for this reason the use of a

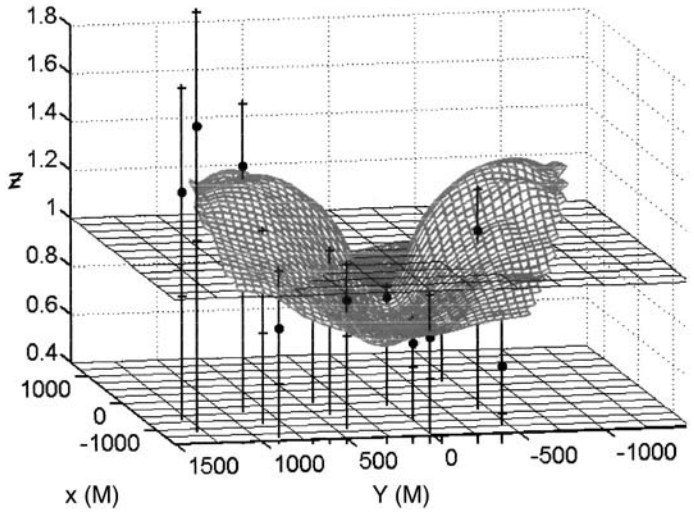

FIG. 1. ''Grid'' of ratios z (vertical axis) of the muon densities calculated with the geomagnetic field **B** taken into account and in the $\mathbf{B}=0$ approximation. Circles with errors — data of Ref. 4; $z=1$ plane — $\mathbf{B}=0$ case.

symmetric SDF in the standard interpretation procedure is a simplification. We proposed the method (1) precisely because an asymmetric muon SDF can be calculated for each specific case. Taking account of the geomagnetic field, $\chi_1^2=0.93$ with 36 degrees of freedom, i.e., the proposed interpretation of the GAS data is entirely reasonable, while the reliability of the standard procedure is $\sim 1\%$. Neglecting the geomagnetic field gives $\chi_1^2=2.03$ (the probability of agreement is less than 0.03%).[13] The values of the coordinates $X=1112$ m and $Y=-452$ m of the shower axis in the array plane, which are determined by the new method, differ from the initial estimates $X_0=1055$ m and $Y_0=-406$ m, which increases the average value of the parameter $\rho(600,\theta)$ by a factor of 1.45. Since this parameter $\rho(600,\theta,\phi)$ also depends on the azimuthal angle ϕ (the minimum value can differ from the maximum value by approximately a factor of ~ 1.5(!) — see Fig. 1), it should not be used to estimate the energy E_0. According to the proposed method, an estimate of E_0, just like estimates of X and Y, is obtained by minimizing expression (1). Taking into account the normalization of the computed muon densities (see Sec. 3), this minimum obtains for $E_0=3\times 10^{20}$ eV, which is two or three times higher than the old estimate.[4] It should be noted especially that the interpretation of the experimental results is finished at this stage, since all required estimates have been obtained.

In the standard procedure other steps, each of which can lead to additional errors, are required. For example, switching from the parameter $\rho(600,\theta)$ averaged over azimuthal angles to its value for vertical showers ($\theta=0$), assuming exponential absorption, can lead to a substantial discrepancy with the theory, which also does not give unequivocal predictions (see below). This is illustrated in Fig. 2, which shows the computed θ dependence of the charged-particle density $\rho(600,\theta)$:

$$\rho(600,\theta)=\rho_e(600,\theta)+1.25\cdot k_\mu\cdot\rho_\mu(600,\theta,\geqslant E_\mu), \tag{2}$$

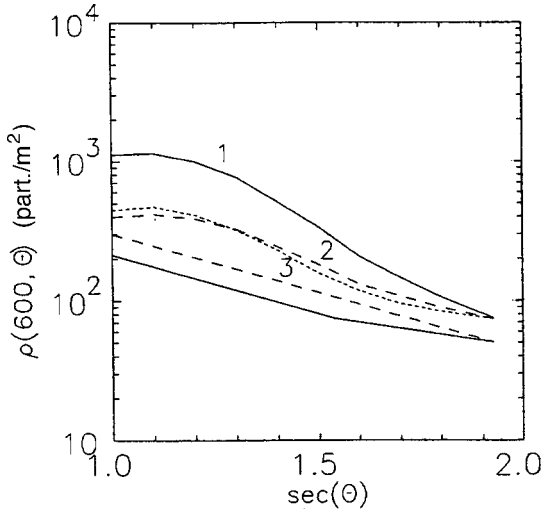

FIG. 2. Charged-particle density 600 m from the axis of a 3×10^{20} eV shower as a function of the zenith angle θ. Curves *1*, *2*, and *3* correspond to the assumptions of Refs. 14, 15, and 16 about the electron SDF and are drawn from $\rho(600,\theta)=77.6$. The two straight lines represent two variants of exponential absorption and are drawn from $\rho(600,\theta)=53.9$.

where ρ_e and ρ_μ are the electron and muon densities, $E_\mu=0.3$ GeV, the factor 1.25 takes into account the muon-decay electrons, and $k_\mu=1.42$ is a normalization factor (see Sec. 3). Curves *1*, *2*, and *3* were calculated according to three different hypotheses concerning the electron SDF (*1* — NKG approximation,[14] *2* — model with a modified NGK function,[15] *3* — approximation used in Ref. 16). These curves are drawn from the new value $\rho(600,\theta)=77.6$ and demonstrate the nonuniqueness of switching to $\rho(600,0)$. The two straight lines correspond to two values of the absorption range λ used at the Yakutsk array and are drawn from the initial estimate $\rho(600,\theta)=53.9$.

The calorimetric determination method[12] gives the following estimate of E_0 on the basis of the value of the parameter $\rho(600,0)$:

$$E_0=a\cdot\rho^{\alpha}(600,0), \tag{3}$$

where $a=4.8\times10^{17}$ eV and $\alpha=1$. However, since the statistical sample of the events is limited at superhigh energies, such a calibration is actually obtained in a narrow energy range where the error in the estimation of α is large. At the highest energies the shower maximum approaches the observation level and the ratios of the various shower characteristics change. For this reason extrapolating the calibration to superhigh energies is not entirely sound. For example, calculations in the QGS model with the normalization of the signal taken into account (see Sec. 3) give $a=4.55\times10^{17}$ eV and $\alpha=1.07$ and therefore an additional increase in the estimate of the energy E_0 by a factor of approximately 1.5. Our method (1) does not contain this step and the additional errors due to it.

3. Normalization of the computed shower parameters

The calorimetric determination method,[12] which is based on measurements of the Cherenkov light, is the main advantage of the Yakutsk array. For this reason, the idea of

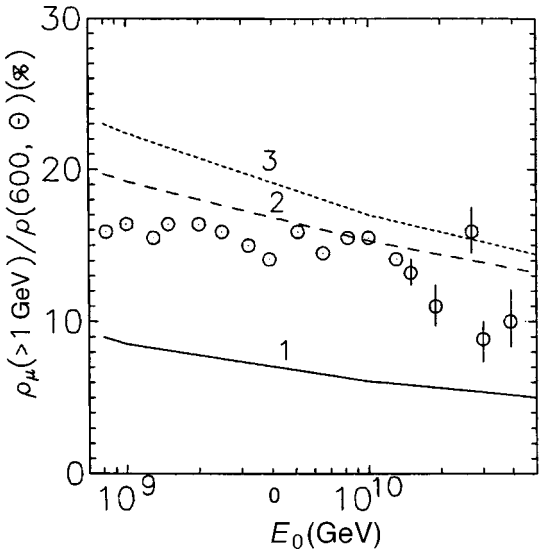

FIG. 3. Fraction of muons with energy $E_\mu \geqslant 1$ GeV 600 m from the shower axis as a function of E_0. Curves *1*, *2*, and *3* correspond to the assumptions of Refs. 14, 15, and 16 concerning the electron SDF. Circles — data from Ref. 19 for $\theta = 18°$.

normalizing the computed shower parameters with respect to the results of Ref. 12 is of interest. For the experimentally estimated energies E_0,[12] the computed Cherenkov photon fluxes Φ are 2%–5% higher than the measured values. This means that the dynamics of the development of hadron cascades in the atmosphere can be described completely satisfactorily on the basis of the adopted model[10] and approximations. The good agreement between the computed cascade curves[17] and the data of Ref. 6 also shows that the development of a shower in the longitudinal direction can also be described on the basis of the QGS model at energies $\sim 3\times 10^{20}$ eV. However, the computed energy fraction $E_{\mu\nu}/E_0$, which goes into muons and neutrinos, is on average 1.42 times smaller than the value estimated experimentally. For this reason, the factor $k_\mu = 1.42$ was introduced in Eq. (2) for the charged-particle density, i.e., normalization of the computed muon densities was performed. We also note that for $k_\mu = 1.42$ our computational results for the muon density agree with the calculations performed using the COSMOS code.[18] In the total energy balance this means that the computed fraction of the energy of the electron-photon component decreases by 2%–3%, i.e., precisely by the amount following from a comparison of the Cherenkov photon fluxes.

Figure 3 illustrates the fact that for the chosen normalization of the muon densities ($k_\mu = 1.42$) and the assumption of Ref. 15 concerning the electron SDF the computed fraction of muons with energies $E_\mu \geqslant 1$ GeV agrees with the experimental fraction,[19] i.e., all existing experimental data can be described well in this case.

In summary, the interpretation of the readings of all triggered detectors in the GAS detected at the Yakutsk array in terms of the QGS model with the geomagnetic field taken into account and with normalization of only one parameter of the shower (the muon density) shows to a high degree of reliability ($\chi_1^2 = 0.93$ with 36 degrees of freedom) that

the energy E_0 of this shower is $\sim 3\times 10^{20}$ eV. This result does not depend on the assumption made in Ref. 15 about the electron SDF, since the method proposed for analyzing the muon GAS does not involve switching to shower parameters for the vertical direction. It is interesting that both the energy estimate and the direction of arrival of this shower agree well with the analogous estimates of the GAS detected in the USA at the Fly's Eye array.[6] Without normalization (i.e., with $k_\mu = 1$) the energy E_0 increases to 4.3×10^{20} eV.

In closing, we wish to thank G. T. Zatsepin for a fruitful discussion of the results, suggestions, and support.

*e-mail: ddn@dec1.npi.msu.su

[1] J. Linsley, Phys. Rev. Lett. **10**, 146 (1963).
[2] G. Brooke, G. Cunningham, P. I. Eames *et al.*, in *Proceedings of the 19th ICRC*, La Jolla, Calif. (1985), Vol. 2, p. 150.
[3] M. M. Winn, J. Ulrichs, L. Horton *et al.*, in *Proceedings of the 19th ICRC*, La Jolla, Calif. (1985), Vol. 9, p. 499.
[4] N. N. Efimov, T. A. Egorov, A. V. Glushkov *et al.*, in *Proceedings of the International Workshop on Astrophysical Aspects of the Most Energetic Cosmic Rays*, Kofu (1990), p. 20.
[5] N. Hayashida, K. Honda, M. Honda *et al.*, Phys. Rev. Lett. **73**, 3491 (1994).
[6] D. J. Bird, S. C. Corbato, H. U. Dai *et al.*, Astrophys. J. **424**, 491 (1994).
[7] K. Greisen, Phys. Rev. Lett. **2**, 748 (1966).
[8] G. T. Zatsepin and V. A. Kuz'min, JETP Lett. **4**, 78 (1966).
[9] M. Takeda, N. Hayashida, K. Honda *et al.*, Phys. Rev. Lett. **81**, 1163 (1998).
[10] A. B. Kaĭdalov, K. A. Ter-Martirosyan, and Yu. M. Shabel'skiĭ, Yad. Fiz. **43**, 1282 (1986) [Sov. J. Nucl. Phys. **43**, 822 (1986)].
[11] E. E. Antonov, A. V. Glushkov, T. A. Grigoryan *et al.*, Izv. Ross. Akad. Nauk, Ser. Fiz. **63**, 542 (1999).
[12] A. V. Glushkov, M. N. D'yakonov, T. A. Egorov *et al.*, Izv. Akad. Nauk SSSR, Ser. Fiz. **55**, 713 (1991).
[13] E. E. Antonov, A. V. Glushkov, L. G. Dedenko *et al.*, JETP Lett. **68**, 185 (1998).
[14] K. Greisen, in *The Physics of Cosmic Rays* [Russian translation], Inostr. Lit., Moscow, 1958, Vol. 3, p. 3.
[15] L. G. Dedenko, N. M. Nesterova, S. I. Nikolsky *et al.*, in *Proceedings of the 14th ICRC*, Munich (1975), Vol. 8, p. 2731.
[16] A. A. Lagutin, A. V. Plyasheshnikov, and V. V. Melentjeva, in *Proceedings of the 25th ICRC*, Durban (1997), Vol. 6, p. 289.
[17] A. M. Anokhina, V. I. Galkin, L. G. Dedenko *et al.*, Yad. Fiz. **60**, 290 (1997).
[18] N. Hayashida, K. Honda, M. Honda *et al.*, in *Proceedings of the 25th ICRC*, Durban (1997), Vol. 6, p. 241.
[19] A. V. Glushkov, V. B. Kosarev, I. T. Makarov *et al.*, JETP Lett. **67**, 383 (1998).

Translated by M. E. Alferieff

Twisted spinors on black holes

Yu. P. Goncharov
Theoretical Group, Experimental Physics Department, State Technical University, 195251 St. Petersburg, Russia

(Submitted 2 April 1999)
Pis'ma Zh. Éksp. Teor. Fiz. **69**, No. 9, 619–625 (10 May 1999)

It is noted that the standard black hole topology admits twisted configurations of the spinor field owing to the existence of twisted spinor bundles, and they are analyzed using the Schwarzschild black hole as an example. This is physically linked with the natural presence of Dirac monopoles on black holes and entails marked modification of the Hawking radiation for spinor particles. © *1999 American Institute of Physics.* [S0021-3640(99)00309-6]

PACS numbers: 04.70.Dy, 04.20.Gz

1. A few years ago there appeared an interest in studying topologically inequivalent configurations (TICs) of various fields on 4D black holes, since TICs might give marked additional contributions to quantum effects in the 4D black hole physics, e.g., Hawking radiation,[2] and also might help to solve the problem of laying a statistical foundation for the black hole entropy.[2] So far, however, only TICs of the complex scalar field have been studied, more or less on the Schwarzschild (SW), Reissner–Nordström (RN), and Kerr black holes. The next physically important case is that of spinor fields. In the present paper we begin a study of twisted TICs of spinor fields in a form convenient for physical applications, restricting ourselves here for the sake of simplicity to the framework of the SW black hole geometry.

We write down the black hole metric under discussion (using the ordinary set of local coordinates t,r,ϑ,φ) in the form

$$ds^2=g_{\mu\nu}dx^\mu\otimes dx^\nu\equiv a\,dt^2-a^{-1}dr^2-r^2(d\vartheta^2+\sin^2\vartheta\,d\varphi^2) \tag{1}$$

with $a=1-r_g/r$, $r_g=2M$, where M is the mass of the black hole. In addition, we have $|g|=|\det(g_{\mu\nu})|=(r^2\sin\vartheta)^2$ and $r_g\leqslant r<\infty$, $0\leqslant\vartheta<\pi$, $0\leqslant\varphi<2\pi$.

Throughout the paper we employ the system of units with $\hbar=c=G=1$, unless explicitly stated otherwise. Finally, we shall denote by $L_2(F)$ the set of the modulo square integrable complex functions on any manifold F furnished with an integration measure.

2. The existence of TICs of a spinor field on black holes follows from the fact that over the standard black hole topology $\mathbb{R}^2\times\mathbb{S}^2$ there exists only one Spin-structure [conforming to the group Spin(1,3)= SL(2,$\mathbb{C}$)]. Referring for the exact definition of Spin-structure to Refs. 5 and 6, we only note here that the number of inequivalent Spin-structures for a manifold M is equal to the number of elements in $H^1(M,\mathbb{Z}_2)$, the first

cohomologygroup of M with coefficients in $\mathbb{Z}_2$. In our case $H^1(\mathbb{R}^2\times\mathbb{S}^2,\mathbb{Z}_2)=H^1(\mathbb{S}^2,\mathbb{Z}_2)$, which is equal to 0, and thus there exists only the trivial Spin-structure.

On the other hand, the nonisomorphic complex line bundles over M are classified by the elements in $H^2(M,\mathbb{Z})$, the second cohomology group of M with coefficients in $\mathbb{Z}$ (Refs. 5 and 6). In our case this group is equal to $H^2(\mathbb{S}^2,\mathbb{Z})=\mathbb{Z}$, and, consequently, the number of complex line bundles is countable. As a result, each complex line bundle can be characterized by an integer $n\in\mathbb{Z}$, which in what follows will be called its Chern number.

In this situation, if we denote by $S(M)$ the only standard spinor bundle over $M=\mathbb{R}^2\times\mathbb{S}^2$ and by ξ the complex line bundle with Chern number n, we can construct the tensor product $S(M)\otimes\xi$. As is known,[7] over any noncompact spacetime the bundle $S(M)$ is trivial and, accordingly, the Chern number of the 4D vector bundle $S(M)\otimes\xi$ is equal to n as well. Under the circumstances we obtain the twisted Dirac operator $\mathcal{D}:S(M)\otimes\xi\to S(M)\otimes\xi$, and so the wave equation for the corresponding spinors ψ (with a mass μ_0) as sections of the bundle $S(M)\otimes\xi$ may look as follows:

$$\mathcal{D}\psi=\mu_0\psi, \tag{2}$$

and we can call the (standard) spinors corresponding to $n=0$ (trivial complex line bundle ξ) *untwisted*, while the rest of the spinors with $n\neq 0$ should be referred to as *twisted*.

From general considerations[5,6,8] the explicit form of the operator $\mathcal{D}$ in local coordinates x^μ on a $2k$-dimensional (pseudo)Riemannian manifold can be written as follows:

$$\mathcal{D}=i\nabla_\mu\equiv i\gamma^a E_a^\mu\left(\partial_\mu-\frac{1}{2}\omega_{\mu ab}\gamma^a\gamma^b-ieA_\mu\right),\quad a<b, \tag{3}$$

where $A=A_\mu dx^\mu$ is a connection in the bundle ξ and the forms $\omega_{ab}=\omega_{\mu ab}dx^\mu$ obey the Cartan structure equations $de^a=\omega^a{}_b\wedge e^b$ with exterior derivative d, while the orthonormal basis $e^a=e^a_\mu dx^\mu$ in the cotangent bundle and the dual basis $E_a=E_a^\mu\partial_\mu$ in the tangent bundle are connected by the relations $e^a(E_b)=\delta^a_b$. Finally, the matrices γ^arepresent the Clifford algebra of the corresponding quadratic form in $\mathbb{C}^{2^k}$. Below we shall deal only with the 2D Euclidean case (quadratic form $Q_2=x_0^2+x_1^2$) or with the 4D Lorentzian case (quadratic form $Q_{1,3}=x_0^2-x_1^2-x_2^2-x_3^2$). For the latter case we take the following choice for γ^a:

$$\gamma^0=\begin{pmatrix}1&0\\0&-1\end{pmatrix},\quad \gamma^b=\begin{pmatrix}0&\sigma_b\\-\sigma_b&0\end{pmatrix},\quad b=1,2,3, \tag{4}$$

where the σ_b denote the ordinary Pauli matrices. It should be noted that, in the Lorentzian case, Greek indices $\mu,\nu,\ldots$ are raised and lowered with $g_{\mu\nu}$ of (1) or its inverse $g^{\mu\nu}$ while Latin indices $a,b,\ldots$ are raised and lowered by $\eta_{ab}=\eta^{ab}=$ diag(1,–1,–1,–1), so that $e^a_\mu e^b_\nu g^{\mu\nu}=\eta^{ab}$, $E_a^\mu E_b^\nu g_{\mu\nu}=\eta_{ab}$ and so on.

Using the fact that all of the aforementioned bundles $S(M)\otimes\xi$ can be trivialized over the chart of local coordinates (t,r,ϑ,φ) covering almost the whole manifold $\mathbb{R}^2\times\mathbb{S}^2$, we can concretize the wave equation (2)on the given chart for a TIC ψ with Chern number $n\in\mathbb{Z}$ in the case of metric (1). Namely, we can put $e^0=\sqrt{a}dt$,

$e^1=dr/\sqrt{a}$, $e^2=rd\vartheta$, $e^3=r\sin\vartheta d\varphi$ and, accordingly, $E_0=\partial_t/\sqrt{a}$, $E_1=\sqrt{a}\partial_r$, $E_2=\partial_\vartheta/r$, $E_3=\partial_\varphi/r\sin\vartheta$. This entails

$$\omega_{01}=-\frac{1}{2}\frac{da}{dr}dt, \quad \omega_{12}=-\sqrt{a}d\vartheta, \quad \omega_{13}=-\sqrt{a}\sin\vartheta d\varphi, \quad \omega_{23}=-\cos\vartheta d\varphi. \quad (5)$$

As to the connection A_μ in the bundle ξ, a suitable one was found in Ref. 1 and is $A=A_\mu dx^\mu=-(n/e)\cos\vartheta d\varphi$. Then the curvature of the bundle ξ is $F=dA=(n/e)\sin\vartheta d\vartheta\wedge d\varphi$. We can further introduce the Hodge star operator on 2-forms F of any k-dimensional (pseudo)Riemannian manifold B provided with a (pseudo)Riemannian metric $g_{\mu\nu}$ by the relation (see, e. g., Ref. 8)

$$F\wedge *F=(g^{\mu\alpha}g^{\nu\beta}-g^{\mu\beta}g^{\nu\alpha})F_{\mu\nu}F_{\alpha\beta}\sqrt{|g|}\,dx^1\wedge dx^2\cdots\wedge dx^k \quad (6)$$

in local coordinates x^μ. In the case of the metric (1) this yields $*F=(n/er^2)dt\wedge dr$, and integrating over the surface $t=\text{const}$, $r=\text{const}$ with topology $\mathbb{S}^2$ gives rise to the Dirac charge quantization condition

$$\int_{S^2}F=4\pi\frac{n}{e}=4\pi q \quad (7)$$

with magnetic charge q, so we can identify the coupling constant e with the electric charge. Further, the Maxwell equations $dF=0$, $d\cdot F=0$ are clearly fulfilled with the exterior differential $d=\partial_t dt+\partial_r dr+\partial_\vartheta d\vartheta+\partial_\varphi d\varphi$ in coordinates t,r,ϑ,φ. We come to the same conclusion as in the case of TICs of a complex scalar field:[1–4] Dirac magnetic $U(1)$-monopoles naturally live on black holes as connections in complex line bundles, and, hence, physically the appearance of TICs for the spinor field should be attributed to the natural presence of Dirac monopoles on the black hole, and the interaction with them splits the spinor field into TICs. Also it should be emphasized that the total (internal) magnetic charge Q_m of the black hole, the result of summing over all the monopoles, remains equal to zero because

$$Q_m=\frac{1}{e}\sum_{n\in\mathbb{Z}}n=0. \quad (8)$$

Returning to Eq. (2), we see that when all the above is taken into account, it has the form

$$\left[i\gamma^0\frac{1}{\sqrt{a}}\left(\partial_t-\frac{1}{2}\omega_{t01}\gamma^0\gamma^1\right)+i\gamma^1\sqrt{a}\partial_r+i\gamma^2\frac{1}{r}\left(\partial_\vartheta-\frac{1}{2}\omega_{\vartheta 12}\gamma^1\gamma^2\right)\right.$$
$$\left.+i\gamma^3\frac{1}{r\sin\vartheta}\left(\partial_\varphi-\frac{1}{2}\omega_{\varphi 13}\gamma^1\gamma^3-\frac{1}{2}\omega_{\varphi 23}\gamma^2\gamma^3+in\cos\vartheta\right)\right]\psi=\mu_0\psi. \quad (9)$$

After a simple matrix algebra computation using (4) and (5), we find that Eq. (9) can be rewritten as

$$\begin{pmatrix}A & B\\ -B & -A\end{pmatrix}\begin{pmatrix}\psi_1\\ \psi_2\end{pmatrix}=\mu_0\begin{pmatrix}\psi_1\\ \psi_2\end{pmatrix}, \quad (10)$$

with the operators

$$A=\frac{i}{\sqrt{a}}\partial_t, \quad B=i\sigma_1 B_1+\frac{1}{r}B_2, \tag{11}$$

where, in turn,

$$B_1=\frac{1}{2}\frac{d\sqrt{a}}{dr}+\sqrt{a}\partial_r+\frac{\sqrt{a}}{r}, \quad B_2=i\sigma_2\partial_\vartheta+i\sigma_3\frac{1}{\sin\vartheta}\left(\partial_\varphi-\frac{1}{2}\sigma_2\sigma_3\cos\vartheta+in\cos\vartheta\right). \tag{12}$$

Now we can use the ansatz $\psi_1=e^{i\omega t}r^{-1}F_1(r)\Phi(\vartheta,\varphi)$, $\psi_2=e^{i\omega t}r^{-1}F_2(r)\sigma_1\Phi(\vartheta,\varphi)$ with a 2D spinor $\Phi=\binom{\Phi_1}{\Phi_2}$ to get, with the help of (10)–(12),

$$\left(B_1+\frac{1}{r}D_n\right)\psi_1=i(\mu_0-c)\sigma_1\psi_2,$$

$$\left(B_1+\frac{1}{r}D_n\right)\psi_2=-i(\mu_0+c)\sigma_1\psi_1, \tag{13}$$

with $c=(1/\sqrt{a})\omega$ and $D_n=-i\sigma_1 B_2$. It is natural to take Φ as an eigenspinor of the operator D_n, and, noting that $\sigma_1 D_n=-D_n\sigma_1$, we can obtain from (13) the system

$$\sqrt{a}\partial_r F_1+\left(\frac{1}{2}\frac{d\sqrt{a}}{dr}+\frac{\lambda}{r}\right)F_1=i(\mu_0-c)F_2,$$

$$\sqrt{a}\partial_r F_2+\left(\frac{1}{2}\frac{d\sqrt{a}}{dr}-\frac{\lambda}{r}\right)F_2=-i(\mu_0+c)F_1, \tag{14}$$

with an eigenvalue λ of the operator D_n. We should therefore explore the equation $D_n\Phi=\lambda\Phi$.

3. It is not hard to see that the operator D_n has the form (3) with $\gamma^0=-i\sigma_1\sigma_2$, $\gamma^1=-i\sigma_1\sigma_3$, $e^0=d\vartheta$, $e^1=\sin\vartheta d\varphi$, $\omega_{01}=\cos\vartheta d\varphi$, $A_\mu dx^\mu=-(n/e)\cos\vartheta d\varphi$, i.e., it corresponds to the above-mentioned quadratic form Q_2, and this is just a twisted (Euclidean) Dirac operator on the unit sphere, and the conforming complex line bundle is the restriction of the bundle ξ on the unit sphere. Again a simple matrix algebra computation results in

$$D_n=\begin{pmatrix} D_{1n} & D_{2n} \\ -D_{2n} & -D_{1n}\end{pmatrix}, \quad D_{1n}=i\left(\partial_\vartheta+\frac{1}{2}\cot\vartheta\right), \quad D_{2n}=-\frac{1}{\sin\vartheta}(\partial_\varphi+in\cot\vartheta).$$

Then it is easy to see that the equation $D_n\Phi=\lambda\Phi$ can be transformed into

$$\begin{pmatrix} 0 & D_n^- \\ D_n^+ & 0\end{pmatrix}\Phi_0=\lambda\Phi_0, \quad \Phi_0=\begin{pmatrix}\Phi_+\\ \Phi_-\end{pmatrix}, \tag{15}$$

where

$$D_n^\pm=D_{1n}\pm D_{2n}=i\left[\partial_\vartheta+\left(\frac{1}{2}\mp n\right)\cot\vartheta\right]\mp\frac{1}{\sin\vartheta}\partial_\varphi, \quad \Phi_\pm=\Phi_1\pm\Phi_2.$$

From here it follows that $D_n^- D_n^+\Phi_+=\lambda^2\Phi_+$, $D_n^+ D_n^-\Phi_-=\lambda^2\Phi_-$ or, with the use of the ansatz $\Phi_\pm=P_\pm(\vartheta)e^{-im'\varphi}$, in explicit form

$$\left[\partial_\vartheta^2+\cot\vartheta\partial_\vartheta-\frac{m'^2+(n\mp 1/2)^2-2m'(n\mp 1/2)\cos\vartheta}{\sin^2\vartheta}\right]P_\pm(\vartheta)$$
$$=\left(\frac{1}{4}-n^2-\lambda^2\right)P_\pm(\vartheta). \tag{16}$$

It is known[1,9] that the differential operators of the left-handside in (16) have in the interval $0\leqslant\vartheta\leqslant\pi$ eigenfunctions whichare finite at $\vartheta=0,\pi$ only for eigenvalues $-k(k+1)$, where k is a positive integer or half-integer, while at the same time $m',n'=n\pm 1/2$, and the multiplicity of such an eigenvalue is equal to $2k+1$. In our case we have that $n'=n\pm 1/2$ is half-integer because the Chern number $n\in\mathbb{Z}$. As a result, we should put $m'=m-1/2$ with an integer m and then $|m'|\leqslant k=l+1/2$ with a positive integer l and, accordingly, $1/4-n^2-\lambda^2=-k(k+1)$, which entails (denoting $\lambda=\sqrt{(l+1)^2-n^2}$) that the spectrum of D_n consists of the numbers $\pm\lambda$ with a multiplicity $2k+1=2(l+1)$ of each one. Besides, it is clear that under the circumstances one has $-l\leqslant m\leqslant l+1$, $l\geqslant|n|$. This just reflects the fact that from general considerations[5,6,8] the spectrum of a twisted Euclidean Dirac operator on an even-dimensional manifold is symmetric with respect the origin. The corresponding eigenfunctions $P_\pm(\vartheta)=P^k_{m'n'}(\cos\vartheta)$ of the above operators can be chosen in miscellaneous forms (see, e.g., Ref. 9) with the orthogonality relation at fixed n'

$$\int_0^\pi P^{*k}_{m'n'}(\cos\vartheta)P^{k'}_{m''n'}(\cos\vartheta)\sin\vartheta d\vartheta=\frac{2}{2k+1}\delta_{kk'}\delta_{m'm''}, \tag{17}$$

where (*) signifies complex conjugation. As a consequence, we come to the conclusion that the spinor Φ_0 of (15) can be chosen in the form

$$\Phi_0=\begin{pmatrix}C_1P^k_{m'n-1/2}\\ C_2P^k_{m'n+1/2}\end{pmatrix}e^{-im'\varphi}$$

with some constants $C_{1,2}$. Now we can employ the relations[9]

$$-\partial_\vartheta P^k_{m'n'}\pm\left(n'\cot\vartheta-\frac{m'}{\sin\vartheta}\right)P^k_{m'n'}=-i\sqrt{k(k+1)-n'(n'\pm 1)}P^k_{m'n'\pm 1} \tag{18}$$

which holds for the functions $P^k_{m'n'}$, to establish that $C_1=C_2=C$ corresponds to the eigenvalue λ, while $C_1=-C_2=C$ corresponds to $-\lambda$. Thus, the eigenspinors $\Phi=\binom{\Phi_1}{\Phi_2}$ of the operator D_n can be written as follows:

$$\Phi_{\pm\lambda}=\frac{C}{2}\begin{pmatrix}P^k_{m'n-1/2}\pm P^k_{m'n+1/2}\\ P^k_{m'n-1/2}\mp P^k_{m'n+1/2}\end{pmatrix}e^{-im'\varphi}, \tag{19}$$

where the coefficient C may be defined from the normalization condition

$$\int_0^\pi\int_0^{2\pi}(|\Phi_1|^2+|\Phi_2|^2)\sin\vartheta d\vartheta d\varphi=1, \tag{20}$$

which, with the use of relation (17), yields $C=\sqrt{(l+1)/\pi}$. These spinors form an orthonormal basis in $L_2^2(\mathbb{S}^2)$. Finally, it should be noted that the given spinors can be

expressed in terms of the monopole spherical harmonics $Y^l_{mn}(\vartheta,\varphi)=P^l_{mn}(\cos\vartheta)e^{-im\varphi}$, which naturally arise when one is considering twisted TICs of a complex scalar field,[9] but we shall not need it here.

4. It follows from what we have said that when quantizing twisted TICs of spinors we can take the set of spinors

$$\psi_{\pm\lambda}=\frac{1}{\sqrt{2\pi\omega}}e^{i\omega t}r^{-1}\begin{pmatrix} F_1(r,\pm\lambda)\Phi_{\pm\lambda} \\ F_2(r,\pm\lambda)\sigma_1\Phi_{\pm\lambda}\end{pmatrix} \tag{21}$$

as a basis in $L^4_2(\mathbb{R}^2\times\mathbb{S}^2)$ and implement the quantization procedure, as usual, by expanding in the modes (21):

$$\psi=\sum_{\pm\lambda}\sum_{l=|n|}^{\infty}\sum_{m=-l}^{l+1}\int_0^\infty d\omega(a^-_{\omega nlm}\psi_\lambda+b^+_{\omega nlm}\psi_{-\lambda}),$$

$$\overline{\psi}=\sum_{\pm\lambda}\sum_{l=|n|}^{\infty}\sum_{m=-l}^{l+1}\int_0^\infty d\omega(a^+_{\omega nlm}\overline{\psi}_\lambda+b^-_{\omega nlm}\overline{\psi}_{-\lambda}), \tag{22}$$

where $\overline{\psi}=\gamma^0\psi^\dagger$ is the adjoint spinor and ($\dagger$) stands for Hermitian conjugation. As a result, the operators $a^{\pm}_{\omega nlm}$, $b^{\pm}_{\omega nlm}$ of (22) should be interpreted as the creation and annihilation operators for a spinor particle in the gravitational field of the black hole and in the field of a monopole with Chern number n. As to the functions $F_{1,2}(r,\pm\lambda)$ of (21), in accordance with Eqs. (14) we can get the second-order equations for them in the form

$$a\partial_r a\partial_r F_{1,2}+a\left[\sqrt{a}\partial_r\left(\frac{1}{2}\frac{d\sqrt{a}}{dr}\pm\frac{\lambda}{r}\right)+\frac{1}{4}\left(\frac{d\sqrt{a}}{dr}\right)^2-\frac{\lambda^2}{r^2}\right]F_{1,2}=(a\mu_0^2-\omega^2)F_{1,2}. \tag{23}$$

Making the substitution $r^*=r+r_g\ln(r/r_g-1)$ and going over to the dimensionless quantities $x=r^*/M$, $y=r/M$, $k=\omega M$, we can rewrite Eqs. (23) in the Schrödinger-like form

$$\frac{d^2}{dx^2}E_{1,2}+[k^2-(\mu_0 M)^2]E_{1,2}=V_{1,2}(x,\lambda)E_{1,2}, \tag{24}$$

where $E_{1,2}=E_{1,2}(x,k,\lambda)=F_\pm(Mx)$, $F_\pm(r^*)=F_{1,2}[r(r^*)]$, and the potentials $V_{1,2}$ are given by

$$V_{1,2}(x,\lambda)=\frac{1}{4y^4(x)}+\left[\frac{1}{y^4(x)}\mp\frac{\lambda}{y^2(x)}\sqrt{1-\frac{2}{y(x)}}+\frac{\lambda^2}{y^2(x)}\right]\times\left[1-\frac{2}{y(x)}\right]-\frac{2}{y(x)}(\mu_0 M)^2, \tag{25}$$

where $y(x)$ is the inverse function for $x(y)=y+2\ln(0.5y-1)$, so $y(x)$ is a one-to-one correspondence between $(-\infty,\infty)$ and $(2,\infty)$.

Let us for the sake of simplicity restrict ourselves to massless spinors ($\mu_0=0$). Then, as can be seen, $V_{1,2}\to 0$ as $x\to+\infty$ and $V_{1,2}\to 1/64$ as $x\to-\infty$. This allows us to pose the scattering problem on the whole x axis for Eq. (24) at $k>0$:

$$E^{+}_{1,2}\sim\begin{cases} e^{ikx}+\ s^{(1,2)}_{12}e^{-ikx}+1/64k^2, & x\to-\infty,\\ s^{(1,2)}_{11}e^{ikx}, & x\to+\infty,\end{cases}$$

$$E^{-}_{1,2}\sim\begin{cases} s^{(1,2)}_{22}e^{-ikx}+1/64k^2, & x\to-\infty,\\ e^{-ikx}+s^{(1,2)}_{21}e^{ikx}, & x\to+\infty\end{cases} \tag{26}$$

with S-matrices $\{s^{(1,2)}_{ij}=s^{(1,2)}_{ij}(k,\lambda)\}$. Then by virtue of (14) one can obtain the equality

$$s^{(1)}_{11}(k,\lambda)=-s^{(2)}_{11}(k,\lambda). \tag{27}$$

Having obtained these relations, one can speak about the Hawking radiation process for any TIC of the spinor field on a black hole. Actually, one can notice that Eq. (2) corresponds to the Lagrangian

$$\mathcal{L}=\frac{i}{2}|g|^{1/2}[\bar{\psi}\gamma^{\mu}\nabla_{\mu}\psi-(\nabla_{\mu}\bar{\psi})\gamma^{\mu}\psi-\mu_0\bar{\psi}\psi], \tag{28}$$

and one can use the energy–momentum tensor for a TIC with Chern number n conforming to the Lagrangian (28),

$$T_{\mu\nu}=\frac{i}{4}[\bar{\psi}\gamma_{\mu}\nabla_{\nu}\psi+\bar{\psi}\gamma_{\nu}\nabla_{\mu}\psi-(\nabla_{\mu}\bar{\psi})\gamma_{\nu}\psi-(\nabla_{\nu}\bar{\psi})\gamma_{\mu}\psi], \tag{29}$$

to get, according to the standard prescription (see, e.g., Ref. 10) with the use of (20) and (27), the luminosity $L(n)$ with respect to the Hawking radiation for the TIC with Chern number n (in ordinary units)

$$L(n)=\lim_{r\to\infty}\int_{S^2}\langle 0|T_{\rm tr}|0\rangle d\sigma=A\sum_{\pm\lambda}\sum_{l=|n|}^{\infty}2(l+1)\int_0^{\infty}\frac{|s^{(1)}_{11}(k,\lambda)|^2}{e^{8\pi k}+1}dk, \tag{30}$$

with the vacuum expectation value $\langle 0|T_{\rm tr}|0\rangle$ and the surface element $d\sigma=r^2\sin\vartheta d\vartheta\wedge d\varphi$, while $A=(c^5/GM)(c\hbar/G)^{1/2}\approx 0.125728\times 10^{55}\,\mathrm{erg\cdot s^{-1}}M^{-1}$ (M in g).

We can interpret $L(n)$ as an additional contribution to the Hawking radiation due to the additional spinor particles leaving the black hole because of the interaction with monopoles. Under this situation, to obtain the total luminosity L of the black hole with respect to the Hawking radiation for the spinor field, one should sum up over all n, i.e.,

$$L=\sum_{n\in\mathbb{Z}}L(n)=L(0)+2\sum_{n=1}^{\infty}L(n), \tag{31}$$

since $L(-n)=L(n)$.

As a result, we can expect a marked increase of Hawking radiation from black holes for spinor particles. But in order to get an exact value of this increase one must apply numerical methods, inasmuch as the scattering problem for the general equation (24) does not admit any exact solution and is quite complicated to treat — the potentials $V_{1,2}(x,\lambda)$ of (25) are given in implicit form. We might mention that, for instance, the corresponding increase for the complex scalar field can amount to 17% of the total (summed up over all the TICs) luminosity.[2]

It is clear that the most general case is the Kerr–Newman black hole, but for it the equations will be more complicated, and we shall consider them elsewhere.

The work was supported in part by the Russian Fund for Fundamental Research (Grant 98-02-18380-a) and by GRACENAS (Grant 6-18-1997).

[1] Yu. P. Goncharov and J. V. Yarevskaya, Mod. Phys. Lett. F **9**, 3175 (1994); F **10**, 1813 (1995); Yu. P. Goncharov, Nucl. Phys. B **460**, 167 (1996).
[2] Yu. P. Goncharov and N. E. Firsova, Int. J. Mod. Phys. D **5**, 419 (1996); Nucl. Phys. B **486**, 371 (1997).
[3] Yu. P. Goncharov, Int. J. Mod. Phys. F **12**, 3347 (1997); JETP Lett. **67**, 1802 (1998); Mod. Phys. Lett. F **13**, 1495 (1998).
[4] Yu. P. Goncharov, Phys. Lett. B **398**, 32 (1997); Int. J. Mod. Phys. D **8**, 123 (1999).
[5] *Géométrie Riemannian en Dimension 4*, Seminaire Arthur Besse, Cedic/Fernand Nathan, Paris, 1981.
[6] H. B. Lawson Jr. and M.-L. Michelsohn, *Spin Geometry*, Princeton Univ. Press, Princeton, 1989.
[7] R. Geroch, J. Math. Phys. **9**, 1739 (1968); C. J. Isham, Proc. R. Soc. London, F **364**, 591 (1978).
[8] A. L. Besse, *Einstein Manifolds*, Springer-Verlag, Berlin, 1987.
[9] N. Ya. Vilenkin, *Special Functions and Theory of Group Representations* [in Russian], Nauka, Moscow, 1991.
[10] D. V. Gal'tsov, *Particles and Fields in the Vicinity of Black Holes* [in Russian], Moscow University Press, 1986.

Published in English in the original Russian journal. Edited by Steve Torstveit.

On triple correlations in isotropic electronic magnetohydrodynamic turbulence

O. Chkhetiani*
Institute of Space Studies, Russian Academy of Sciences, 117810 Moscow, Russia

(Submitted 25 February 1999; resubmitted 10 March 1999)
Pis'ma Zh. Éksp. Teor. Fiz. **69**, No. 9, 626–630 (10 May 1999)

The evolution of the correlation characteristics in three-dimensional isotropic electronic magnetohydrodynamic turbulence is investigated. Universal exact relations between the longitudinal and longitudinal–transverse two-point triple correlations of the components of the fluctuational magnetic fields and the rates of dissipation of the magnetic helicity and energy are obtained in the inertial range. © *1999 American Institute of Physics.* [S0021-3640(99)00409-0]

PACS numbers: 52.35.Bj, 52.35.Ra

All statistical theories of turbulence take into account the well-known exact Kolmogorov result — the 4/5 law,[1] which relates the third-order spatial longitudinal correlations of the velocity with the rate of energy dissipation. In magnetohydrodynamics such a relation was obtained by Chandrasekhar.[2] Recently a similar relation (2/15 law) was established for hydrodynamic turbulence with helicity.[3,4] The confirmations of the 4/5 law for diverse turbulent hydrodynamic flows are well known.[5] Confirmations have been obtained for the 2/15 law[3,4] for helicity.[6] It is important to note that such accurate relations are obtained by solving dynamical equations and are a consequence of the conservation laws. No dimensional considerations are employed in their derivation. The fundamental significance of the 4/5 law in hydrodynamics has been examined in detail in Ref. 7.

Electronic magnetohydrodynamics (EMHD) pertains to a branch of plasma oscillations on which the Hall term predominates,[8,9] and it is a limiting case of multicomponent MHD, where the motion of the ions can be neglected and the motion of the electrons preserves quasineutrality. In contrast to the standard MHD case, the description (with uniform density) can be reduced to a single nonlinear equation for the magnetic field. The region of applicability of EMHD are laboratory and industrial plasma setups, the ionosphere, the solar photosphere, and solids.[9,10] In the 1970s the term MHD at helicon frequencies was also used.[10] Weak turbulence of helicons (whistler) was studied in Refs. 11–13. The dynamic properties of strong three-dimensional turbulence in EMHD have been studied in Ref. 14. Arguments supporting the idea that only weak turbulence is realized in the EMHD mechanism are presented in Ref. 8.

EMDH is described by the equation[8,14]

$$\partial_t \mathbf{h} + \mathrm{curl}\left[\frac{\mathbf{j}}{ne}\times\mathbf{h}\right] + c\,\mathrm{curl}\,\frac{\mathbf{j}}{\sigma} = 0, \tag{1}$$

$$\mathbf{j} = \frac{c}{4\pi}\,\mathrm{curl}\,\mathbf{h}, \quad \mathrm{div}\,\mathbf{h} = 0. \tag{2}$$

For $n = \mathrm{const}$ and $\sigma = \mathrm{const}$ obtain

$$\partial_t \mathbf{h} = -\frac{c}{4\pi ne}\,\mathrm{curl}[\mathrm{curl}\,\mathbf{h}\times\mathbf{h}] + \frac{c^2}{4\pi\sigma}\Delta\mathbf{h}, \quad \mathrm{div}\,\mathbf{h} = 0. \tag{3}$$

In the frequency domain this corresponds to the range

$$w_i < w < w_e\,.$$

For what follows, we introduce the notation $f = c/4\pi ne$ and $\nu_m = c^2/4\pi\sigma$. The structure of Eq. (3) is close to the Navier–Stokes equation for an incompressible liquid. We can verify by direct substitution that it conserves the energy

$$\int_V \frac{\mathbf{h}^2}{2}\,dV$$

and the helicity

$$\int_V \mathbf{a}\cdot\mathbf{h}\,dV$$

of the magnetic field.

Let us consider the free evolution of uniform and isotropic fluctuations of the magnetic field in EMHD. Writing out the equation for the vector potential $\mathbf{a} = \mathrm{curl}^{-1}\mathbf{h}$ and averaging, we obtain equations of the Kármán–Howarth type for the two-point correlation functions involving the energy and helicity of the magnetic field:

$$\begin{aligned}\partial_t h_{ii} &= f\varepsilon_{ijk}\frac{\partial^2}{\partial r_i \partial r_m}(h_{j,km} - h_{jm,k}) + 2\nu_m\Delta_r h_{ii} \\ &= f\varepsilon_{ijk}\frac{\partial^2}{\partial r_i \partial r_m}(h_{km,j} - h_{jm,k}) + 2\nu_m\Delta_r h_{ii}\,,\end{aligned} \tag{4}$$

$$\partial_t g_{ii} = 2f\frac{\partial}{\partial r_m}h_{im,i} + 2\nu_m\Delta_r g_{ii}\,, \tag{5}$$

where

$$h_{ii} = \langle h_i(\mathbf{x})h_i(\mathbf{x}+\mathbf{r})\rangle, \quad g_{ii} = \langle a_i(\mathbf{x})h_i(\mathbf{x}+\mathbf{r})\rangle, \tag{6}$$

$$h_{jm,k} = \langle h_j(\mathbf{x})h_m(\mathbf{x})h_k(\mathbf{x}+\mathbf{r})\rangle. \tag{7}$$

The right-hand sides of Eqs. (4) and (5) contain the spatial derivatives with respect to r of the rank-3 two-point correlation tensor. The general form of such a tensor, with allowance for the gyrotropy and incompressibility of the magnetic field, is[2–4]

$$h_{ij,k}(\mathbf{r}) = V(\varepsilon_{jkl} r_i r_l + \varepsilon_{ikl} r_j r_l) + \frac{2}{r}\partial_r T r_i r_j r_k - (r\partial_r T + 3T)(r_i \delta_{jk} + r_j \delta_{ik}) + 2T\delta_{ij} r_k . \tag{8}$$

Fluctuations of the magnetic field without helicity were considered in Ref. 2. In that case the tensor $h_{ij,k}$ consists of only the first two terms, which are proportional to the scalar V, which is related to the energy transfer. Taking the helicity into account introduces additional terms which are proportional to the product of pseudoscalar quantities and odd combinations of the components of the radius vector. Formally, the solenoidal tensor (8) is identical to the analogous tensor for triple correlations of the velocity field in hydrodynamic turbulence.[3] However, in contrast to the latter it does not change under reflection of the coordinates, i.e., $h_{ij,k}(-\mathbf{r}) = h_{ij,k}(\mathbf{r})$. The properties of homogeneous turbulence also imply that $h_{k,ij}(r) = h_{ij,k}(-r)$.[5] Both properties are taken into account in Eq. (4).

In what follows we shall need to examine the auxiliary tensor $\langle \delta h_i(\mathbf{x}|\mathbf{r})\, \delta h_j(\mathbf{x}|\mathbf{r})\rangle$, where $\delta\mathbf{h}(\mathbf{x}|\mathbf{r}) = \mathbf{h}(\mathbf{x}+\mathbf{r}) - \mathbf{h}(\mathbf{x})$. In homogeneous turbulence it has the form

$$\langle \delta h_i(\mathbf{x}|\mathbf{r})\, \delta h_j(\mathbf{x}|\mathbf{r})\rangle = B_{tt}(r)(\delta_{ij} - n_i n_j) + B_{rr} n_i n_j ,$$

where $n = \mathbf{r}/|\mathbf{r}|$. The incompressibility condition implies that $B_{tt} = (1/2r)\,\partial_r(r^2 B_{rr})$ (Ref. 15). Then

$$\langle h_i(\mathbf{x}) h_i(\mathbf{x}+\mathbf{r})\rangle = \langle \mathbf{h}^2(\mathbf{x})\rangle - \frac{1}{2r^2}\partial_r(r^3 B_{rr}). \tag{9}$$

We represent g_{ii} in the form

$$g_{ii} = \langle a_i(\mathbf{x}) h_i(\mathbf{x}+\mathbf{r})\rangle = \langle a_i(\mathbf{x}+\mathbf{r}) h_i(\mathbf{x}+\mathbf{r})\rangle - \frac{2}{r^2}\partial_r(r^3 C(r)). \tag{10}$$

Substituting expressions (8)–(10) into Eqs. (4) and (5) we obtain

$$-2\overline{\varepsilon}_m - \frac{1}{2}\partial_t \frac{1}{r^2}\partial_r(r^3 B_{rr}) = -\frac{4f}{r^2}\partial_r\left(\frac{1}{r}\partial_r(r^5 V)\right) - \frac{\nu_m}{r^2}\partial_r\left(\frac{1}{r^2}\partial_r(r^3 B_{rr})\right), \tag{11}$$

$$-2\overline{\eta}_m - \partial_t \frac{2}{r^2}\partial_r(r^3 C) = -\frac{4f}{r^2}\partial_r\left(\frac{1}{r}\partial_r(r^5 T)\right) - \frac{2\nu_m}{r^2}\partial_r\left(r^2\partial_r\left(\frac{2}{r^2}\partial_r(r^3 C)\right)\right). \tag{12}$$

Here

$$\overline{\varepsilon}_m = \nu_m\left\langle \frac{\partial h_i}{\partial x_j}\frac{\partial h_i}{\partial x_j}\right\rangle = \nu_m\langle(\operatorname{curl}\mathbf{h})^2\rangle, \tag{13}$$

$$\overline{\eta}_m = \nu_m\left\langle \frac{\partial a_i}{\partial x_j}\frac{\partial h_i}{\partial x_j}\right\rangle = \nu_m\langle\mathbf{h}\cdot\operatorname{curl}\mathbf{h}\rangle \tag{14}$$

are, respectively, the dissipation of the magnetic energy and helicity. Successive integration with allowance for the regularity of the behavior as $r\to 0$ gives

$$-\frac{4}{3}\overline{\varepsilon}_m - \partial_t B_{rr} = -\frac{8f}{r^4}\partial_r(r^5 V) - \frac{2\nu_m}{r^4}\partial_r(r^4\partial_r B_{rr}), \tag{15}$$

$$-\frac{\overline{\eta}_m}{3}-\partial_t C=-\frac{2f}{r^4}\partial_r(r^5T)-\frac{2\nu_m}{r^4}\partial_r(r^4\partial_r C). \tag{16}$$

In the inertial range the time derivatives and dissipation can be neglected, and it is found that the functions T and V depend only on the rates of dissipation of the magnetic energy and the helicity and are, respectively,

$$V=\frac{\overline{\varepsilon}_m/f}{30}, \quad T=\frac{\overline{\eta}_m/f}{30}. \tag{17}$$

Therefore the rank-3 two-point correlation tensor for magnetic field fluctuations becomes

$$\langle h_i(\mathbf{x})h_j(\mathbf{x})h_k(\mathbf{x}+\mathbf{r})\rangle=\frac{\overline{\varepsilon}_m/f}{30}(\varepsilon_{jkl}r_i+\varepsilon_{ikl}r_j)r_l-\frac{\overline{\eta}_m/f}{10}\left(r_i\delta_{jk}+r_j\delta_{ik}-\frac{2}{3}\delta_{ij}r_k\right). \tag{18}$$

It should be noted especially that up to numerical factors the tensor (18) of coefficients is identical to the corresponding correlation tensor of the velocity fluctuations in hydrodynamic turbulence.[4]

Let us decompose the magnetic field into longitudinal and transverse components

$$\mathbf{h}_l=(\mathbf{h}\cdot\mathbf{r})\mathbf{r}/r^2, \quad \mathbf{h}_t=\mathbf{h}-\mathbf{h}_l,$$

$$\delta h_l(\mathbf{x}|\mathbf{r})=(\mathbf{h}_l(x+r)-\mathbf{h}_l(\mathbf{x}))\cdot\mathbf{r}/r.$$

In this notation we obtain

$$\langle\delta h_l(\mathbf{x}|\mathbf{r})^3\rangle=-24Tr=-\frac{4}{5}\frac{\overline{\eta}_m}{f}r, \tag{19}$$

$$\langle\delta\mathbf{h}_l(\mathbf{x}|\mathbf{r})\cdot[\mathbf{h}_t(x+r)\times\mathbf{h}_t(x)]\rangle=4Vr^2=\frac{2}{15}\frac{\overline{\varepsilon}_m}{f}r^2. \tag{20}$$

Therefore the 4/5 and 2/15 laws should hold in homogeneous and isotropic EMHD turbulence. As one can see from Eq. (19), it is much simpler to determine the helicity in EMHD turbulence than in hydrodynamics, where this requires especially accurate measurements of various velocity components or the use of delicate instruments to determine the gradients, whereas in EMHD it is sufficient to measure only the longitudinal components of the fluctuational magnetic fields or currents.

We underscore that no dimensional considerations were used to derive the relations for T and V, which involve the helicity and energy fluxes. This result, which is only a consequence of the statistical properties of the isotropic solutions of the EMHD equations, is universal and does not depend on which kind of turbulence — weak or strong — develops in the system.

It can be verified by direct substitution that taking the isotropy into account in the form of an external constant magnetic field $\mathbf{h}_0=\text{const}$ leads only to a modification of the results obtained. A dependence on the angle between the radius vector and the direction of the magnetic field will appear, since if homogeneity is preserved, the terms related to the external field ($\sim(\mathbf{h}_0\cdot\nabla)\operatorname{curl}\mathbf{h}$) will not appear in equations of the form (4) and (5) for the two-point correlation functions.

TABLE I.

	Hydrodynamics **v**	EMHD **h**
Nonlinearity	$[\mathrm{curl}\,\mathbf{v}\times\mathbf{v}]+\nabla(p+\mathbf{v}^2/2)$	$f\,\mathrm{curl}\,[\mathrm{curl}\,\mathbf{h}\times\mathbf{h}]$
Energy dissipation	$\overline{\varepsilon}=\nu\langle(\mathrm{curl}\,\mathbf{v})^2\rangle$	$\overline{\varepsilon_m}=\nu_m\langle(\mathrm{curl}\,\mathbf{h})^2\rangle$
	$\overline{\eta}=\nu\langle\mathrm{curl}\,\mathbf{v}\cdot\mathrm{curl}^2\mathbf{v}\rangle$	$\overline{\eta_m}=\nu_m\langle\mathbf{h}\cdot\mathrm{curl}\,\mathbf{h}\rangle$
4/5 law	$\langle\delta v_l(\mathbf{x}\|\mathbf{r}^3\rangle=-\frac{4}{5}\overline{\varepsilon}r$	$\langle\delta h_l(\mathbf{x}\|\mathbf{r})^3\rangle=-\frac{4}{5}\frac{\overline{\eta_m}}{f}r$
2/15 law	$\langle\delta\mathbf{v}_l(\mathbf{x}\|\mathbf{r})\cdot[\mathbf{v}_t(\mathbf{x}+\mathbf{r})\times\mathbf{v}_t(\mathbf{x})]\rangle$ $=\frac{2}{15}\overline{\eta}r^2$	$\langle\delta\mathbf{h}_l(\mathbf{x}\|\mathbf{r})\cdot[\mathbf{h}_t(\mathbf{x}+\mathbf{r})\times\mathbf{h}_t(\mathbf{x})\rangle$ $=\frac{2}{15}\frac{\overline{\varepsilon_m}}{f}r^2$

The ''extra'' curl in EMHD, as compared with the Navier–Stokes equation, leads to an unusual transposition — for longitudinal correlations the 4/5 law holds, just as in hydrodynamics, but it is related with the gyrotropic component of the fluctuations, i.e., the helicity flux and, conversely, mixed longitudinal–transverse correlations are related with the magnetic energy flux. Table I gives a comparative summary of the basic results.

In closing, I thank S. S. Moiseev for helpful discussions. This work was supported in part by the Russian Fund for Fundamental Research (Grant No. 98-02-17229) and INTAS (Joint Georgia–INTAS Project No. 504).

*e-mail: ochkheti@mx.iki.rssi.ru

[1] A. N. Kolmogorov, Dokl. Akad. Nauk SSSR **32**, 19 (1941).
[2] S. Chandrasekhar, Proc. Phys. Soc. London, Sect. A **204**, 435 (1951).
[3] O. G. Chkhetiani, JETP Lett. **63**, 808 (1996).
[4] V. S. L'vov, E. Podivilov, and I. Procaccia, http://xxx.lanl.gov/abs/chao-dyn/9705016.
[5] A. S. Monin and A. M. Yaglom, *Statistical Fluid Mechanics*, Vols. 1 and 2 (MIT Press, Cambridge, Mass., 1971 and 1975) [Russian original, Gidrometeoizdat, St. Petersburg, 1996, Part 2].
[6] L. Biferale, D. Pierotti, and F. Toschi, http://xxx.lanl.gov/abs/chao-dyn/9804004.
[7] U. Frisch, *Turbulence*, Cambridge University Press, New York, 1995.
[8] A. S. Kingsep, K. V. Chukbar, and V. V. Yan'kov, *Reviews of Plasma Physics*, Vol. 16, edited by B. B. Kadomtsev, Consultants Bureau, New York (1990) [Russian original, Voprosy Teorii Plazmy **16**, 209 (1987)].
[9] A. V. Gordeev, A. S. Kingsep, and L. I. Rudakov, Phys. Rep. **243**, 216 (1994).
[10] S. I. Vaĭnshteĭn, Usp. Fiz. Nauk **120**, 613 (1976) [Sov. Phys. Usp. **19**, 987 (1976)].
[11] V. M. Yakovenko, Zh. Éksp. Teor. Fiz. **57**, 554 (1968) [*sic*].
[12] V. N. Tsytovich, *Theory of Turbulent Plasma* (Plenum Press, New York, 1974) [Russian original, Énergoatomizdat, Moscow, 1971].
[13] M. A. Livshits and V. N. Tsytovich, Zh. Éksp. Teor. Fiz. **62**, 606 (1972) [Sov. Phys. JETP **35**, 321 (1972)].
[14] S. I. Vaĭnshteĭn, Zh. Éksp. Teor. Fiz. **64**, 139 (1973) [Sov. Phys. JETP **37**, 73 (1973)].
[15] L. D. Landau and E. M. Lifshitz, *Fluid Mechanics*, 2nd edition (Pergamon Press, New York, 1987) [Russian original, 3rd ed., Nauka, Moscow, 1986].

Translated by M. E. Alferieff

Effect of ordering on the structure and specific heat of nonstoichiometric titanium carbide

V. N. Lipatnikov* and A. I. Gusev

Institute of Solid-State Chemistry, Urals Branch of the Russian Academy of Sciences, 620219 Ekaterinburg, Russia

(Submitted 22 March 1999)
Pis'ma Zh. Éksp. Teor. Fiz. **69**, No. 9, 631–637 (10 May 1999)

The experimental results on the change in the crystal structure and specific heat of nonstoichiometric titanium carbide TiC_y ($0.5<y<0.65$) near disorder–order phase transitions are reported. It is established that at temperatures below 1000 K the ordered phases Ti_2C with cubic and trigonal symmetry and an orthorhombic ordered phase Ti_3C_2 form in titanium carbide by a close-to-first-order phase transition mechanism. The temperatures and heats of order–disorder phase transformations are determined. © *1999 American Institute of Physics.* [S0021-3640(99)00509-5]

PACS numbers: 61.66.Fn, 65.40.+g, 64.60.Cn

Titanium carbide TiC_y with a $B1$ (NaCl) type basal structure belongs to a group of highly nonstoichiometric compounds which includes cubic and hexagonal carbides, nitrides, and oxides MX_y and M_2X_y (M is a group-IV or -V transition metal, and X stands for C, N, or O). Even among highly nonstoichiometric compounds, titanium carbide TiC_y is unique, since it can exist even when more than half of all sites in its nonmetallic sublattice are vacant. No other compounds with such stability with respect to the formation of structural vacancies are known. The disordered titanium carbide TiC_y ($TiC_y\square_{1-y}$) possesses an exceptionally wide range of homogeneity — from $TiC_{0.48}$ to $TiC_{1.00}$ (Ref. 1), where the carbon atoms C and the structural vacancies $\square$ form a solution of substitution in the nonmetallic sublattice. The high concentration of structural vacancies creates the prerequisites for ordering of TiC_y carbide. Atom–vacancy ordering appreciably influences the structure and properties of highly nonstoichiometric carbides MC_y (Refs. 2 and 3).

Calculations[4] by the order-parameters functional method[1,5] show that three superstructures, Ti_2C, Ti_3C_2, and Ti_6C_5, can form upon the ordering of TiC_y carbide ($0.48 \leqslant y \leqslant 0.96$). According to the calculations of Ref. 6, which were performed by the Monte Carlo method for a narrower range of compositions $TiC_{0.55}$–$TiC_{0.70}$, in this part of the region of homogeneity of TiC_y at $T<950$ K the ordered phases Ti_2C and Ti_3C_2 are the thermodynamically equilibrium phases, in agreement with the theoretical results of Ref. 4. Ordered phases of the type Ti_2C with cubic (space group $Fd3m$) and trigonal (space group $R\bar{3}m$) symmetries have been observed experimentally in titanium carbide TiC_y in the range $0.5 \leqslant y \leqslant 0.7$ (Ref. 1). There is also indirect evidence of the formation of the ordered phase Ti_3C_2 (Ref. 6). Reports of a trigonal phase Ti_2C with space group

$P3_121$ are, of course, due to an error initially made in Ref. 7 and uncritically repeated in Refs. 8–11; indeed, on the basis of the $B1$ basal structure such an M_2C-type trigonal (space group $P3_121$) phase with unit cell periods $a=b=a_{B1}/\sqrt{2}$ ($a=\{1/2\ 1/2\ 0\}_{B1}$) and $c=3\sqrt{2}a_{B1}$ ($c=\{2\ 2\ 2\}_{B1}$) is fundamentally impossible, since sites of the metallic and nonmetallic lattices are partially coincident. Ordering of carbide TiC_y with a higher relative carbon content $y>0.7$ has practically escaped study.

The specific heat of titanium carbide has been studied very little. The temperature dependence of the specific heat of close-to-stoichiometric titanium carbide TiC_y with $y\approx 1.00$ at $T>300$ K is presented in Ref. 12. The specific heat of the carbides $TiC_{0.95}$ and $TiC_{0.99}$ in the temperature range 12–300 K has been measured in Ref. 13 by the adiabatic method. There are no published data on the specific heat of disordered nonstoichiometric titanium carbide TiC_y ($0.48<y\leqslant 1.00$) in the entire region of its homogeneity. In Ref. 14 it is shown by the adiabatic calorimetry method that in the temperature range 1.5–5.0 K the specific heat C_p of the annealed (ordered) carbide $TiC_{0.625}$ is 0.4–0.9 $mJ\cdot mole^{-1}K^{-1}$ less than C_p of the same carbide in a quenched disordered state. There is no other published information on the effect of ordering on the specific heat of nonstoichiometric carbide TiC_y.

In the present work we studied the effect of ordering on the crystal structure and specific heat of titanium carbide TiC_y. The specific heat is very sensitive to disorder–order phase transformations, and by studying the temperature dependence of $C_p(T)$ one can observe directly even weak effects associated with ordering.

Samples of nonstoichiometric titanium carbide $TiC_{0.54}$, $TiC_{0.58}$, and $TiC_{0.62}$ were synthesized by hot pressing of powdered mixtures of $TiC_{0.98}$ and metallic titanium in a highly pure argon atmosphere at temperature 1800–2000 K and pressing pressure 23–25 MPa. The phase composition and crystal structure of the synthesized TiC_y samples and the same samples after annealing or measurement of the specific heat were studied by x-ray diffraction in Cu$K\alpha$ radiation in a step-wise scanning mode with $\Delta 2\theta=0.02°$ for 2θ ranging from 14° to 130°. In measurements on annealed carbides the exposure time at each point was 5 s. All synthesized samples were homogeneous and contained only the disordered phase of TiC_y with $B1$ (NaCl) structure.

The specific heat was measured in a Netzsch DSC404 differential scanning calorimeter in the temperature range 300–1300 K in an atmosphere consisting of ''especially pure'' (OCh-grade) argon. The measurements were performed with heating and cooling rates of 20 $K\cdot min^{-1}$ and a 5 K step. To determine the heats of transitions in TiC_y accurately, calibration measurements were performed beforehand under the same conditions. High-purity aluminum Al and gold Au were used for calibration. Sapphire was used as the comparison standard in the calorimetric experiments.

To achieve an ordered state the synthesized samples were annealed for 340 h with temperature gradually decreasing from 1070 to 770 K; cooling from 770 to 300 K was performed at the rate 1 $K\cdot min^{-1}$. Annealing led to the appearance of superstructural reflections in the x-ray diffraction patterns of the carbides $TiC_{0.54}$, $TiC_{0.58}$, and $TiC_{0.62}$.

In the x-ray diffraction pattern of the annealed carbide $TiC_{0.54}$ the first superstructural peak with wave vector $|\mathbf{q}|=(2a_{B1}\sin\theta)/\lambda\approx 0.870$ is observed near $2\theta\approx 17.8$–17.9° and corresponds to the vector $\{1/2\ 1/2\ 1/2\}$ of length $|\mathbf{q}|\approx 0.866$ (here and below, superstructural vectors are given in units of $2\pi/a_{B1}$, where a_{B1} is the period of the disordered

*B*1-type basal structure). The next three superstructural reflections correspond to the vectors {3/2 1/2 1/2}, {3/2 3/2 1/2}, and {3/2 3/2 3/2} and are observed at the angles $2\theta \approx 34.5°$, 45.9°, and 55.4°. The superstructural reflection {3/2 3/2 1/2} is very weak. The position of the observed superstructural reflections and the absence of a trigonal splitting of the structural lines $(331)_{B1}$, $(420)_{B1}$, and $(422)_{B1}$ show that an ordered cubic (space group $Fd3m$) phase Ti_2C formed in the carbide $TiC_{0.54}$ as a result of annealing. All rays of the star $\{\mathbf{k}_9\}$ appear in the channel with the disorder–order phase transition TiC_y (space group $Fm3m$) $\leftrightarrow$ Ti_2C (space group $Fd3m$) (the description of all stars $\{\mathbf{k}_s\}$ of wave vectors of the first Brillouin zone of an fcc crystal and their rays is given in Ref. 1).

The diffraction pattern of the annealed carbide $TiC_{0.58}$ contains superstructural reflections {1/2 1/2 1/2}, {3/2 1/2 1/2}, and {3/2 3/2 3/2} near the angles $2\theta \approx 17.9°$, $\sim 34.4°$, and $\sim 55.4°$. There is no {3/2 3/2 1/2} reflection. An important difference between the x-ray diffraction pattern of the annealed carbide $TiC_{0.58}$ and that of the annealed carbide $TiC_{0.54}$ is the observed trigonal splitting of the structural lines $(220)_{B1}$, $(311)_{B1}$, $(331)_{B1}$, $(420)_{B1}$, and $(422)_{B1}$. This means that the trigonal (space group $R\bar{3}m$) ordered phase Ti_2C formed in the carbide $TiC_{0.58}$ as a result of annealing. It is also possible that the annealed carbide $TiC_{0.58}$ contains, together with the trigonal phase, a certain amount of the cubic ordered phase Ti_2C and a small quantity (5–7 mass%) of the phase Ti_3C_2. The channel with the disorder–order transition TiC_y (space group $Fm3m$) $\leftrightarrow$ Ti_2C (space group $R\bar{3}m$) includes one ray $\mathbf{k}_9^{(3)}$ of the star $\{\mathbf{k}_9\}$.

Superstructural reflections, which are not present in the x-ray diffraction patterns of the carbides $TiC_{0.54}$ and $TiC_{0.58}$, are observed in the diffraction pattern of the annealed carbide $TiC_{0.62}$ together with the reflections {1/2 1/2 1/2} ($2\theta \approx 18.0°$) and {3/2 3/2 3/2} ($2\theta \approx 55.2°$) corresponding to the trigonal (space group $R\bar{3}m$) ordered phase Ti_2C. These are reflections near $2\theta \approx 30.6–30.7°$, $\sim 41.2°$, $\sim 42.6°$, and $\sim 55.4-55.5°$, with wave vectors of length $|\mathbf{q}| \approx 1.488$, 1.970, 2.038, and 2.607. This analysis has shown that the first two reflections are related with the rays $\mathbf{k}_4^{(1)} = \{2/3\ 2/3\ 0\}$ and $\mathbf{k}_4^{(2)} = -\mathbf{k}_4^{(1)}$ of the star $\{\mathbf{k}_4\}$, and the next two reflections are associated with the rays $\mathbf{k}_3^{(3)} = \{1/3\ -2/3\ -1/2\}$, $\mathbf{k}_3^{(4)} = -\mathbf{k}_3^{(3)}$, $\mathbf{k}_3^{(5)} = \{-1/3\ 2/3\ -1/2\}$, and $\mathbf{k}_3^{(6)} = -\mathbf{k}_3^{(5)}$ of the star $\{\mathbf{k}_3\}$. According to Ref. 15, such a set of superstructural reflections can correspond only to the orthorhombic (space group $C222_1$) ordered phase Ti_3C_2, which forms via a transition channel including two rays of the star $\{\mathbf{k}_4\}$ and four rays of the star $\{\mathbf{k}_3\}$.

It has been suggested[6,8,16] that the cubic superstructure Ti_2C is metastable or exists in a narrow temperature range, so that we performed an additional experiment. The disordered carbides $TiC_{0.54}$ and $TiC_{0.58}$ were annealed at 1000 K for 135 h and then quenched to 300 K (quench rate $\sim 250\ \mathrm{K \cdot min^{-1}}$) to preserve the structural state attained by annealing. The diffraction patterns of the annealed carbides $TiC_{0.54}$ and $TiC_{0.58}$ were found to be the same as for these carbides after annealing with temperature decreasing slowly, but the intensity of the superstructural reflections was several times lower. From this it follows that the cubic and trigonal ordered phases Ti_2C exist in different concentration intervals and are stable at all temperatures below 1000 K.

The distribution functions $n(x_1, y_1, z_1)$ describing the probability of finding carbon atoms at the sites $\mathbf{r} = \{x_1\ y_1\ z_1\}$ in the ordered carbide phases TiC_y have the following forms:

$$Ti_2C(\text{space group } R\bar{3}m): n(x_1, y_1, z_1) = y - (\eta_9/2)\cos[\pi(x_1 - y_1 + z_1)], \quad (1)$$

$$\mathrm{Ti_2C}(\text{space group } Fd3m): n(x_1, y_1, z_1)$$
$$= y - (\eta_9/4)\{-\cos[\pi(x_1+y_1+z_1)] + \cos[\pi(-x_1+y_1+z_1)]$$
$$+ \cos[\pi(x_1-y_1+z_1)] + \cos[\pi(x_1+y_1-z_1)]\}, \quad (2)$$

$$\mathrm{Ti_3C_2}(\text{space group} C222_1): n(x_1, y_1, z_1)$$
$$= y - (\eta_4/3)\{(1/2)\cos[4\pi(x_1+y_1)/3] - (\sqrt{3}/2)\sin[4\pi(x_1+y_1)3]\} + (\eta_3/2)$$
$$\times\{(1/2+\sqrt{3}/6)\cos[\pi(2x_1-4y_1-3z_1)/3] + (1/2-\sqrt{3}/6)$$
$$\times \sin[\pi(2x_1-4y_1-3z_1)/3] + (1/2-\sqrt{3}/6)\cos[\pi(-2x_1+4y_1-3z_1)/3]$$
$$+ (1/2+\sqrt{3}/6)\sin[\pi(-2x_1+4y_1-3z_1)/3]\}, \quad (3)$$

where x_1, y_1, and z_1 are the coordinates of the sites of the nonmetallic face-centered cubic sublattice undergoing ordering; η_9, η_4, and η_3 are long-range order parameters corresponding to the stars of wave vectors whose rays form disorder–order transition channels. The distribution functions (1)–(3) possess all symmetry elements with respect to which a particular superstructure is invariant. The formation of Ti_3C superstructures is related with the Lifshits star $\{\mathbf{k}_9\}$ and can occur as a second-order phase transition, which does not preclude the possibility of a first-order transition. The superstructure Ti_3C_2 is described by two critical order parameters, which correspond to non-Lifshits stars $\{\mathbf{k}_4\}$ and $\{\mathbf{k}_3\}$, and it forms only by a first-order phase transition.

An overall lowering of symmetry (product of rotational and translational lowerings of symmetry) in the transitions $TiC_y \rightarrow Ti_2C$ (space group $R\bar{3}m$), $TiC_y \rightarrow Ti_2C$ (space group $Fd3m$), and $TiC_y \rightarrow Ti_3C$ (space group $C222_1$) is 2, 8, and 144, respectively.

When measuring the specific heat, effects due to an order–disorder equilibrium transition were observed in the dependences $C_p(T)$ in the heating regime, and effects due to an equilibrium transition from a high-temperature disordered into a low-temperature ordered state were observed on cooling.

On heating from 300 to 1000 K the specific heat C_p of the annealed carbide $TiC_{0.54}$ increases continuously as a result of the excitation of the phonon subsystem. Subsequently, a sharp jump in the specific heat is observed at the transition temperature $T_{\text{trans}} \approx 1000$ K (Fig. 1). This jump is due to the equilibrium order–disorder transformation Ti_2C (space group $Fd3m$) $\rightarrow TiC_{0.54}$. The peak in the specific heat near T_{trans} has more of a symmetric (Fig. 2) and not a λ form; the symmetry of the peak is more characteristic for a first-order than a second-order phase transition. Moreover, weak hysteresis of the specific heat is observed on cooling; this also confirms that the transition is close to a first-order transition. Temperature hysteresis near an order–disorder transition had previously been observed in the resistivity of nonstoichiometric titanium carbide.[17] The lattice period a_{B1} of the basal phase with $B1$ structure also increases by a small amount as a result of ordering. All this taken together makes it possible to interpret the reversible order–disorder transformation Ti_2C (space group $Fd3m$) $\leftrightarrow TiC_{0.54}$ as a weak first-order phase transition with a low latent heat of transformation.

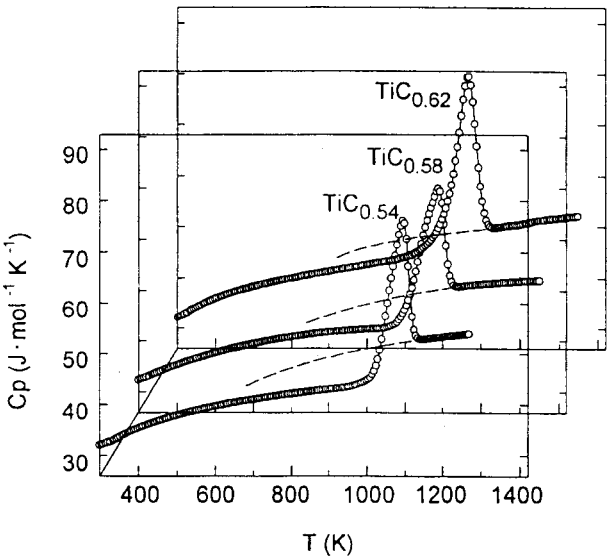

FIG. 1. Change in the specific heat $C_p(T)$ of annealed (ordered) nonstoichiometric titanium carbides $TiC_{0.54}$, $TiC_{0.58}$, and $TiC_{0.62}$ on heating: The dashed curves show the specific heat of the carbides TiC_y in a quenched nonequilibrium disordered state at temperatures $T<T_{trans}$.

The dependences $C_p(T)$ for the annealed carbides $TiC_{0.58}$ and $TiC_{0.62}$ (Fig. 1) have the same form as for the carbide $TiC_{0.54}$. However, the peak in the specific heat for the carbide $TiC_{0.58}$ can be represented as a superposition of two contributions (Fig. 2), one of which corresponds to the transformation $Ti_2C \rightarrow TiC_y$ and the other to the transformation

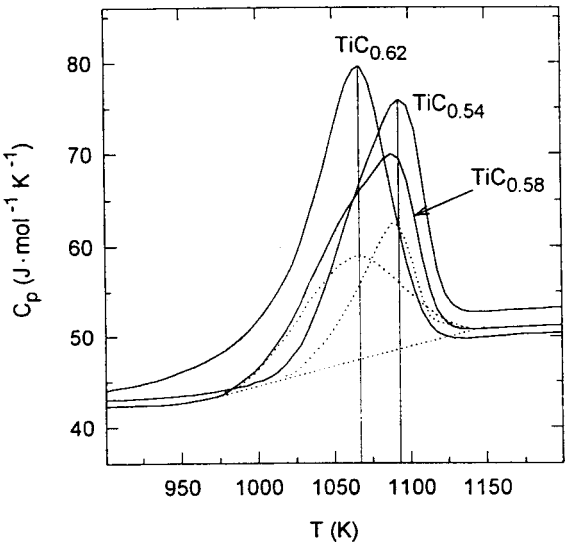

FIG. 2. Specific heat of the carbides $TiC_{0.54}$, $TiC_{0.58}$, and $TiC_{0.62}$ near the peaks corresponding to a transition from an ordered into a disordered state. Dotted curves — superpositional contributions to the specific heat of the carbide $TiC_{0.58}$ that correspond to the transformations $Ti_2C \rightarrow TiC_y$ and $Ti_3C_2 \rightarrow TiC_y$.

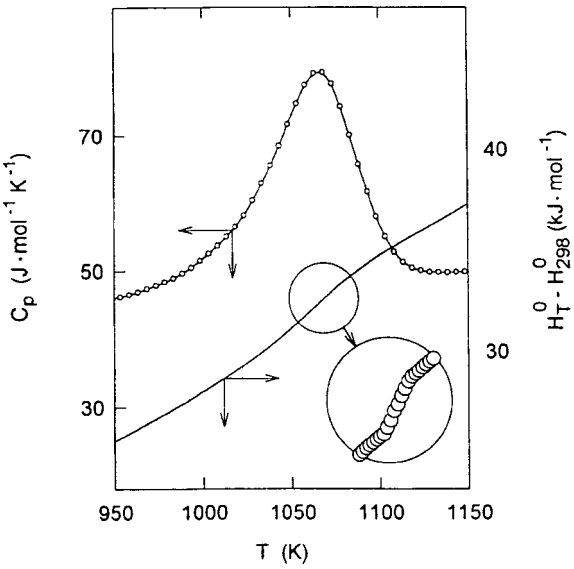

FIG. 3. Variation of the specific heat $C_p(T)$ and enthalpy $(H_T^0 - H_{298}^0)$ of the nonstoichiometric carbide $TiC_{0.62}$ near the reversible order–disorder phase transformation Ti_3C_2 (space group $C222_1$) $\leftrightarrow$ $TiC_{0.62}$: $T_{trans} = 970 \pm 10$ K and $\Delta H_{trans} = 1.8 \pm 0.2$ kJ·mole^{-1}.

$Ti_3C_2 \rightarrow TiC_y$. The peaks corresponding to these contributions are broadened compared with the peaks in the specific heat of the carbides $TiC_{0.54}$ and $TiC_{0.62}$. Apparently, the annealed carbide $TiC_{0.58}$ contains the ordered phases Ti_2C and Ti_3C_2, where the degree of long-range order is less than in the single-phase ordered carbides.

The most symmetric peak of the specific heat near an order–disorder transition is observed for the carbide $TiC_{0.62}$ (Fig. 2), in which a Ti_3C_2 phase forms. A symmetry analysis showed that the transformation $Ti_3C_2 \leftrightarrow TiC_y$ can only be a first-order transition. Figure 3 shows the change in the enthalpy $(H_T^0 - H_{298}^0)$ and specific heat $C_p(T)$ of the nonstoichiometric carbide $TiC_{0.62}$ near a phase transition: It is evident that a jump $(H_T^0 - H_{298}^0)$ in the enthalpy is observed at the transition temperature T_{trans}.

The measured temperatures T_{trans} and heats ΔH_{trans} of the phase transitions Ti_2C (space group $Fd\bar{3}m$) $\leftrightarrow$ $TiC_{0.54}$, Ti_2C (space group $R\bar{3}m$) $\leftrightarrow$ $TiC_{0.58}$, and Ti_3C_2 (space group $C222_1$) $\leftrightarrow$ $TiC_{0.62}$ studied are 1000, 980, and 970 K and 1.5 ± 0.2, 1.5 ± 0.2, and 1.8 ± 0.2 kJ·mole^{-1}, respectively.

The experimental data on the temperature dependence of the specific heat of ordered titanium carbides with different carbon content were approximated in the temperature range from 300 to 1000 K by the following equations:

$TiC_{0.54}$:

$$C_p(T) = 46.5538 + 1.1566 \times 10^{-3} T + 7.6604 \times 10^{-7} T^2 - 4631.8871 T^{-1} (\text{J} \cdot \text{mole}^{-1}\text{K}^{-1}).$$

$TiC_{0.58}$:

$$C_p(T) = 31.1767 + 2.7000 \times 10^{-3} T + 1.3772 \times 10^{-5} T^2 - 1775.7430 T^{-1} (\text{J} \cdot \text{mole}^{-1}\text{K}^{-1}).$$

$TiC_{0.62}$:

$$C_p(T) = 60.8874 - 2.7600\times10^{-3}T + 1.9196\times10^{-5}T^2 - 6793.1821T^{-1}(\text{J}\cdot\text{mole}^{-1}\text{K}^{-1}).$$

The disordered state of nonstoichiometric carbides is easily preserved as a metastable state at $T<T_{trans}$. As one can see from Fig. 1, near T_{trans} the specific heat of quenched disordered carbides TiC_y is greater than that of the same carbides in an equilibrium ordered state. This behavior of C_p of highly nonstoichiometric carbides MC_y near an order–disorder transition (the higher specific heat of the disordered carbide and the jump in the specific heat at the transition temperature) had been predicted in Ref. 18.

On the whole our study of the crystal structure and specific heat of titanium carbide TiC_y ($0.54\leqslant y\leqslant 0.62$) showed that ordering of TiC_y with formation of the cubic (space group $Fd3m$) and trigonal (space group $R\bar{3}m$) Ti_2C superstructures and orthorhombic (space group $C222_1$) Ti_3C_2 superstructure occurs at temperature 970–1000 K as a first-order transition. The results obtained agree with the phase diagram which is proposed in Ref. 17 for the system Ti–C and takes account of the ordering of the nonstoichiometric carbide TiC_y.

This work was supported by the Russian Fund for Fundamental Research (Project 98-03-32890a).

*e-mail: lipatnik@chem.ural.ru and/or gusev@chem.ural.ru

[1] A. I. Gusev and A. A. Rempel', *Structural Phase Transitions in Nonstoichiometric Compounds* [in Russian] (Nauka, Moscow, 1988).
[2] A. A. Rempel', Usp. Fiz. Nauk **166**, 33 (1996).
[3] A. I. Gusev and A. N. Zyryanova, JETP Lett. **69**, 324 (1999).
[4] A. I. Gusev and A. A. Rempel, J. Phys. Chem. Solids **55**, 299 (1994); Phys. Status Solidi A **163**, 273 (1997).
[5] A. I. Gusev, Philos. Mag. B **60**, 307 (1989).
[6] C. H. de Novion, B. Beuneu, T. Priem *et al.*, in *The Physics and Chemistry of Carbides, Nitrides and Borides*, edited by R. Freer (Kluwer Academic Publishers, Netherlands, 1990), p. 329.
[7] B. V. Khaenko and V. V. Ḳukol', Kristallografiya **34**, 1513 (1989) [Sov. Phys. Crystallogr. **34**, 905 (1989)].
[8] M. Yu. Tashmetov, V. T. Ém, M. U. Kanalov, and V. M. Shkiro, Preprint *P*8-507 [in Russian], Institute of Nuclear Physics, Uzbek SSR Academy of Sciences, 12 (1990); Metallofiz. **13**, 100 (1991).
[9] V. T. Ém and M. Yu. Tashmetov, Fiz. Met. Metalloved. **73**, 112 (1992).
[10] M. Yu. Tashmetov, V. T. Ém, and N. N. Mukhtarova, Metallofizika (Kiev) **17**(8), 51 (1995).
[11] M. Yu. Tashmetov, V. T. Ém, and B. N. Savenko, Fiz. Tverd. Tela (St. Petersburg) **39**, 2207 (1997) [Phys. Solid State **39**, 1968 (1997)].
[12] E. K. Storm, *The Refractory Carbides* (Academic Press, New York, 1967).
[13] V. E. Ganenko, G. A. Berezovskiĭ, V. S. Neshpor, and G. N. Klimashin, in *Works on Solid-State Physics* [in Russian], (Nauka, Novosibirsk, 1968), No. 3, p. 127.
[14] N. Lorenzelli, R. Caudron, J. P. Landesman, and C. H. de Novion, Solid State Commun. **59**, 765 (1986).
[15] A. I. Gusev and A. A. Rempel, Phys. Status Solidi A **135**, 15 (1993).
[16] V. Moisy-Maurice, N. Lorenzelli, C. H. de Novion, and P. Convert, Acta Metall. **30**, 1769 (1982).
[17] V. N. Lipatnikov, A. Kottar, L. V. Zueva, and A. I. Gusev, Fiz. Tverd. Tela (St. Petersburg) **40**, 1332 (1998) [Phys. Solid State **40**, 1211 (1998)].
[18] A. I. Gusev, A. A. Rempel', and V. N. Lipatnikov, Zh. Fiz. Khim. **64**, 2343 (1990); Phys. Status Solidi B **194**, 467 (1996).

Translated by M. E. Alferieff

On resonance states in ''split'' germanium

A. T. Dalakyan and V. N. Tulupenko*
Donbass State Machine Building Academy, 343913 Kramatorsk, Ukraine

D. A. Firsov
St. Petersburg State Technical University, 195251 St. Petersburg, Russia

V. M. Bondar
Institute of Physics, Ukrainian National Academy of Sciences, 252650 Kiev, Ukraine

(Submitted 25 March 1999)
Pis'ma Zh. Éksp. Teor. Fiz. **69**, No. 9, 638–642 (10 May 1999)

Maxima have been observed experimentally in the dependences of the current on the uniaxial pressure in *p*-type germanium for crossed directions of the uniaxial strain and electric field. The effect, which is observed at $T=77$ K and is absent at $T=4.2$ K, can be explained by tunneling transitions of holes, with the participation of acoustic phonons, from a resonant impurity state to unoccupied states in the valence subbands of germanium. © *1999 American Institute of Physics.* [S0021-3640(99)00609-X]

PACS numbers: 72.80.Cw, 62.50.+p, 72.20.Jv

INTRODUCTION

Induced far-IR emission from hot holes in Ge with an electric field and uniaxial pressure (UP) applied in the same direction was observed at $T=4.2$ K in Ref. 1. The emission is accompanied by a severalfold jump in the current flowing through the sample. This emission arises at total internal reflection modes for sufficiently strong electric fields $E>3$ kV/cm and UPs $X>8$ kbar. In Ref. 2 it is shown that the threshold pressure for the appearance of radiation and the current jump decreases with increasing impurity density and increases with increasing temperature. Spectral investigations[3] have established that the radiation is due to intracenter inversion in the hole distribution. The point is that the UP lifts the degeneracy of the valence subbands and impurity levels, each level following its subband as pressure increases. For $k=0$ the splitting Δ of the subbands (see Fig. 1) is proportional to the UP, $\Delta=\alpha X$ (Ref. 4), with the following splitting parameters α for UPs applied along the crystallographic axes $\mathbf{X}\|[100]$ and $\mathbf{X}\|[111]$: $\alpha_{100}=6$ meV/kbar and $\alpha_{111}=4$ meV/kbar. At splittings $\Delta\geqslant 16$ meV the upper impurity level ϵ_+ falls into the continuous spectrum of the bottom sublevel ϵ_{-p} and therefore becomes resonant.[4] As a result, and since the depth δ_+ of this level relative to its own subband is approximately two times greater than the corresponding depth δ_- (for pressures such that $\Delta-\delta_+<\delta_+$), a population inversion on these levels is produced in a strong electric field. However, as shown in Refs. 2 and 3, the presence of a static domain with a strong electric field (which vanishes at the moment radiation generation arises) in the sample impedes the appearance of intracenter inversion and gives rise to large threshold UPs. A static

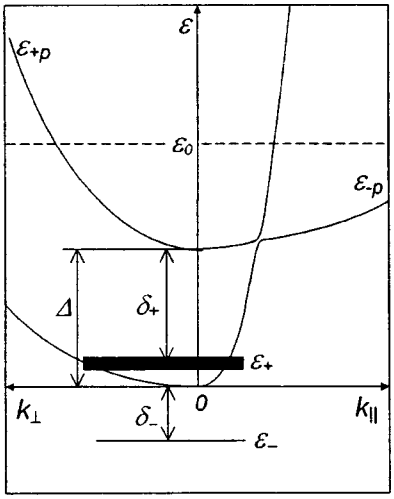

FIG. 1. Schematic diagram of the structure of the valence band of uniaxially strained germanium.

domain forms because of the presence of holes with different masses in the direction of strain in the bottom subband[5] — light holes for hole energies less than the energy corresponding to the inflection point on the dispersion curve (see Fig. 1) and heavy holes for holes with energy greater than the energy corresponding to the inflection point. In addition, a clear dependence of the threshold pressures on the crystallographic directions ([100] or [111]), along which the electric field is applied, is not observed in the experiment of Ref. 2, though for them the splitting parameters differ substantially. The latter circumstance is also explained by the presence of a static domain.[6]

At the same time, for mutually perpendicular UP and electric-field directions, the conditions for the formation of a static domain are not satisfied, since there are no inflections in the dispersion curve. Therefore it can be expected that in this case the presence of resonance impurity states can be observed for UPs much less than 8 kbar. On this basis our objective in the present work was to observe and investigate the possible influence of resonance impurity states on electric-current flow through a sample with crossed directions of the electric field and the UP.

2. EXPERIMENT

The experiments were performed at $T=77$ and 4.2 K. At $T=77$ K the current-voltage and pressure-current dependences were investigated for samples in the form of a cross and a rectangle, while only rectangular samples were used at $T=4.2$ K.

The choice of sample shape was dictated by the following circumstances. In the first place, if for $\mathbf{E}\parallel\mathbf{X}\parallel[111]$ increasing the UP suppresses the injection of nonequilibrium current carriers (electrons) from the contacts, then electron injection is easier for $\mathbf{E}\perp\mathbf{X}\parallel[111]$. This is due to the fact that for electric field and UP oriented in the same directions the effective conduction mass of an electron in the bottom split-off valley increases, while for electric field perpendicular to the UP, it decreases. For this reason, to interpret the results obtained correctly it is necessary to eliminate any influence of the

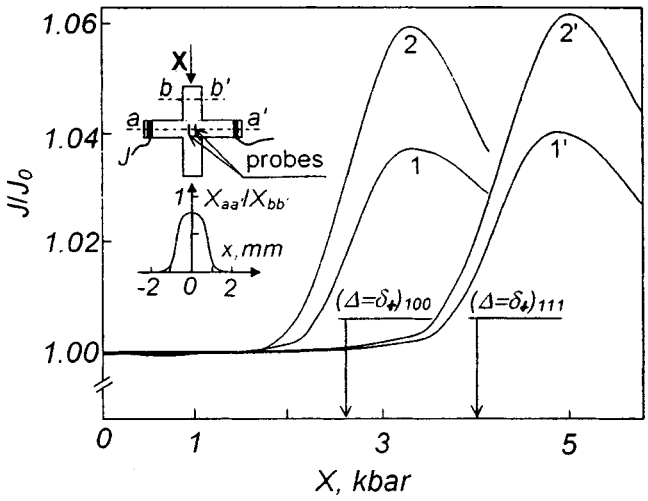

FIG. 2. Normalized current (J_0 is the current at $X=0$) versus the uniaxial pressure X for a cross-shaped sample; $t=77$ K; E, kV/cm: 0.75 — curves *1,1′*; 1.0 — *2,2′*. Hole density $N_A-N_D=8\times10^{13}$ cm^{-3}; $\mathbf{E}\perp\mathbf{X}\|[100]$ — curves *1,2*; $\mathbf{E}\perp\mathbf{X}\|[111]$ — *1′,2′*. Inset: Measurement scheme and the distribution of mechanical stresses on the cross-shaped sample.

injected electrons on the experimental results. In the second place, the effect of uniaxial strain on the properties of the contacts deposited over the entire length of a sample was unclear. On this basis at the first stage the samples were cut out in the shape of a cross, and the mechanical stresses at the center were calculated by the finite-element method. A check of the calculation according to the position of the maximum of the transverse piezoelectric resistance[7] for rectangular samples showed that the computed and experimentally measured positions of the maximum of the piezoelectric resistance were the same to within a quite high accuracy of 5%. The shape and dimensions of the experimental samples and the distribution of the mechanical stresses in the section aa' are shown in the inset in Fig. 2. It is evident that the contacts are located outside the zone of the mechanical stresses. The intensity of the electric field at the center of the samples was measured with capacitive probes.

At the second stage the experiments were performed on rectangular samples with contacts deposited along the entire area of the long faces. We note that such a sample shape is most favorable for generation of longitudinal (with respect to the length of the sample) IR-radiation modes. Comparing the pressure–current curves with the analogous curves obtained for the cross-shaped samples showed that mechanical loads up to 6 kbar did not change the properties of the contacts. The same conclusion was also confirmed by repeated measurements of the transverse piezoelectric resistance and current-voltage characteristics of the rectangular samples, and the reproducibility of the results was quite high — around 1% for high-resistance samples and 1.5% for doped samples. The duration of the strong electric field pulses was 120 ns with a 20–30 ns rise time. The appearance of nonequilibrium-carrier injection was monitored according to the shape of the current pulse and for some samples according to the decrease in the Hall constant. For this purpose, permanent magnets were placed next to the sample. The Hall contacts were

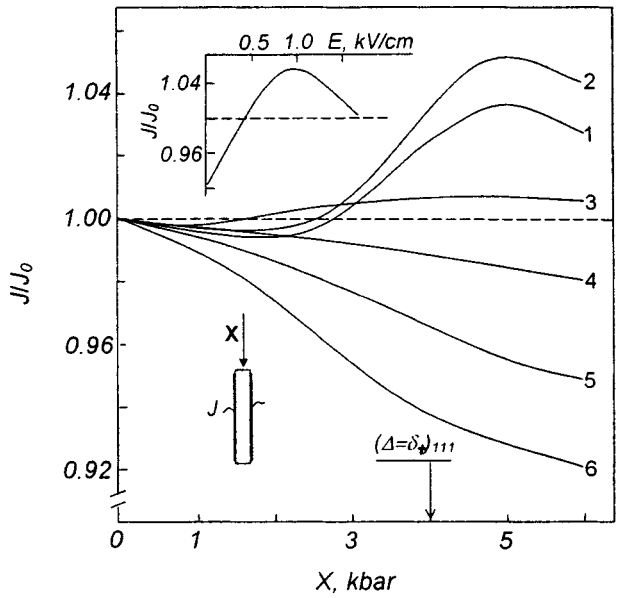

FIG. 3. Same as Fig. 2 for rectangular samples ($\mathbf{E}\perp\mathbf{X}\|[111]$). Initial temperature T_0, K: 77 — curves *1–3*; 4.2 — *4–6*. *E*, kV/cm: 0.5 — *1,4*; 1.0 — *2,5*; 1.25 — *6*; 1.5 — *3*. Hole density $N_A-N_D=6.8\times10^{14}$ cm^{-3}. Insets: Top — normalized current versus the electric field strength with uniaxial pressure $X=5$ kbar ($T_0=77$ K); bottom — sample shape and measurement scheme.

led out through dies. Such double monitoring made it possible to perform measurements on rectangular samples in fields where electron injection had no effect on the results obtained. Loads were applied to the samples in a manner similar to that used in Ref. 2.

DISCUSSION

The experimental results are presented in Figs. 2 and 3. We discuss first the results obtained at $T=4.2$ K. The decrease of the current at liquid-helium temperature within the curves 4–6 in Fig. 3 can be explained by the decrease in the density of states in the lower subband ϵ_{-p} with increasing pressure and by the effective capture of holes in the resonance states.[8] An increase in the average hole energy with increasing electric field E results in an increase of the hole effective mass m_1 in the ϵ_{-p} subband (for example, for $\mathbf{X}\|[111]$ $m_1|_{\epsilon=7\text{ meV}}/m_1|_{\epsilon=20\text{ meV}}\approx0.8$), as a result of which the normalized current should decrease with increasing electric field. In Fig. 3 this is reflected as a lowering of the curves 4–6 as the curve number increases, which corresponds to an increase in the electric field.

The position of the maxima on the pressure scale at $T=77$ K makes it possible to attribute them to the appearance of resonance impurity states. We underscore that the maxima are observed only at liquid-nitrogen temperature, and their magnitude depends on the electric field. The top inset in Fig. 3 shows the dependence of the normalized current on the electric field at 5 kbar pressure (the pressure at which maxima are observed). This curve was constructed on the basis of an analysis of nine curves similar to the curves 1–3 in Fig. 3. On this basis it can be inferred that the current growth in the

curves 1–3 in Fig. 3 (see also Fig. 2) is due to emptying of the bound states ϵ_+ in an electric field and, correspondingly, an increase in the number of holes contributing to the electric current. For $E=0$ the equilibrium population of the resonant states is determined mainly by scattering of holes by acoustic phonons. When an electric field is switched on, the rate of escape of holes from a resonant state increases is higher than in the equilibrium situation, while the rate of arrival into these states remains essentially unchanged. A hole which has left the level ϵ_+ can remain within the bottom subband ϵ_{-p} and it can also occupy the upper subband ϵ_{+p}. We note that in either case tunneling of a hole in an electric field with absorption of an acoustic phonon is assumed. In both cases the phonon energy required for a hole to be transferred out of the resonant state will be less than for $E=0$. For example, in the second case the energy of the absorbed phonons can be less than the gap width, determined by the dispersion law for holes in the upper subband $(\epsilon_{+p}(p)-\epsilon_+)|_{E=0}$, as a result of the decrease in the gap with an electric field, increasing the probability of such processes. Moreover, we underscore that the hole effective mass in the upper subband is approximately three times less than in the bottom subband, and the hole contribution to the electric conductivity will be much higher.

The decrease of the current component due to holes in the subband ϵ_{-p} with a further increase of pressure could be due to (just as in the case $T=4.2$ K) a decrease in the density of states in the bottom subband. The contribution of the upper subband to the hole current also will decrease, first, because of the decrease in the probability of holes being transferred out of the lower subband (the level ϵ_+ is broadened and correspondingly the lifetime of a hole in the level and the capture probability decrease) and, second, because the intensity of hole scattering with emission of an optical phonon with energy ϵ_0 with the final state of the hole in the bottom subband increases. The latter factor is due to the fact that the difference $\epsilon_0-\epsilon_+(p)$ decreases with increasing pressure for all holes with momentum p in the upper subband below the optical phonon energy ϵ_0, which in an electric field causes their lifetime with respect to the emission of an optical phonon to decrease. Since the direction-averaged density of states in the upper subband is approximately 20 times lower than in the bottom subband (for holes with the same energy), even holes with $\epsilon\approx 2\epsilon_0$ will be scattered primarily into the bottom subband.

We shall now examine the decrease of the electric current with increasing electric field intensity at 5 kbar pressure (see top inset in Fig. 3). For holes in the bottom subband such behavior of the current can be explained by analogy to the dependence $J(X)$ at $T=4.2$ K, specifically, by the increase in the hole effective mass with increasing hole energy. For holes in the subband ϵ_{+p} increasing the field heats up the holes and therefore increases the intensity of hole scattering by optical phonons with the final state in the subband ϵ_{-p}, which likewise decreases the current.

In conclusion, we note that the relative contribution of holes from each subband to the experimentally observed current maximum can be estimated on the basis of calculations matched with experiment.

We thank O. G. Sarbeĭ and M. S. Kagan for fruitful and stimulating discussions of this work.

This work was supported by the Ukrainian Fund for Fundamental Research (Grant 2.4/970), the Russian Fund for Fundamental Research (Grant 99/02-17102), and Grant NATO CNS 970627.

*e-mail: tvn@laser.donetsk.ua

[1] I. V. Altukhov, M. S. Kagan, and V. N. Sinis, JETP Lett. **47**, 164 (1988).
[2] V. G. Belykh, A. T. Dalakyan, V. N. Tulupenko, and D. A. Firsov, Fiz. Tekh. Poluprovodn. **29,** 1764 (1995) [Semiconductors **29**, 921 (1995)].
[3] I. V. Altukhov, M. S. Kagan, K. A. Korolev, and V. N. Sinis, JETP Lett. **59**, 476 (1994).
[4] G. L. Bir and G. E. Pikus, *Symmetry and Strain-Induced Effects in Semiconductors* (Wiley, New York, 1975) [Russian original, Nauka, Moscow, 1972].
[5] B. K. Ridley and T. B. Watkins, Proc. Phys. Soc. **78**, 293 (1961).
[6] V. N. Tulupenko, Ukr. Fiz. Zh. **42**, 1227 (1997).
[7] P. I. Baranskiĭ, V. Ya. Duchal, V. V. Kolomiets, and V. V. Chernysh, Fiz. Tekh. Poluprovodn. **20,** 2112 (1986) [Sov. Phys. Semicond. **20**, 1319 (1986)].
[8] I. V. Altukhov, M. S. Kagan, K. A. Korolev *et al.*, Zh. Éksp. Teor. Fiz. **115**, 89 (1999) [JETP **88**, 51 (1999)].

Translated by M. E. Alferieff

Kosterlitz–Thouless transition and radiation defects in a superconducting thin film

A. N. Artemov*

Donetsk Physicotechnical Institute, Ukrainian National Academy of Sciences, 340114 Donetsk, Ukraine

(Submitted 1 March 1999; resubmitted 29 March 1999)
Pis'ma Zh. Éksp. Teor. Fiz. **69**, No. 9, 643–648 (10 May 1999)

The thermodynamics of a system of Pearl vortices in a superconducting thin film containing radiation defects is studied. It is shown that three phase transition scenarios are possible, depending on the defect density. At low densities there is one stable state of the system. When the first critical density n_{d1} is reached, there appears a temperature interval in which the system can be in two stable states. If the density exceeds n_{d2}, then the lower limit of stability of the metastable states shifts abruptly to zero. © *1999 American Institute of Physics.*
[S0021-3640(99)00709-4]

PACS numbers: 74.76.−w, 74.80.Dm, 61.82.−d

A Kosterlitz–Thouless (KT) transition[1,2] occurs in two-dimensional systems in which topological defects with a Coulomb interaction can exist. An example of a model two-dimensional superconducting system is a layered superconductor without a Josephson link between the layers and with two-dimensional magnetic vortices as the topological defects. The KT transition in such a system is due to two phenomena — instability of vortex dipoles with respect to dissociation into a gas of free vortices, appearing in the system above the temperature[3,4]

$$T_{\mathrm{KT}}=\frac{\phi_0^2}{16\pi^2\Lambda(T_{\mathrm{KT}})}, \tag{1}$$

and collective effects in the system of free vortices. Here ϕ_0 is the magnetic flux quantum, $\Lambda=2\lambda^2/s$, λ is the London length, and s is the period of the system.

A superconducting thin film with thickness $d\ll\lambda$ is not a strictly two-dimensional system. Vortices in such a system have been studied by Pearl.[5] The logarithmic interaction of vortices in a film is bounded by the large but finite effective Pearl length $\Lambda=2\lambda^2/d$. Nonetheless, as was shown in Ref. 6, processes which allow a behavior of the system close to a KT transition can occur in a system of Pearl vortices. These are the same instability and collective effects that give rise to a KT transition in a two-dimensional system. However, in a system of Pearl vortices the correlation length cannot exceed Λ, while in a two-dimensional system the Pearl length approaches infinity as the temperature T_{KT} is approached from above. For this reason, in a Pearl film the phenom-

ena that are known as a KT transition do not constitute a phase transition in the strict sense.

In recent years there has been steady interest in the effect of radiation (columnar) defects on the properties of layered superconductors (see, for example, Refs. 7 and 8). These defects are formed by irradiating the samples with high-energy heavy-ion beams. They consist of nonsuperconducting regions with transverse dimensions of the order of the coherence length ξ of the superconductor. It has been shown that introduction of radiation defects is an effective method for intensifying the pinning of magnetic vortices and thereby increasing the critical current.

Since the behavior of systems of two-dimensional and Pearl vortices is determined by the same processes, it is natural to expect that radiation defects will also have the same influence. Their role consists in trapping and confining Pearl vortices, preventing their motion under the action of the current.

Thermal fluctuations have a different effect on the system of vortices in a superconductor. It is manifested, for example, in a fluctuational detachment of vortices from pinning centers, resulting in magnetic flux creep and decreasing the critical current. At low temperatures, fluctuations in a superconducting thin film lead to the production of pairs of oppositely directed Pearl vortices and a very small number of free vortices. Breakup of vortex pairs by a current results in a nonlinear current–voltage characteristic (IVC). As the temperature T of the superconductor increases to the critical temperature T_{KT} of the KT phase transition, instability leading to avalanche-like growth of the number of free vortices, giving rise to a linear behavior of the IVC, appears in the system of vortices. In a superconductor with pinning centers, such growth of the number of free vortices can lead to reversible behavior of the system. The thermodynamics of a system of Pearl vortices in a perfect thin film has been studied by Ryzhov and Tareyeva.[9]

In the present letter the influence of radiation defects on the KT transition in a superconducting thin film is studied. It is shown that, depending on the defect density n_d, three different phase transition scenarios are possible. For low n_d, less than a critical density n_{d1}, the transition is continuous, like a second-order transition. For $n_{d1}<n_d<n_{d2}$ there exist two thermodynamically equilibrium states of free vortices — individual and collective. A phase transition then occurs as a first-order transition, and hysteresis should be observed in the temperature dependence of the resistance. At a high defect density $n_d>n_{d2}$ the lower limit of stability of the metastable states shifts to $T=0$. In this situation the possibility of a transition of the system to a lower metastable state is very unlikely.

We shall treat Pearl vortices as classical massless particles. They can be in a free state or they can be trapped by radiation defects. We shall treat free and trapped vortices as two subsystems in thermal and chemical contact with each other. Free vortices can appear and disappear in such a system as a result of dissociation and recombination of vortex dipoles, and they can be trapped by and escape from defects. In an equilibrium state the temperatures and chemical potentials of the subsystems are the same.

We shall write down the partition function of the system of vortices in a film with defects. In a real film defects form a random configuration determined by the coordinates $\{\mathbf{R}_\alpha\}$. Let the system contain N_+ and N_- free vortices with two orientations, N_{t+} and N_{t-} vortices trapped by defects, and $N_d>N_{t+}+N_{t-}$ radiation defects. Then

$$Z(N_{\pm},N_{t\pm})=e^{-\beta F}=\frac{1}{N_{+}!N_{-}!N_{t+}!N_{t-}!}\left(e^{-\beta E_0}\int\frac{d\mathbf{x}}{\pi\xi^2}\right)^{N_{+}+N_{-}}$$
$$\times\sum_{\{\mathbf{R}_\alpha\}}\exp\left\{-\sum_{ij}\beta U(\mathbf{x}_i-\mathbf{x}_j)-\sum_{i\alpha}\beta U(\mathbf{x}_i-\mathbf{R}_\alpha)-\sum_{\alpha\gamma}\beta U(\mathbf{R}_\alpha-\mathbf{R}_\gamma)\right\}. \quad (2)$$

Here $\beta=1/T$, E_0 is the energy of a vortex core, $\pi\xi^2$ is the size of a cell in the space occupied by one vortex, and U is the interaction energy of free vortices located at the points $\mathbf{x}_i$ and trapped by defects located the points $\mathbf{R}_\alpha$. The contribution to the partition function from vortex dipoles due to the polarization of the medium and the interaction (see below) of vortices with empty defects has been neglected.

The free energy must be averaged over the arrangement of the defects. It is obvious that after averaging the energy of the system will no longer depend on which of the defects have trapped vortices. For this reason, in expression (2) the sum over various configurations of trapped vortices can be replaced by the number of possible configurations and averaged over one of them. The number of configurations equals the number of ways in which $N_{t+}+N_{t-}$ vortices can be distributed over N_d defects. It is easy to see that this number is $N_d!/(N_d-N_{t+}-N_{t-})!$.

We shall now discuss the averaging of the free energy. Only the configurational part of the energy needs to be averaged, since the entropy part does not depend on the coordinates of the defects. To calculate the configurational energy we shall formally expand the exponential function in Eq. (2) in a series. As is well known,[10] the logarithm of the partition function can be expanded in a series of connected diagrams. To perform the averaging we shall assume that all defects are distributed independently of one another and with equal probability over the entire area of the sample. We shall perform the averaging by integrating the formal series obtained over the coordinates of the defects and dividing each integral by the area S. As a result of this operation, the contribution of trapped vortices, which in a specific configuration were pinned at definite points $\mathbf{R}_\alpha$, is formally included in the free energy of the system on an equal footing with the contribution of free vortices. The only difference is that the state of the vortices trapped by defects is energetically more favorable because of the zero-point energy of the core.

Now it is easy to calculate the free energy of the system of vortices. Since we are interested mainly in collective effects in a system of vortices, we shall confine ourselves to summing a sequence of ring diagrams.[10] A characteristic feature of systems where collective effects play the main role is that the integral $J=\int d\mathbf{r}U(\mathbf{r})$ over the infinite area of the film, corresponding to the simplest diagram, diverges. This integral does diverge for the interaction energy of Pearl vortices. This means that even for a low vortex density it is not possible to limit the calculation to the interaction of vortices with some number of nearest neighbors, and it is necessary to take into account the interaction of all of them with one another. The ring diagrams form the main sequence in the expansion of the configurational energy in this case.

The situation is different for the interaction of a vortex with an empty defect. The interaction energy of a Pearl vortex interacting with an empty cylindrical defect has been calculated in Ref. 11. It decreases with increasing distance from a defect much more

rapidly than the energy of interaction with a vortex. In this case the integral J converges, and the configurational energy can be expanded in a series in the vortex and defect densities. The first nonvanishing term in the series will be the second virial coefficient, which is proportional to the product of the vortex and defect densities. It will give terms in the equation of equilibrium which are proportional to the densities, which are small compared with the logarithms of the densities and can be dropped. On this basis, so as not to complicate the expressions, the contribution to the partition function from the interaction of vortices with empty defects is neglected from the outset.

The free energy of a system of Pearl vortices in the ring approximation has been calculated in Ref. 9. We need only to substitute the sum of the densities of free vortices and vortices trapped by defects for the vortex density in the configurational part. Introducing the dimensionless vortex density $n=(N/S)\pi\xi^2$ and free-energy density $f=(F/S)\pi\xi^2$, we write the free energy of the system as

$$
\begin{aligned}
f=&\,n_+(\ln n_+-1)+n_-(\ln n_--1)+n_{t+}(\ln n_{t+}-1)+n_{t-}(\ln n_{t-}-1)\\
&+(n_d-n_{t+}-n_{t-})(\ln(n_d-n_{t+}-n_{t-})-1)\\
&+p(n_++n_-+n_{t+}+n_{t-})(1-\ln 4p(n_++n_-+n_{t+}+n_{t-}))\\
&+\frac{1}{4\Lambda^2}G[16p\Lambda^2(n_++n_-+n_{t+}+n_{t-})]+(n_++n_-)pe_0,
\end{aligned}
$$

$$
G[x]=\frac{1}{2}\ln\frac{x}{4}+\sqrt{|1-x|}\begin{cases}\arctan\dfrac{1}{\sqrt{x-1}}-\dfrac{\pi}{2}, & x\geqslant 1\\[2ex] \dfrac{1}{2}\ln\dfrac{1+\sqrt{1-x}}{1-\sqrt{1-x}}, & x\leqslant 1\end{cases}. \tag{3}
$$

Here $pe_0=\beta E_0$ and $p=\phi_0^2/16\pi^2\Lambda T$.

A system of vortices in a thin film is a system with a variable number of particles. The equilibrium number of particles in such a system must be determined by minimizing the free energy, and the equilibrium chemical potential is zero. Thus we obtain the conditions of equilibrium of the system by equating to zero the derivatives of the free energy with respect to the number $n_\pm$ of free vortices and the number $n_{t\pm}$ of vortices trapped by defects:

$$
\begin{aligned}
&\ln n_\pm-p\ln 4p(n_++n_-+n_{t+}+n_{t-})\\
&\quad+4pG'[32p\Lambda(n_++n_-+n_{t+}+n_{t-})]+pe_0=0,\\
&\ln n_{t\pm}-\ln(n_d-n_{t+}-n_{t-})-p\ln 4p(n_++n_-+n_{t+}+n_{t-})\\
&\quad+4pG'[16p\Lambda(n_++n_-+n_{t+}+n_{t-})]=0.
\end{aligned}
\tag{4}
$$

Subtracting the equation for n_- from the equation for n_+ we find that $n_+=n_-$ in a state of equilibrium. The two other equations give $n_{t+}=n_{t-}$. This decreases the number of equations of equilibrium to two. In what follows we shall drop the $+$ and $-$ signs from the subscripts.

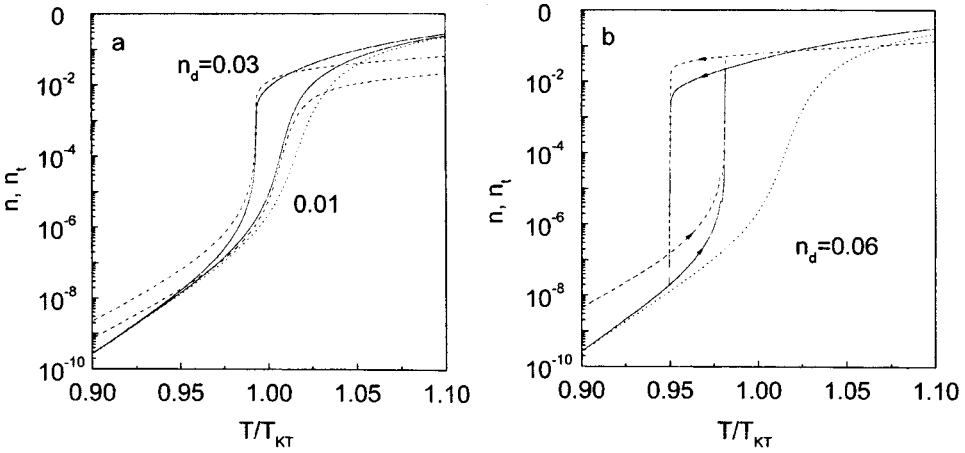

FIG. 1. Temperature dependence of the density of free vortices and the density of vortices trapped by defects for a continuous transition (a) and for a first-order transition (b).

The solutions of the system of equations obtained for various values of the defect density n_d are presented in Fig. 1. The temperature dependence of the density of free vortices (solid line) and trapped vortices (dashed line) at relatively low defect densities $n_d < n_{d1}$ varies continuously (Fig. 1a). The sharp change in the densities near the temperature T_{KT} is due to an instability similar to that predicted by Kosterlitz and Thouless[1] for strictly two-dimensional systems. The same instability is also observed in perfect films (dashed line), but in the presence of defects it is shifted in the direction of low temperatures.

At intermediate defect densities $n_{d1} < n_d < n_{d2}$ (Fig. 1b) there exists a temperature range in which the system of vortices possesses two stable states. In the state with the lower density the screening length $\delta = \xi/\sqrt{8p(n+n_t)}$ for the interaction of vortices is greater than the effective Pearl length Λ, and collective effects (screening) have only a weak effect on the state of the system. In the state with the higher density $\delta < \Lambda$, collective effects renormalize the interaction energy of the vortices and the energy now depends on the vortex density. This is a collective state of the system. Hysteresis of the resistance, which depends on the density of free vortices, should be observed in this density range.

For very high defect densities, $n_d > n_{d2}$, the left-hand stability limit of the metastable states shifts abruptly to $T = 0$. The system will always be in a collective state. A transition of the system to the lower state is unlikely.

A single general characteristic feature due to the existence of defects appears in all three scenarios. For any defect density, the density n of free vortices, to whose presence the resistive behavior of the superconductor is attributed, is higher than in a defect-free film, and the resistance jump shifts abruptly in the direction of lower temperatures.

This phenomenon can be explained as follows. In the absence of radiation defects the equilibrium density of free vortices is formed as a result of the establishment of dynamic equilibrium between dissociation and recombination of vortex dipoles. Defects

form an additional reservoir where vortices will accumulate, since the state of a trapped vortex is energetically more favorable on account of the energy of the core. As a result, at low temperatures in the state of the system where collective effects are negligible the density of trapped vortices is always higher than that of free vortices, and the density of free vortices is only negligibly higher than in a defect-free film. As the temperature T_{KT} is approached, the densities of both free and trapped vortices increase. This increases the influence of collective effects on the state of the system of vortices in perfect films and films containing defects. However, in the latter the total vortex density is higher, and collective effects cause the jump in the vortex density to occur at a lower temperature.

The numerical solutions presented were obtained for a model film with the parameters $e_0=3$, $\Lambda/\xi=10^2$ at $T=0$, and the ratio $T_{c0}/T_{\mathrm{KT}}=1.2$. The critical values of the dimensionless defect density for the indicated parameters $n_{d1}\approx 0.03$ and $n_{d2}\approx 0.09$ are quite large. They depend on these parameters, decreasing somewhat as the parameters decrease.

The described behavior of a system of Pearl vortices permits making a number of qualitative assertions about the critical current of a film. It follows from what has been said above that an increase of the critical current should not be observed in the absence of an external magnetic field. Conversely, the temperature at which resistive behavior of the film first appears decreases.

In an external magnetic field, an increase of the critical current due to trapping by the defects of vortices which have entered the sample under the action of a field can be observed at low temperatures. After the temperature at which avalanche-like growth of vortex density starts is reached, the critical current should go to zero, since the number of free vortices grows rapidly. This is one possible depinning mechanism by which a superconductor is brought to a resistive state and which gives rise to reversible behavior of the magnetization of the sample. In the case of a first-order transition, two lines of irreversibility can be observed, depending on the direction of change of the temperature in the experiment.

These remarks are equally applicable to layered superconductors, since the mechanisms responsible for the resistive behavior and magnetization of the sample are the same as in a Pearl film.

*e-mail: artemov@kinetic.ac.donetsk.ua

[1] J. M. Kosterlitz and D. J. Thouless, J. Phys. C **6**, 1181 (1973).
[2] V. L. Berezinskiĭ, Zh. Éksp. Teor. Fiz. **61**, 1144 (1972) [Sov. Phys. JETP **34**, 610 (1972)].
[3] J. R. Clem, Phys. Rev. B **43**, 7837 (1991).
[4] K. H. Fisher, Physica C **178**, 161 (1991).
[5] J. Pearl, Appl. Phys. Lett. **5**, 65 (1964).
[6] M. R. Beasley, J. E. Mooij, and T. P. Orlando, Phys. Rev. Lett. **42**, 1165 (1979).
[7] Qiang Li, Y. Fukumoto, Y. Zhu *et al.*, Phys. Rev. B **54**, R788 (1996).
[8] C. J. van der Beek, M. Konczykowski, T. W. Li *et al.*, Phys. Rev. B **54**, R792 (1996).
[9] V. N. Ryzhov and E. E. Tareyeva, Phys. Rev. B **49**, 6162 (1994).
[10] R. Balescu, *Equilibrium and Nonequilibrium Statistical Mechanics* (Wiley, New York, 1975; Mir, Moscow, 1978).
[11] J. L. Chen and T. Y. Tseng, Phys. Rev. B **54**, 502 (1996).

Translated by M. E. Alferieff

Characteristic features of anharmonic effects in the lattice dynamics of fcc metals

M. I. Katsnel'son
Institute of Metal Physics, Urals Branch of the Russian Academy of Sciences, 620219 Ekaterinburg, Russia

A. V. Trefilov and K. Yu. Khromov
Kurchatov Institute Russian Science Center, 123182 Moscow, Russia

(Submitted 30 March 1999)
Pis'ma Zh. Éksp. Teor. Fiz. **69**, No. 9, 649–652 (10 May 1999)

The dispersion in the entire Brillouin zone and the temperature dependence (right up to the melting temperature) of the anharmonic frequency shift and phonon damping in a number of fcc metals is investigated on the basis of microscopic calculations. It is found that the anharmonic effects depend sharply on the wave vector in the directions $\Gamma-X$, $X-W$, and $\Gamma-L$ and, in contrast to bcc metals, the magnitude of the effects is not due to the softness of the initial phonon spectrum. It is shown that the relative frequency shifts and the phonon damping near melting do not exceed 10–20%. The relative role of various anharmonic processes is examined, and the relation between the results obtained and existing experimental data is discussed. © *1999 American Institute of Physics.* [S0021-3640(99)00809-9]

PACS numbers: 63.20.Ry, 63.20.Dj

The investigation of anharmonic effects (AEs) in lattice dynamics is a classic problem of solid-state physics. It is important, specifically, because of the role that such effects they can play in phenomena associated with structural phase transitions and melting in crystals (see, for example, Refs. 1–3). At the same time, obtaining any information about the magnitude and scale of AEs from experiment and theory is a difficult problem. The experimental study of such ''basic'' AEs as the frequency shift and damping of phonons is very difficult and leads to a large uncertainty in the results (see, for example, the data presented in Refs. 4 and 5 for bcc and fcc metals, respectively). Up to now first-principles microscopic calculations of AEs have been performed for one point of the Brillouin zone (N) in the bcc phase of Zr and four points (N,P,ω,G) in Mo.[6] Detailed information about AEs in the entire Brillouin zone and their temperature dependence has been obtained in Refs. 4 and 7 on the basis of pseudopotential theory for the bcc phases of alkali and alkaline-earth metals. For these metals the most striking manifestations of AEs are due to the ''soft-mode behavior'' (the anomalous temperature dependence of the phonon frequencies) of the Σ_4 branch. It is of interest to calculate AEs for the ''general position,'' i.e., for crystals which do not possess soft vibrational modes. Such crystals include most metals with close-packed structures, for example, fcc. There is virtually no

information about AEs in such metals, not counting Ref. 5, where the damping of phonons in precious metals and Al was calculated. However, the calculations were performed only for individual points of the Brillouin zone and at room temperature (which is much less than the melting temperature T_m). Moreover, the accuracy of the model used in Ref. 5 for interatomic interactions is unclear, which is probably the reason for the qualitative discrepancy between the theoretical and experimental dependences of the damping on the wave vector. In the present letter the AEs in the lattice dynamics of fcc metals are investigated in detail on the basis of a systematic anharmonic perturbation theory.

The calculations were performed for Ir, the fcc phases of Ca and Sr, and the hypothetical fcc phase of K. This choice of objects was determined by the fact that reliable and at the same simple microscopic models which make it possible to describe a wide range of lattice properties of these metals exist.[4,7–9] Iridium is an example of an fcc crystal with a ''stiff'' interatomic interaction potential, similar to the Lennard-Jones potential,[8] while K, Ca, and Sr are characterized by potentials with a softer ''core.'' To demonstrate the characteristic features of AEs due to the specific nature of the potential with the same lattice geometry, we present here the results for the ''limiting'' cases — Ir and K. The results for Ca and Sr are qualitatively similar to the results for K and will be presented elsewhere.

The parameters determining the interatomic interaction potential are presented in Ref. 8 for Ir and in Ref. 4 for K. The calculations were performed on the basis of the anharmonic perturbation theory taking account of thermal expansion (quasiharmonic contributions, qh) and three- and four-phonon interaction processes to accuracy $\varkappa^2$, where $\varkappa=(m/M)^{1/4}$ is the adiabatic smallness parameter, and m and M are the electron and ion masses. The exact formulas actually used in the calculations are presented in Ref. 4. For a qualitative discussion of the results, we present here their high-temperature asymptotic representation for $T>\Theta_D$ (Θ_D is the Debye temperature):

$$\Delta_{\lambda\mathbf{k}}=\Delta^{qh}_{\lambda\mathbf{k}}+\Delta^{3}_{\lambda\mathbf{k}}+\Delta^{4}_{\lambda\mathbf{k}}, \tag{1}$$

$$\Delta^{qh}_{\lambda\mathbf{k}}=-\gamma_{\lambda\mathbf{k}}\omega_{\lambda\mathbf{k}}\frac{\Delta\Omega}{\Omega}, \tag{2}$$

$$\Delta^{3}_{\lambda\mathbf{k}}=-\frac{T}{4M^3\omega_{\lambda\mathbf{k}}}\sum_{\mu\nu\mathbf{q}}\left|V^{\mathbf{k},\mathbf{q},\mathbf{k}+\mathbf{q}}_{\lambda\mu\nu}\right|^2\frac{1}{\omega_1^2\omega_2^2}\frac{(\omega_1^2-\omega_2^2)^2-\omega^2_{\lambda\mathbf{k}}(\omega_1^2+\omega_2^2)}{(\omega_1^2+\omega_2^2-\omega^2_{\lambda\mathbf{k}})^2-4\omega_1^2\omega_2^2}, \tag{3}$$

$$\Delta^{4}_{\lambda\mathbf{k}}=\frac{T}{4M^3\omega_{\lambda\mathbf{k}}}\sum_{\mu\mathbf{q}}W^{\mathbf{k},\mathbf{k},\mathbf{q},\mathbf{q}}_{\lambda\lambda\mu\mu}\frac{1}{\omega^2_{\mu\mathbf{q}}}, \tag{4}$$

$$\Gamma_{\lambda\mathbf{k}}=T\frac{\pi}{8M^3}\sum_{\mu\nu\mathbf{q}}\left|V^{\mathbf{k},\mathbf{q},\mathbf{k}+\mathbf{q}}_{\lambda\mu\nu}\right|^2\frac{1}{\omega_1^2\omega_2^2}[\,\delta(\omega_{\lambda\mathbf{k}}-\omega_1-\omega_2)+2\,\delta(\omega_{\lambda\mathbf{k}}+\omega_1-\omega_2)\,]. \tag{5}$$

Here λ, μ, and ν are the indices of the phonon branches, $\mathbf{k}$ and $\mathbf{q}$ are quasimomenta, $\omega_{\lambda\mathbf{k}}$, $\Delta_{\lambda\mathbf{k}}$, and $\Gamma_{\lambda\mathbf{k}}$ are, respectively, the initial phonon frequency and its shift and the phonon damping, $\hat{V}$ and $\hat{W}$ are the amplitudes of three- and four-phonon processes (see Ref. 4), $\gamma_{\lambda\mathbf{k}}=-\partial\ln\omega_{\lambda\mathbf{k}}/\partial\ln\Omega$ is the Grüneisen parameter, $\Delta\Omega$ is the change in the volume Ω per atom due to thermal expansion, and $1\equiv(\mu,\mathbf{q})$ and $2\equiv(\nu,\ \mathbf{k}+\mathbf{q})$.

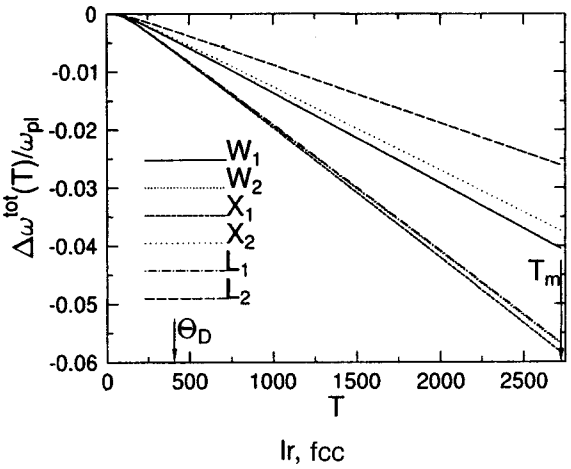

FIG. 1. Temperature dependence of the frequency shift in Ir at the symmetric points of the Brillouin zone; T_m — melting temperature, Θ_D — Debye temperature. The indices 1 and 2 denote longitudinal and transverse phonons; ω_{pl} — ion plasma frequency ($\omega_{pl}^{\mathrm{Ir}}=871$ K, see Ref. 8).

The basic computational results are presented in Figs. 1–5. It is evident from Figs. 1 and 2 that the high-temperature asymptotic representations (3)–(5) obtain very early (for $T \gtrsim \Theta_D/3$). Comparing the analogous results for bcc metals,[4] it can be concluded that this property is probably quite general. It follows from Figs. 1–4 that the strongest AEs in Ir occur for longitudinal phonons near the point X. Specifically, the decrease of the frequency and the increase of the damping with temperature are greatest for these phonons. The situation differs sharply in this respect from bcc alkali and alkaline-earth metals,[4,7] where the maximum damping obtains for ''soft'' phonons, for which the op-

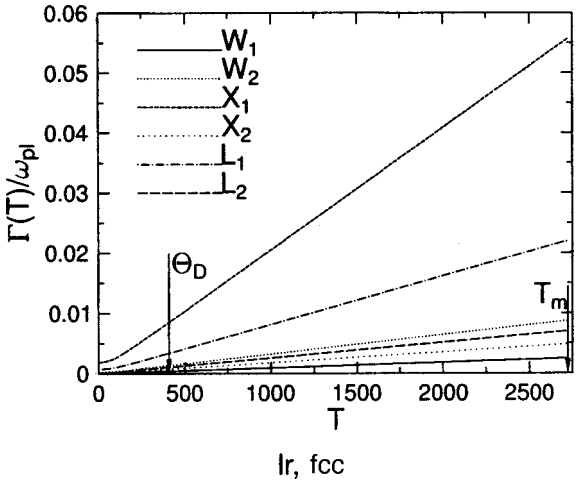

FIG. 2. Temperature dependence of phonon damping in Ir. All notations are the same as in Fig. 1.

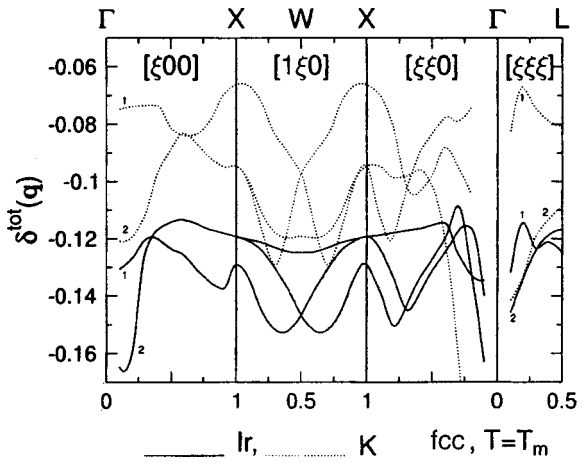

FIG. 3. Dispersion of the relative frequency shift $\delta=\Delta/\omega$ at $T=T_m$. Solid line — Ir, dotted line — fcc K. The numbers *1, 2* indicate longitudinal and transverse branches.

posite behavior of the frequency with increasing T is characteristic — hardening instead of softening. It is evident from Fig. 5 that this difference is due to the fact that in Ir three-phonon processes dominate over four-phonon processes.

To understand the role of the characteristic features of the interatomic interactions for the same lattice geometry, the computational results for a hypothetical fcc phase of K are presented in Figs. 3 and 4. The explicit domination of three-phonon over four-phonon processes, which causes the frequency shift to be negative over the entire Brillouin zone, is also seen in this case and is apparently characteristic for all metals with fcc structure. At the same time, the fact that the neighborhood of the point X is distinguished probably occurs only for crystals with a ''hard'' interatomic interaction potential of the type in Ir.

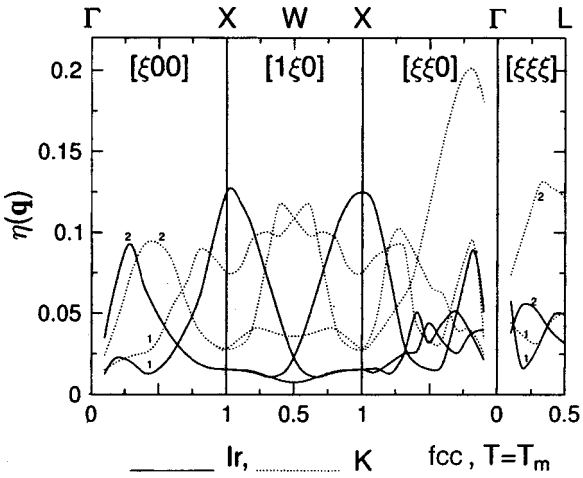

FIG. 4. Dispersion of the relative phonon damping $\eta=\Gamma/\omega$ at $T=T_m$. Solid line — Ir, dotted line — fcc K. The numbers *1, 2* indicate longitudinal and transverse branches.

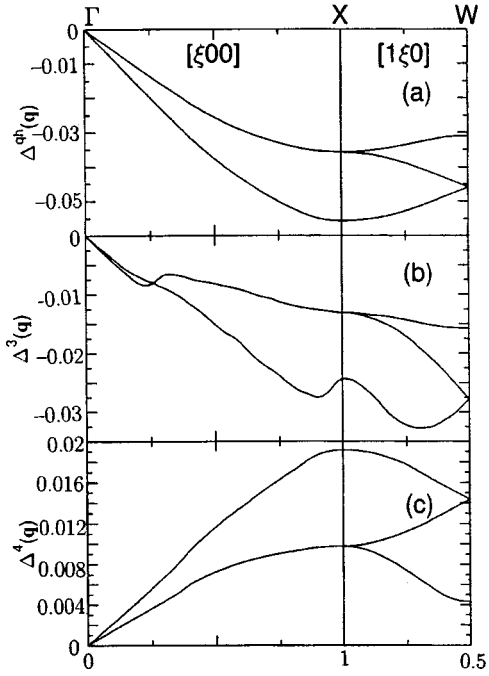

FIG. 5. Variation of the anharmonic contributions Δ^{qh} (a), Δ^3 (b), and Δ^4 (c) in the $\Gamma-X-W$ directions in Ir at $T=T_m$.

It is well known[8] that the ''hardness'' of the potential in metals increases with the effective valence Z ($Z=1$ for K and $Z=4.5$ for Ir). In any case Ir is a striking example of a crystal where AEs are maximum for high-frequency vibrations, in contrast to crystals with soft modes where the AEs are maximum for low-frequency phonons. The latter can be easily explained by the high powers of the frequency in the denominators of the Eqs. (3)–(5), but the example of Ir shows that in the general case the question cannot be solved on the basis of such simple considerations.

According to Fig. 4, an important feature of phonon damping is its nonmonotonic dependence on the wave vector in the $\Gamma-L$ and $\Gamma-X$ directions. According to the experimental data presented in Ref. 5, such nonmonotonic behavior is observed in Al, Cu, Ag, and Au. It can therefore be supposed that this behavior is typical for all metals with the fcc structure.

In closing we note that, as follows from Figs. 3–5, the AEs have a strong dependence over the Brillouin zone. For this reason, approximations which take them into account ''on average'' (approximations of the type used in the recently published Ref. 10), are dangerous. Finally, from the fact, found in the present work, that three-phonon processes predominate over four-phonon processes it follows that the well-known approaches such as the self-consistent phonon approach are inapplicable to metals with a close-packed structure.[11]

This work was supported by the Russian Fund for Fundamental Research, Project 98-02-16219.

[1] V. K. Vaks, *Introduction to the Microscopic Theory of Ferroelectrics* (Nauka, Moscow, 1973).
[2] V. G. Vaks, S. P. Kravchuk, and A. V. Trefilov, J. Phys. F **10**, 2325 (1980).
[3] M. I. Katsnel'son and A. V. Trefilov, Fiz. Met. Metalloved. **64**, 629 (1987).
[4] V. G. Vaks, S. P. Kravchuk, and A. V. Trefilov, J. Phys. F **10**, 2105 (1980).
[5] M. Zoli, G. Santoro, V. Bortolani *et al.*, Phys. Rev. B **41**, 7507 (1990).
[6] Y. Y. Ye, Y. Chen, K. M. Ho *et al.*, Phys. Rev. Lett. **58**, 1769 (1987); J. Phys.: Condens. Matter **3**, 9629 (1991).
[7] V. G. Vaks, G. D. Samolyuk, and F. V. Trefilov, Phys. Lett. A **127**, 37 (1988).
[8] A. S. Ivanov, M. I. Katsnelson, A. G. Mikhin *et al.*, Philos. Mag. B **69**, 1183 (1994).
[9] M. I. Katsnelson, I. I. Naumov, A. V. Trefilov *et al.*, Philos. Mag. B **75**, 389 (1997).
[10] R. C. Shukla and E. R. Cowley, Phys. Rev. B **58**, 2596 (1998).
[11] H. Böttger, *Principles of the Theory of Lattice Dynamics* (Physik-Verlag, Weinheim, 1983; Mir, Moscow, 1986).

Translated by M. E. Alferieff

Mechanism and kinetics of the reversible transformation *lda–hda* of amorphous ice under pressure

O. V. Stal'gorova, E. L. Gromnitskaya, V. V. Brazhkin, and A. G. Lyapin
Institute of High-Pressure Physics, Russian Academy of Sciences, 142092 Troitsk, Moscow Region, Russia

(Submitted 16 March 1999; resubmitted 30 March 1999)
Pis'ma Zh. Éksp. Teor. Fiz. **69**, No. 9, 653–658 (10 May 1999)

An ultrasonic investigation of pressure-induced direct and reverse transformations *lda–hda* between the amorphous phases of low- and high-density ice is performed and the change in the shear modulus is determined. It is found that elastic softening of the amorphous network precedes both transformations, and the behavior of *lda* phase is similar to that of hexagonal $1h$ ice before amorphization. At the same time a number of features of the *lda–hda* transformation are due to the topological disordering of the amorphous phases, and the kinetics of the transformation is different from the standard behavior at a first-order phase transition and also from the compression kinetics of ''classic'' glasses of the type *a*-SiO_2 and *a*-GeO_2. It is shown that the difference in the behavior of the *lda* and *hda* amorphous phases under pressure can be attributed to characteristic features of their spectra of low-energy two-level states. © *1999 American Institute of Physics.* [S0021-3640(99)00909-3]

PACS numbers: 64.70.Kb, 62.50.+p, 62.80.+f, 61.43.Er

Ice can exist at different pressures P and temperatures T in the form of various (at least 12) crystalline modifications.[1,2] Besides these modifications there exist amorphous phases of ice, a number of which commonly occur in nature.[3–5] In 1984 it was discovered[6] that an amorphous modification can be obtained by low-temperature ($T \approx 77$ K) compression of ordinary hexagonal ice $1h$. Besides the solid-phase amorphization (SPA) of ice, another remarkable phenomenon was discovered in Ref. 6. The amorphous modification *hda* (high-density amorphous) obtained on heating to 120–130 K under atmospheric pressure transformed into a less dense amorphous modification *lda* (low density amorphous) with a different structure of the short-range order. It was soon established that the *lda* phase obtained in this manner undergoes under compression a reversible transformation into the *hda* modification.[7]

The transitions $lda \rightarrow hda$ and $hda \rightarrow lda$ were accompanied by a jumplike change in volume, which made it possible to conclude that first-order transitions can occur between different amorphous phases.[7,8] At the same time a study of transformations in other amorphous substances, for example, glassy SiO_2 and GeO_2, showed that the transformation process in these glasses is extended in pressure[9–12] and exhibits unusual loga-

rithmic kinetics.[12] To this day ice apparently remains the only example of a material where sharp transformations into an amorphous state are observed. It has been suggested in a number of works that a transition between two amorphous phases of ice possesses a high-temperature continuation in the form of a first-order transformation in supercooled ice.[13–15] Despite the fact that so far only indirect evidence for the existence of such a transformation exists,[16] investigations in this field are arousing unusually great interest, since they make it possible to explain many unusual properties of water.[13–15]

The transformations $lda \leftrightarrow hda$, just as the SPA of ice, occur in the same temperature range where diffusion processes are largely frozen. Ultrasonic investigations have established that softening of the elastic constants of the crystal lattice of ice $1h$ precedes the SPA of ice; this is apparently directly related with the mechanism of SPA.[17,18] It can be inferred that transitions between amorphous phases are accompanied by softening of the elastic moduli, but in contrast to crystals such softening should occur at different pressures in different sections of the amorphous network.[11,12,19,20] This circumstance is evidently responsible for the logarithmic kinetics[12] and the wide pressure extent of transitions in *a*-SiO_2 and *a*-GeO_2.[9–12]

The study of transformations between the amorphous phases of ice is of special interest in this connection. A preliminary investigation of the direct transition $lda \leftrightarrow hda$ by the ultrasonic method was conducted in Ref. 21, but the results were qualitative, since later it was found that the *lda* ice samples investigated contained a large quantity ($\sim 50\%$) of crystalline phases. In the present work the mechanism and kinetics of the reversible transition $lda \leftrightarrow hda$ under pressure are investigated and the change in the shear modulus is determined. The data obtained show a definite analogy between the transformations $lda \rightarrow hda$ and $1h \rightarrow hda$. At the same time, features associated with the disordered nature of amorphous ice appear at the transition between the amorphous phases. It turns out that the characteristic behavior of the amorphous phases *hda* and *lda* can be interpreted on the basis of recent measurements of the density of low-energy two-level states (TLSs) in the ice phases studied.[22]

The measurements were performed by the pulsed ultrasonic method at pressures from 0 to 2 GPa in the temperature range 77–300 K on a cylinder–piston type high-pressure setup, described in detail in Ref. 23. Cylindrical samples, 8–10 mm high and ~ 17 mm in diameter, were prepared from ice obtained by rapidly cooling distilled water. The experimental details are described in detail in Refs. 17 and 18. The error in determining the pressure did not exceed 0.02 GPa. For measurements above 77 K under thermostatic control the temperature gradient on the sample and the accuracy of the temperature determination were estimated to be 1–2 K.

The *lda* phase was synthesized on the basis of detailed information on the transformations $1h \rightarrow hda$ and $hda \rightarrow lda$, which were obtained in Refs. 6–8, as well as from ultrasonic investigations performed on the present setup[17,18] with continuous monitoring of the P–V–T parameters of the phase transformations of ice. The *hda* phase was obtained first by compressing $1h$ ice to 1.7 GPa at $T = 110$ K. After decompression to 0.05 GPa and heating to $T = 138$ K, a sample consisting primarily of the *lda* phase with density ≈ 0.96 g/cm^3 was synthesized. According to published data,[7] the density of *lda* ice is 0.94 g/cm^3 at liquid-nitrogen temperature. The somewhat higher density of the sample in our case is apparently due to the presence of a small quantity of the *hda* phase or other microcrystalline inclusions. We note that the *lda* phase is difficult to obtain

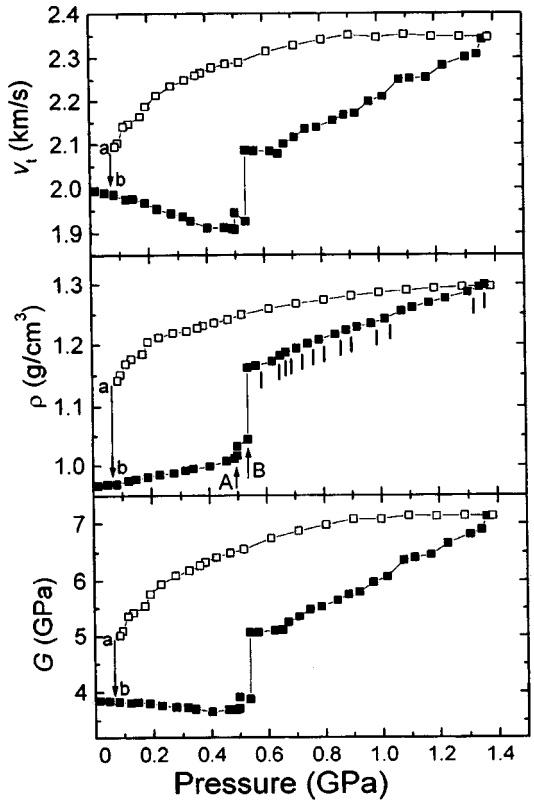

FIG. 1. Variation of the density ρ, transverse ultrasonic velocity v_t, and shear modulus G versus pressure at $T=110$ K for the direct and reverse transition *lda*→ *hda*. The section ab of the reverse transition corresponds to temperatures 120–130 K. The points where the pressure was held constant for a short time are marked by vertical bars on the curve $\rho(P)$.

because of the smallness of the P,T region where it can be produced.

Figure 1 shows the pressure dependences of the transverse velocity v_t of ultrasound and the density ρ as well as the dependence of the shear modulus calculated in the uniform medium approximation $G(P)=\rho v_t^2$, for the direct and reverse transformations lda–hda. The measurements were performed at temperature 110 K. It was found that as pressure increases, the transverse velocity and shear modulus of the *lda* phase decrease right up to pressure 0.4 GPa. According to published data,[7,8] a sharp transition occurs in this region to the higher density phase *hda*. We held the pressure constant at the points *A* ($P=0.50$ GPa) and *B* ($P=0.53$ GPa), marked in Fig. 1, for 9 and 20 min, respectively. The large irreversible increase in density and transverse velocity at these points attests to an lda–hda transition. The subsequent pressure increase leads to an additional increase of ρ and v_t. The pressure was held constant for 1–2 min at a number of points (Fig. 1). In this case relaxation of the density and transverse velocity of ultrasound as a function of time were observed right up to the maximum pressure ≈ 1.4 GPa. The typical change for ρ was 0.2–1.0% of the jump at the lda–hda transition and 0.3–2% for v_t. On the one hand this exceeds the measurement error, while on the other similar relaxation changes

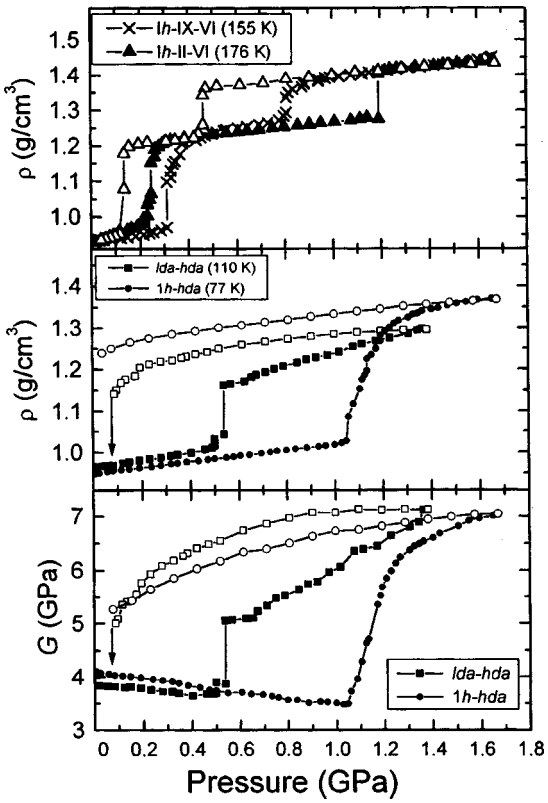

FIG. 2. Comparison of the pressure dependences $\rho(P)$ and $G(P)$ for the transitions $lda \rightarrow hda$ and $1h \rightarrow hda$. The curves $\rho(P)$ for certain transitions between crystalline phases are also presented. The open symbols correspond to decompression.

are not observed in transitions between the crystal phases of ice and cannot be attributed to the error of the measurement method. Therefore the transformation $lda \rightarrow hda$ continues at least to pressure 1.4 GPa, as is confirmed by comparing the direct and reverse paths in Fig. 1.

There is an obvious analogy between the transformations $lda \rightarrow hda$ and $1h \rightarrow hda$ (Fig. 2), since in both cases softening of the shear modulus precedes a transition into the higher-density phase. Moreover, the pressure derivatives of the shear modulus for the *lda* phase ($G'_p \sim -(0.3–0.6)$) and the $1h$ phase ($G'_p \sim -(0.4–0.6)$) are quite close. However, there are also appreciable differences between these transformations. The transition $lda \rightarrow hda$ is clearly more extended in pressure. This transformation apparently is completed at a pressure somewhat above 1.4 GPa, since the final value of the density at 1.4 GPa is somewhat lower than the density of the *hda* phase. It should be underscored that the sharp jump in properties for the transition $lda \rightarrow hda$ is due to long-time holding (for a total of about 30 min), while the collapse of the hexagonal $1h$ ice into the *hda* phase is more rapid, and the transformation does not have an extended ''tail.'' At the same time, a relatively rapid change in pressure also leads to sharp collapse of the *lda* phase but at a somewhat higher pressure.[7,8] The extended nature of the $lda \rightarrow hda$

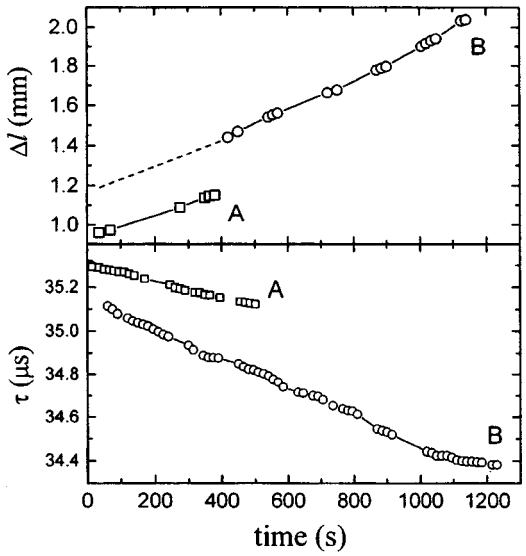

FIG. 3. Time dependence of the piston displacement Δl, related linearly with the sample volume, and the travel time τ of an ultrasonic pulse at pressures marked by the arrows *A* and *B* in Fig. 1.

transformation has also been observed in previous measurements of the density.[7] For comparison, experimental curves for first-order phase transitions between the crystalline phases I $\rightarrow$ II $\rightarrow$ VI and I $\rightarrow$ IX $\rightarrow$VI are also presented in Fig. 2.

The mechanism of the reverse transformation $hda \rightarrow lda$, just as that of the direct transition, is apparently due to the elastic softening of the amorphous network of the *hda* phase. This follows from a comparison of the character of the variations in $G(P)$ for the reverse transition with a sharper jump in the density dependence (Fig. 1). The elastic softening preceding the jump in volume is even more noticeable when the transformation $hda-lda$ occurs with a change in temperature.[18]

Definite information about the transformation mechanism can be obtained by investigating the transformation kinetics. In our case such measurements were performed under pressures corresponding to the points *A* and *B*. The results are presented in Fig. 3. We observed an almost linear time dependence for the change in density and the travel time of an ultrasonic pulse. Such behavior evidently does not correspond to the exponential kinetics of ordinary first-order phase transitions, which is described by the activation energies for nucleation and growth of crystals, or to the logarithmic compression kinetics for *a*-SiO_2 and *a*-GeO_2,[12] which is due to the wide spectrum of activation energies for local structural rearrangements.

In summary, it can be concluded that for the transformation $lda \rightarrow hda$ features characteristic of first-order phase transitions (jump in volume, elastic moduli, and so on) and SPA $1h \rightarrow hda$ (softening of *G* right up to the transition itself) on the one hand and typical features for amorphous phase–amorphous phase transformations in *a*-SiO_2 and *a*-GeO_2 (wide pressure range for the transition and relaxational changes) on the other are observed. The characteristic features of the transformation $lda \rightarrow hda$ can be explained on the basis of recent measurements of the density of TLSs in the phases of ice.[22]

The mechanism of SPA (including the transition $1h \rightarrow hda$) is associated, as a rule, with instability of the initial crystal lattice,[24,25] and the instability, being associated with definite phonon modes, should appear coherently in the entire crystal. For an amorphous network the variations in the energy states of individual atoms and local atomic stresses lead to variations in the pressures for structural rearrangement of different nanosections of the network, and the transformation into the amorphous phase is controlled by local soft modes. Volume changes should appear at a definite concentration of soft modes that corresponds to instability of the amorphous network. We assume that the density of low-energy TLSs in the amorphous phase is related with the phonon density of states, determining the instability of local sections of the amorphous network under pressure, both characteristics probably being determined by the topological stiffness of the system. The behavior of the topologically stiff disordered networks should be similar to that of the crystal lattices with the same short-range order, while in soft glasses the transformation will proceed in a wider range of the external parameters.

Measurements of the low-temperature infrared absorption spectra established that the *lda* phase, just as the $1h$ modification, possesses an almost zero density of low-energy excitations, in contrast to the *hda* phase and conventional glasses (including *a*-SiO_2 and *a*-GeO_2).[22] That is, the *lda* phase should behave similarly to $1h$ ice, as a topologically stiff network, as is in fact observed experimentally. The negative derivative of the shear modulus is probably a quite general property of tetrahedrally packed structures.[25] However, in the presence of instability of the ordered lattice the rearrangement of the short-range order should encompass the entire crystal, whereas in the amorphous network of *lda* a substantial number of atoms and nanosections is apparently resistant to a change in short-range order at the onset of the transition. The transformation of such nanosections will occur at higher pressures.

In summary, features appear in the transformation of amorphous ice that are general for disordered systems and are due to the variations in the atomic characteristics. The behavior of the *hda* phase before a transformation is similar to that of the ''classic'' glasses SiO_2 and GeO_2. At the same time the behavior of ice before a $lda \rightarrow hda$ transition can be explained by specific features of the structure and phonon spectrum of the *lda* phase. More complete information about the mechanism of amorphous phase–amorphous phase transformations can be obtained from a detailed comparison of the transitions kinetics for amorphous ice and *a*-SiO_2 and *a*-GeO_2 glasses. Analysis of the behavior of ice in a $hda \rightarrow lda$ transition and the corresponding kinetic measurements are also very important for resolving this problem.

This work was supported by the Russian Fund for Fundamental Research (Grant 98-02-16325) and the Educational-Science Center ''Matter Under High Static Compression'' (Project No. 250).

[1] E. Yu. Tonkov, *High Pressure Phase Transformations*, A Handbook 1-2 (Gordon and Breach, Philadelphia, 1992).
[2] C. Lobban, J. L. Finney, and W. F. Kuhs, Nature (London) **391**, 268 (1998).
[3] A. G. G. M. Tielens and L. J. Allamandola, *Physical Processes in Interstellar Clouds*, edited by G. E. Morfill and M. Scholer (Dordrecht, Reidel, 1987), p. 333.
[4] M. J. Mumma, P. R. Weissman, and S. A. Stern, *Protostars and Planets III*, edited by E. H. Levy, J. I. Lunine, and M. S. Matthews (University of Arizona Press, Tucson, 1993), p. 1177.
[5] P. Jenniskens, D. F. Blake, M. A. Wilson, and A. Pohorille, Astrophys. J. **455**, 389 (1995).
[6] O. Mishima, L. D. Calvert, and E. Whalley, Nature (London) **310**, 393 (1984).

[7] O. Mishima, L. D. Calvert, and E. Whalley, Nature (London) **314**, 76 (1985).
[8] O. Mishima, J. Chem. Phys. **100**, 5910 (1994).
[9] C. Meade, R. J. Hamley, and H. K. Mao, Phys. Rev. Lett. **69**, 1387 (1992).
[10] C. S. Zha, R. J. Hemley, H. K. Mao *et al.*, Phys. Rev. B **50**, 13105 (1994).
[11] K. H. Smith, E. Shero, A. Chizmeshya, and G. H. Wolf, J. Chem. Phys. **102**, 6851 (1995).
[12] O. B. Tsiok, V. V. Brazhkin, A. G. Lyapin, and L. G. Khvostantsev, Phys. Rev. Lett. **80**, 999 (1998).
[13] P. H. Poole, F. Sciortino, U. Essmann, and H. E. Stanley, Nature (London) **360**, 324 (1992).
[14] E. G. Ponyatovskiĭ, V. V. Sinitsyn, and T. A. Pozdnyakova, JETP Lett. **60**, 360 (1994).
[15] H. Tanaka, Nature (London) **380**, 328 (1996).
[16] O. Mishima and H. E. Stanley, Nature (London) **392**, 164 (1998).
[17] O. V. Stal'gorova, E. L. Gromnitskaya, and V. V. Brazhkin, JETP Lett. **62**, 356 (1997).
[18] E. L. Gromnitskaya, O. V. Stal'gorova, and V. V. Brazhkin, Zh. Éksp. Teor. Fiz. **112**, 200 (1997) [JETP **85**, 109 (1997)].
[19] V. V. Brazhkin, A. G. Lyapin, and O. B. Tsiok, Rev. High Pressure Sci. Technol. **7**, 347 (1998).
[20] D. J. Lacks, Phys. Rev. Lett. **80**, 5385 (1998).
[21] V. V. Brazhkin, E. L. Gromnitskaya, O. V. Stalgorova, and A. G. Lyapin, Rev. High Pressure Sci. Technol. **7**, 1129 (1998).
[22] N. I. Agladze and A. J. Sievers, Phys. Rev. Lett. **80**, 4209 (1998).
[23] O. V. Stal'gorova, E. L. Gromnitskaya, D. R. Dmitriev, and F. F. Voronov, Prib. Tekh. Éksp. **39**, 115 (1996).
[24] V. V. Brazhkin and A. G. Lyapin, High Press. Res. **15**, 9 (1996).
[25] A. G. Lyapin and V. V. Brazhkin, Phys. Rev. B **54**, 12036 (1996).

Translated by M. E. Alferieff

Effect of phasons and magnetic fields on the electronic spectrum of a three-dimensional quasicrystal

Yu. Kh. Vekilov,* P. V. Slobodyanyuk, É. I. Isaev, and S. F. Arslanov
Moscow State Institute of Steels and Alloys, 117936 Moscow, Russia

(Submitted 31 March 1999)
Pis'ma Zh. Éksp. Teor. Fiz. **69**, No. 9, 659–661 (10 May 1999)

The effect of phasons and magnetic fields on the electronic spectrum of an icosahedral quasicrystal is investigated in the tight-binding approximation. Phasons smooth the singular spectrum and produce a greater delocalization of the critical wave functions. A magnetic field shifts the limits of the spectrum, smooths the spectrum, lifts the degeneracy, and also delocalizes the wave functions. © *1999 American Institute of Physics.* [S0021-3640(99)01009-9]

PACS numbers: 71.23.Ft

Measurements of the conductivity of pure, perfect AlPdRe quasicrystals have shown that a mobility threshold exists and that the Mott law $\sigma=\sigma_0/\exp(-T^*/T)^{1/4}$ holds at low temperatures.[1,2] This shows that in an ''ideal'' perfect quasicrystal the electronic states at the Fermi level are localized in the Fermi-glass regime (the density of states at the Fermi level is nonzero and the Fermi level lies below the mobility threshold). This localization differs from the Anderson localization, which is due to the disorder in the system, and it is caused by interference of electronic states as a result of the symmetry characteristics and structure of the quasicrystal.[3] Theoretical analysis of the electronic spectra indicates that such localization possesses characteristic features. In a one-dimensional quasicrystal (Fibonacci chain) the density of states is highly singular (a Cantor set of gaps) and the measure of the allowed states (Lebesgue measure) is zero.[4,5] In two-dimensional (Penrose tiling)[6] and three-dimensional (Amman–MacKay network)[7] quasicrystals the spectrum is also singular, but it does not contain a hierarchical gap structure (nonzero Lebesgue measure). The wave functions are ''critical,'' i.e., they are not localized, they are not delocalized, and they decay with increasing distance according to a power law. In contrast to the one- and two-dimensional cases, for the three-dimensional crystals the exponent — the localization exponent — is the same for all states. For Anderson localization, which is due to incoherent scattering by the disorder introduced into the system, the electronic states are localized, their spectrum is continuous, and the localization is stable against small perturbations (the mobility threshold shifts continuously with the external perturbation). In contrast to Anderson localization, the localization of electronic states in a quasicrystal should be unstable with respect to small perturbations that destroy the symmetry of the system. This arises the interesting problem of investigating the effect of intrinsic defects (phasons) and external fields (magnetic fields) on the electronic spectrum of a quasicrystal. It is also of interest to compare the ''competing'' effect of Anderson localization (the effect of strong substitutional disorder in a quasicrystalline alloy has

been investigated in Ref. 7). In this letter we present the basic results of an investigation of the effect of phason distortions and magnetic fields on the electronic spectrum of a three-dimensional icosahedral quasicrystal.

Just as in Ref. 7, the electronic spectrum and wave functions of an icosahedral quasicrystals were investigated in the tight-binding approximation and by the method of level statistics on the basis of a two-fragment structural model (Amman–MacKay network). The quasicrystal was treated as the structural limit of rational approximants with increasing period (the computational method and the method for constructing the structure using a projection technique are described in detail in Ref. 7). The ''centered'' decoration of approximants — atoms with one *s* orbital per atom — was considered. The atoms were placed at the centers of the rhombohedra. The Hamiltonian of the system has the form

$$H=\sum_i |i\rangle \epsilon_i \langle i| + \sum_{j,j\neq i} |i\rangle t_{ij} \langle j|.$$

When only atoms of one kind are present in the system, the diagonal elements E_i can be set equal to zero, and the hopping integrals can be assumed to be a nonzero constant only for the nearest neighbors ($t_{ij}=-1$) — for atoms belonging to rhombohedra that have a face in common.

Phasons were introduced as follows. For a centered decoration of the rhombohedra a configuration consisting of two ''blunt'' and two ''sharp'' rhombohedra is often encountered. In a certain combination these rhombohedra form a rhombic dodecahedron. Phasons are introduced by flipping the rhombohedra comprising the rhombic dodecahedron. The rhombohedra were flipped in such a way that the surface of the rhombic dodecahedron remained unchanged and the spatial orientation of the flipped rhombohedra was preserved. For such flips the atoms at the centers of the rhombohedra were transferred into positions which are symmetric relative to the geometric center of the rhombododecahedron (the number of nearest neighbors remained the same). The analog of such a transformation in the projection technique is a fluctuation of the projection tube. The ratio of the number of ''sharp'' rhombohedra to the number of ''blunt'' rhombohedra remains unchanged, and the average slope of the projection tube does not change and correspondingly the volume of the projection of the projection tube on the unphysical subspace is constant. When phasons were introduced, the coordination environment changed for atoms at the centers of the rhombohedra, as a result of which the positions of the nonzero matrix elements of the Hamiltonian changed. A magnetic field was introduced in the standard manner by multiplying the matrix elements of the Hamiltonian matrix by a phase factor containing the vector potential in the Landau gauge. The magnitude of the field was measured by the ratio of the magnetic flux through a cell to the flux quantum.

The calculations were performed for the approximant 2/1, 3/2. A number of characteristics, including the integrated density of states, the density of states, the Lebesgue measure of the spectrum, the coordinate dependence of the wave functions, and the localization exponents were calculated. In the present letter, we present information only about the density of states and the localization of the wave functions.

The computational results show that when phasons are introduced the spectrum (see

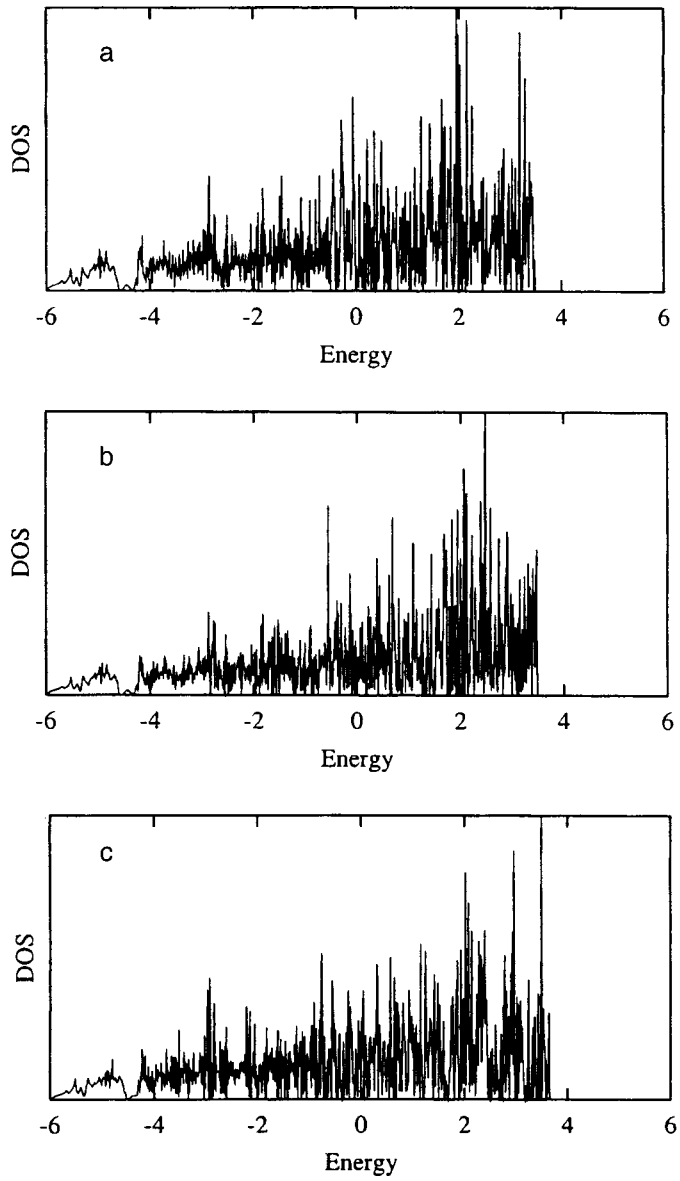

FIG. 1. Density of states for 3/2 approximants: a) no phason; b) 5 flips per cell; c) 74 flips per cell.

Fig. 1) becomes less singular and the wave functions more delocalized (less ''critical''). The effect of a magnetic field on the spectrum of a quasicrystal is more complicated. This will be discussed in detail in a separate paper. Here we give only a qualitative discussion of the results. A magnetic field lifts the degeneracy of the electronic levels, smears the spectrum, and shifts (quasiperiodically as a function of the field strength) the limits of the spectrum. In contrast to ordinary crystal and amorphous structures, the wave functions become more delocalized when a magnetic field is switched on.

It is interesting to compare the results presented above with the effect of ''chemical'' disorder (substitutional disorder) on the spectrum. In Ref. 7 it was established that for a high degree of substitutional disorder, $\delta=\epsilon_A-\epsilon_B$ ($\epsilon_i=\epsilon_A, \epsilon_B$), the energy spectrum is substantially smoothed compared with a quasicrystal without disorder, and the wave functions tend to localize. Here it is shown that for $\delta<0.1$ (i.e., evidently, below the Anderson localization threshold) the wave functions become more delocalized compared with the wave functions in a perfect quasicrystal.

In summary, it can be considered as proven that the electronic states at the Fermi level are localized by virtue of coherent interference due to the characteristic features of the symmetry and structure of the quasicrystal. Small disturbances — phasons, a magnetic field, weak chemical disorder — destroy this interference and take the quasicrystal out of the Fermi-glass regime. Correspondingly, the transport properties and their temperature characteristics will be different from those of a perfect ideal object.

In closing we thank D. V. Olenev for his attention to this work and for valuable remarks.

*e-mail: vekilov@trf.misa.ac.ru

[1] C. R. Wang, H. S. Kuan, S. T. Lin, and Y. Y Chen, J. Phys. Soc. Jpn. **67**, 2383 (1998).
[2] Q. Guo and S. J. Poon, Phys. Rev. B **54**, 12793 (1996).
[3] Yu. Kh. Vekilov, P. A. Korzhavyĭ, and D. V. Olenev, JETP Lett. **62**, 372 (1995).
[4] P. A. Kalugin, A. Yu. Kitaev, and L. S. Levitov, JETP Lett. **41**, 145 (1985).
[5] P. A. Kalugin, A. Yu. Kitaev, and L. S. Levitov, Zh. Éksp. Teor. Fiz. **91**, 692 (1986) [Sov. Phys. JETP **64**, 410 (1986)].
[6] H. Tsunetsugu, T. Fujiwara, K. Ueda, and T. Tokiḥiro, Phys. Rev. B **43**, 8879 (1991).
[7] D. V. Olenev, É. Isaev, and Yu. Kh. Vekilov, Zh. Éksp. Teor. Fiz. **113**, 1009 (1998) [JETP **86**, 550 (1998)].

Translated by M. E. Alferieff

Simulation of a Panlevé–Gullstrand black hole in a thin ^{3}He-A film

G. E. Volovik

Low Temperature Laboratory, Helsinki University of Technology, FIN-02015 HUT, Finland;
L. D. Landau Institute of Theoretical Physics, Russian Academy of Sciences, 117940 Moscow, Russia

(Submitted 1 April 1999)
Pis'ma Zh. Éksp. Teor. Fiz. **69**, No. 9, 662–668 (10 May 1999)

A quasi-stationary superfluid state is constructed which exhibits an event horizon and Hawking radiation. © *1999 American Institute of Physics.* [S0021-3640(99)01109-3]

PACS numbers: 67.57.De, 04.70.Dy

Introduction

It is well known that the gravitational field can be simulated in condensed matter by motion of a liquid: the propagation of some perturbations in a moving liquid obeys the same equation as the propagation of relativistic particles in the gravitational field. These perturbations are sound waves in normal fluids[1,2] and quasiparticles in superfluids[3] (phonons in superfluid ^{4}He and low-energy Bogoliubov fermions in superfluid ^{3}He-A). If the fluid motion is radial and spherically symmetric, the effective metric is expressed in terms of the radial velocity $v(r)$ as

$$ds^2 = -(c^2 - v^2(r))dt^2 + 2v(r)drdt + dr^2 + r^2 d\Omega^2. \quad (1)$$

For superfluids v is the velocity of the superfluid vacuum, v_s.

The kinetic energy of superflow plays the part of the gravitational potential: $\Phi = -v^2(r)/2$. If one chooses the velocity field corresponding to the potential of a point body of mass M:

$$v^2(r) = -2\Phi = 2GM/r \equiv c^2 r_h/r, \quad (2)$$

one obtains the Panlevé–Gullstrand form of the Schwarzschild geometry (see e.g., Ref. 2). Here r_h denotes the position of the event horizon, where the velocity of the fluid reaches the ''speed of light'' (c is the speed of sound for phonons or the slope of the energy spectrum $E = \pm cp$ of Bogoliubov fermions). If the fluid moves towards the origin, i.e., $v(r) < 0$, this velocity field reproduces the horizon of a black hole (the so-called sonic black hole[1]): Since the velocity of the fluid behind the horizon exceeds the propagation velocity c of the perturbations with respect to the fluid, the low-energy quasiparticles are trapped within the horizon. In quantum Fermi liquids— superfluid phases of ^{3}He — this kind of hydrodynamic black hole will allow one to investigate the quantum fermionic vacuum in a classical gravitational field in the presence of a horizon.

The hydrodynamic black hole was first suggested by Unruh for an ordinary liquid.[1] However, since all the known normal liquids are classical, the most interesting quantum effects related to the horizon cannot be simulated in such a flow. Also, the geometry is such that it cannot be realized: in the inward radial flow the liquid accumulates at the origin, so that this sonic black hole cannot be stationary. In the other scenario a horizon appears in soliton motion if the velocity of the soliton exceeds the local ''speed of light.''[1] This scenario has the same drawback: in a finite system the motion of the soliton cannot be supported for a long time. In the ''draining bathtub'' geometry suggested in Ref. 4 the fluid motion can be made constant in time. However, the friction of the liquid moving through the drain is the main source of dissipation. This will hide any quantum effects related to the horizon. Superfluidity of the liquid does not help much in this situation. A horizon does not appear: The ''superluminal'' (supercritical) motion with respect to the boundaries is unstable, because the interaction with the walls produces the Cherenkov radiation of quasiparticles, and the superfluidity collapses (see Ref. 5).

Here we suggest a scenario in which this collapse is avoided. The superfluid motion becomes quasi-stationary and exhibits an event horizon; the lifetime of the ''superluminally'' flowing state is determined by intrinsic mechanisms related to the existence of a horizon: in particular, by the analog of Hawking radiation.

Simulation of 2D black hole

A stationary black hole can be realized in the following geometry, which is a refinement of the bathtub geometry of Ref. 4 (see Fig. 1a). A superfluid ^{3}He-A film is moving towards the center of the disk (i.e., $v(r)<0$), where it escapes to the third dimension through an orifice (hole). If the thickness of the film is constant, the flow velocity of the 2D motion increases towards the center as $v(r)=a/r$, and at $r=r_h=a/c$ it reaches the''speed of light'' c (now r denotes the radial coordinate in the cylindrical system). If this happens, the hole becomes a black hole: Behind the horizon, at $r<r_h$, the (quasi)particles can move only to the hole (orifice), since their velocity of propagation with respect to the superfluid condensate is less than the velocity v of the condensate.

The black hole analogy is also supported by the effective metric experienced by the quasiparticles. The energy spectrum of the low-energy Bogoliubov fermions is given by

$$(E-\mathbf{p}\cdot\mathbf{v})^2=c^2(p_x^2+p_y^2)+v_F^2(p_z\mp p_F)^2. \tag{3}$$

Here the axis z is along the normal of the film. This axis z also marks the direction of the unit orbital vector $\hat{l}$, which is the anisotropy axis for the ''speed of light'': $\hat{l}$ is fixed along the normal to the film. The ''speed of light'' for quasiparticles propagating along the film is $c\sim 3$ cm/sec. It is much smaller than the Fermi velocity v_F, which corresponds to the ''speed of light'' for quasiparticles propagating along the normal to the film. This c is also much smaller than the speed of sound in ^{3}He-A, and for that reason the motion of fluid has no effect on the density of the liquid.

Outside the orifice the velocity of the superfluid $\mathbf{v}$ is two-dimensional and radial. For such a velocity field the energy spectrum in Eq. (3) corresponds to the motion of a Bogoliubov quasiparticle in a space with the following effective metric:

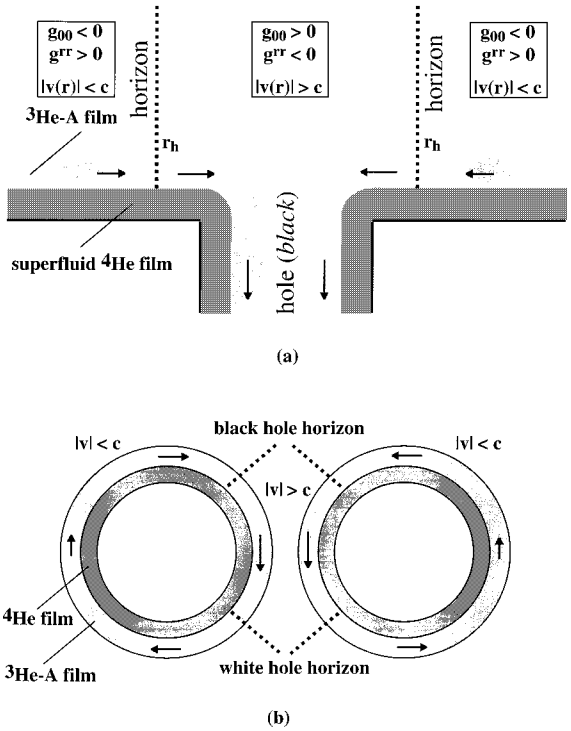

FIG. 1. Simulation of a 2D black hole in a thin ^{3}He-A film. a: ''Draining bathtub'' geometry. b: ^{3}He-A film circulating on the top of a ^{4}He film on a torus.

$$ds^2 = -(c^2 - v^2(r))dt^2 + 2v(r)drdt + dr^2 + r^2 d\phi^2 + \frac{c^2}{v_F^2} dz^2. \tag{4}$$

Across the horizon the g_{00} component of the metric changes sign, which marks the presence of the horizon at $r = r_h$, where $v(r_h) = c$.

The important element of the construction in Fig. 1a is that the moving superfluid ^{3}He-A film is placed on the top of the superfluid ^{4}He film. This is done to avoid the interaction of the ^{3}He-A film with the solid substrate. The superfluid ^{4}He film effectively screens the interaction and thus prevents the collapse of the ''superluminal'' flow of ^{3}He-A.

The motion of the superfluid ^{3}He-A with respect to superfluid ^{4}He film is not dangerous. The superfluid ^{4}He is not excited even if ^{3}He-A moves with its superluminal velocity: the value of c for ^{3}He-A is much smaller than the Landau velocity for radiation of quasiparticles in superfluid ^{4}He, which is about 50 m/sec. In this analysis we have neglected the radiation of surface waves, assuming that the thickness of ^{4}He film is small enough.

Finally one can close the superflow by introducing a toroidal geometry. Figure 1b shows the superflow around meridians (minor circles) of the torus in the cross-sectional plane. Both superfluid condensates, ^{4}He and ^{3}He-A, circulate around meridians with

integer numbers N_4 and N_3 of superfluid velocity circulation quanta, $\kappa_4 = 2\pi\hbar/m_4$ and $\kappa_3 = \pi\hbar/m_3$. If the inner radius of the torus is small, the superfluid velocity is enhanced in the region close to the inner circle, where it can exceed c. In this case both a black hole horizon and a white hole horizon appear.

Since the extrinsic mechanism of friction of the ^{3}He-A film — the scattering of quasiparticles on the roughness of substrate — is eliminated, we can now consider intrinsic mechanisms of dissipation of the supercritical flow. The most interesting one is the Hawking radiation related to the existence of a horizon.

Vacuum in comoving and rest frames

Let us consider the simplest case of the 2D motion along the film in the bathtub geometry of Fig. 1a. This can be easily generalized to the motion in the toroidal geometry.

There are two important reference frames: (i) The frame of the observer, who is locally comoving with the superfluid vacuum. In this frame the local superfluid velocity is zero, $v = 0$, so that the energy spectrum of the Bogoliubov fermions as viewed by the observer is (here we assume a pure 2D motion along the film)

$$E_{\rm com} = \pm cp. \tag{5}$$

In this geometry, in which the superflow velocity is confined in the plane of the film, the speed c coincides with the Landau critical velocity of the superfluid vacuum, $v_{\rm Landau} = \min(|E_{\rm com}(p)|/p)$. The vacuum as determined by the comoving observer is shown on Fig. 2a: fermions occupy the negative energy levels in the Dirac sea (the states with the minus sign in Eq. (5)). It is the counterpart of the Minkowski vacuum but is defined only locally: The comoving frame cannot be defined globally. Moreover for the comoving observer, whose velocity changes with time, the whole velocity field $\mathbf{v}(\mathbf{r},t)$ of the superflow is time dependent. This does not allow a correct determination of the energy.

(ii) The energy can be well defined in the laboratory frame (the rest frame). In this frame the system is stationary, though is not static: The effective metric does not depend on time, so that the energy is conserved, but this metric contains the mixed component g_{0i}. The energy in the rest frame is obtained from the local energy in the comoving frame by means of a Doppler shift. In case of the radial superflow one has

$$E_{\rm rest} = \pm cp + p_r v(r). \tag{6}$$

Figures 2b,c show how the ''Minkowski'' vacuum of the comoving frame is seen by the observer at rest (note that the velocity is negative, $v(r) < 0$). In the absence of a horizon, or outside the horizon, the local vacuum does not change: the states which are occupied (empty) in the Minkowski vacuum remain occupied (empty) in the rest-frame vacuum (see Fig. 2b). In the presence of a horizon behind which the velocity of superflow exceeds the Landau critical velocity, the situation changes: Behind the horizon the vacuum in the rest frame differs from that in the comoving frame. Let us for simplicity consider the states with zero transverse momentum $p_\phi = 0$ on the branch $E_{\rm rest} = (v(r) + c)p_r$ in the rest frame. If the system is in the Minkowski vacuum state (i.e., in the ground state as viewed by the comoving observer), the quasiparticles on this branch have an inverted distribution in the rest frame: the negative energy states are empty, while the

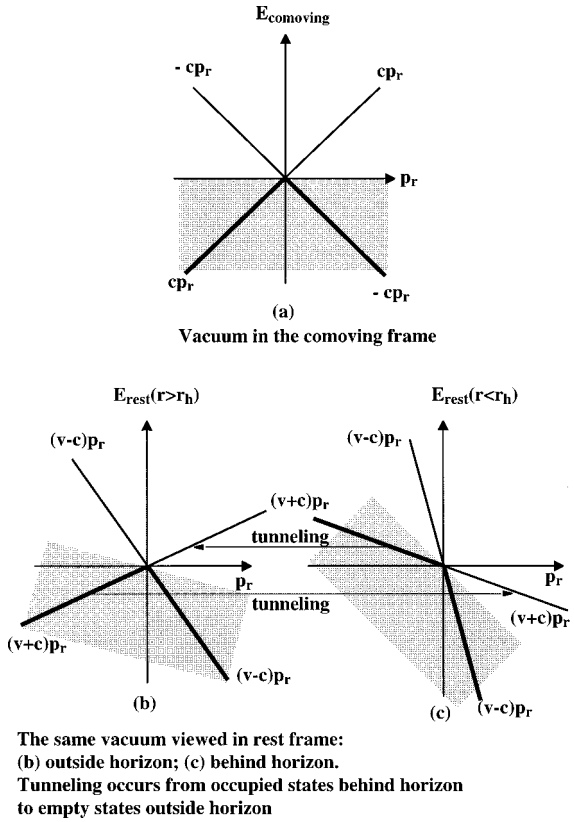

FIG. 2. a: Fermionic vacuum in the comoving frame. The states with $E_{\rm com}<0$ are occupied (thick lines). The same vacuum viewed in the rest frame (b) outside horizon and (c) inside horizon. Behind the horizon the branch $E_{\rm rest}=(v+c)p_r$ (for $p_\perp=0$) has an inverted population as seen in the rest frame: the states with positive energy $E_{\rm rest}>0$ are filled, while the states with $E_{\rm rest}<0$ are empty. The tunneling across horizon from the occupied states to the empty states with the same energy gives rise to the Hawking radiation from the horizon.

positive energy states are occupied (see Fig. 2c). For this branch the particle distribution corresponds to the negative temperature $T=-0$ behind the horizon.

Since the energy in the rest frame is a good quantum number, the fermions can tunnel across the horizon from the occupied levels to empty ones with the same energy. Thus if the system is initially in the Minkowski vacuum in the comoving frame, the tunneling disturbs this vacuum state: Pairs of excitations are created: a quasiparticle, say, is created outside the horizon while its partner — a quasihole — is created inside the horizon. This simulates the Hawking radiation from the black hole.

Hawking radiation

To estimate the tunneling rate in the semiclassical approximation, let us consider the classical trajectories $p_r(r)$ of particles, say, with positive energy, $E_{\rm rest}>0$, for the simplest case when the transverse momentum p_ϕ is zero (Fig. 3). The branch $E_{\rm rest}=(v(r)-c)p_r$ describes the incoming particles with $p_r<0$ which propagate through the horizon

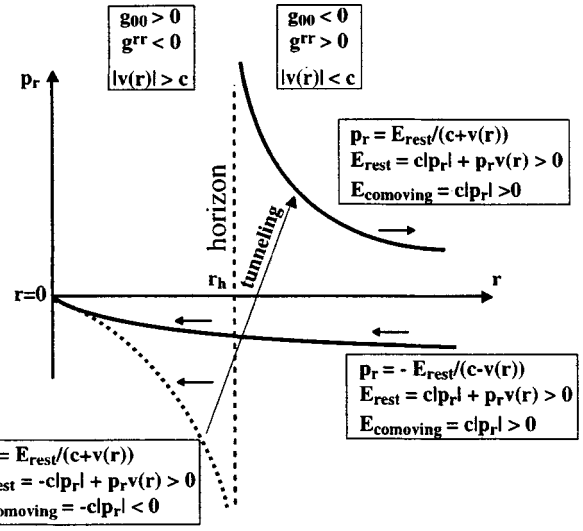

FIG. 3. Tunneling from the Minkowski vacuum within the horizon to the outgoing mode.

to the orifice (or to the singularity at $r=0$, if the orifice is infinitely small) without any singularity at the horizon. The classical trajectories of these particles are

$$p_r(r) = -E_{\rm rest}/[c - v(r)] < 0. \tag{7}$$

The energies of these particles as viewed by the comoving observer are also positive: $E_{\rm com}(r) = -cp_r(r) = E_{\rm rest}(c/c - v(r)) > 0$.

Another branch $E_{\rm rest} = (v(r)+c)p_r$ in Fig. 3 contains two disconnected pieces describing the particle propagating from the horizon in two opposite directions:

$$r > r_h: \quad p_r(r) = E_{\rm rest}/[c + v(r)] > 0, \quad E_{\rm com}(r) = cp_r(r) > 0, \tag{8}$$

$$r < r_h: \quad p_r(r) = E_{\rm rest}/[c + v(r)] < 0, \quad E_{\rm com}(r) = cp_r(r) < 0. \tag{9}$$

Equation (8) describes the outgoing particles — the particles propagating from the horizon to the exterior. The energy of these particles is positive in both frames, comoving and rest. Equation (9) describes the propagation of particles from the horizon to the orifice (or to the singularity). Though for the rest-frame observer the energy of these particles is positive, these particles, which live within the horizon, belong to the Minkowski vacuum in the comoving frame.

The classical trajectory in Eqs. (8) and (9) is thus disrupted at the horizon. There is, however, a quantum mechanical transition between the two pieces of the branch: quantum tunneling. The tunneling amplitude can be found in semiclassical approximation by shifting the contour of integration to the complex plane:

$$w \sim \exp(-2S), \tag{10}$$

$$S = {\rm Im} \int dr \;\; p_r(r) = \frac{\pi E_{\rm rest}}{|v'(r)|_{r=r_h}}. \tag{11}$$

This means that the wave function of any particle in the Minkowskii vacuum inside the horizon contains an exponentially small part describing the propagation from the horizon to infinity. This corresponds to the radiation from the Minkowski vacuum in the presence of the event horizon. The exponential dependence of the probability on the quasiparticle energy $E_{\rm rest}$ suggests that this radiation looks like thermal radiation. The corresponding temperature, the Hawking temperature, is

$$T_{\rm Hawking}=\hbar|v'(r)|_{r=r_h}/2\pi. \tag{12}$$

The radiation leads to the quantum friction: the linear momentum of the flow decreases with time.This occurs continuously until the superfluid Minkowski vacuum between the horizons is completely exhausted and the superfluid state breaks down. This leads to a phase slip event, after which the number N_3 of circulation quanta of superfluid velocity trapped by the torus is reduced. This process will repeatedly continue until the two horizons merge.

Negative temperature for the chiral 1+1 fermions

It should be mentioned that there is an example in which a negative temperature behind the horizon is well defined. This is the case of the 1+1-dimensional chiral fermions living in the vortex core. For such fermions there is only one branch, $E=\omega_0(\phi)L$. Here L is the angular momentum of the quasiparticle in the vortex core, and $\omega_0(\phi)$ is the so-called minigap, which for a nonaxisymmetric vortex core depends on the azimuthal angle ϕ. This is equivalent to our branch $E=c(r)p_r$ in the nonmoving liquid if the speed of light is coordinate-dependent. If the vortex core is rotated with angular velocity Ω, the energy spectrum is time-dependent in the laboratory frame $E=\omega_0(\phi-\Omega t)L$. But it is time-independent in the frame corotating with the vortex core, where the energy is well defined: $E_{\rm corotating}=(\omega_0(\phi)-\Omega)L$; this is equivalent to our branch $E_{\rm rest}=(v+c)p_r$ in the rest frame. The horizon can occur if the vortex core rotates with sufficiently large angular velocity, such that Ω exceeds the minimal value of the minigap.[6] In this case, since there is only one branch of the fermions, the negative temperature is well defined. Behind the horizon the Minkowski vacuum, which is the state with $T=+0$ now in the laboratory frame (Fig. 4a), is really the state with $T=-0$ in the frame corotating with the core (Fig. 4b) and vice versa; the state with $T=-0$ in the laboratory frame is the state with $T=+0$ in the corotating frame.

Such symmetry between the vacua for the 1+1 chiral fermions suggests that there can also be symmetry between the nonzero positive and negative temperatures. Let us now take the Hawking radiation into account and suppose that at infinity there is a heat bath with the temperature $T=T_{\rm Hawking}$. Then the heat flux from infinity exactly compensates the radiation from the horizon. In such a metastable steady state the distribution of quasiparticles behind the horizon would correspond to a nonzero negative temperature $T=-T_{\rm Hawking}$.

Discussion

The above construction in Fig. 1b allows us (at least in principle) to obtain the event horizon in the quasi-stationary regime, when the main source of non-stationarity is the dissipation coming from the Hawking radiation. As to the practical implementation, there are, of course, many technical problems to be solved.

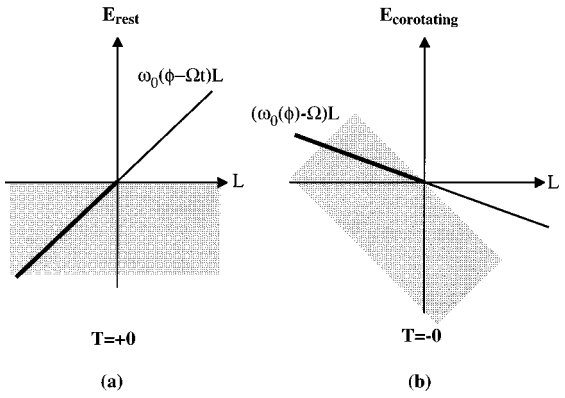

FIG. 4. Energy spectrum of fermionic quasiparticles in the vortex core. a: $\Omega=0$ corresponds to the nonrotating vortex. The spectrum is linear in the angular momentum L; $\omega_0(\phi)$ is the minigap, which depends on the angle ϕ if the core is not axisymmetric. The states with negative L are occupied. If the vortex core is rotating with angular velocity Ω, then in the laboratory frame the minigap depends on time. b: The spectrum is well defined in the coordinate frame corotating with the core. Here the spectrum is shown in the region of ϕ where $\omega_0(\phi)<\Omega$, i.e., behind the horizon. If the initial state is the Minkowski vacuum, it is seen by the corotating observer as the state with $T=-0$.

The situation in which the supercritical flow is described in terms of the event horizon and Hawking radiation occurs only for the low-energy fermions, whose spectrum is ''relativistic.'' Howeverever, the analog of the event horizon persists even in the case of the ''nonrelativistic'' spectrum: the ''horizon'' occurs at the surface where the local superflow becomes supercritical, i.e., the superfluid velocity exceeds the Landau critical velocity. Thus it is necessary to extend the consideration of the Hawking type radiation to higher energies, where the other mechanisms for the decay of the supercritical superflow can become important.

For example, the radiated particles with energies outside the ''relativistic'' region can be Andreev-scattered back to the black hole. Thus both partners (particle and hole) of the Hawking radiation will remain within the horizon. This recalls the phenomenon of partial reflection of particles with $E>m$ and total reflection of particles with $E<m$, created by a black hole, back to the black hole horizon by an effective potential outside the black hole, created by the spacetime curvature. In the former case, this partial reflection results in the well-known ''greybody'' property of the Hawking thermal radiation at spatial infinity (see, e.g., Ref. 7). For a discussion of the second case, when there is no radiation at spatial infinity, see, e.g., Ref. 8. In our case the reflection back to the hole is due not to a potential barrier outside the black hole but rather to the ''curvature'' of the quasiparticle spectrum.

This would mean that the particle creation in a high ''gravity'' field can disturb the ''Minkowski'' quantum vacuum inside the horizon without any radiation to the exterior. In principle such pair creation inside the horizon can be more important for the dissipation of the ''superluminal'' (supercritical) superflow than the Hawking radiation.

I thank Ted Jacobson and Alexei Starobinsky for illuminating discussions. This work was supported by the Russian Fund for Fundamental Research Grant No. 96-02-

16072 and by the European Science Foundation network on ''Topological Defects in Cosmology and Condensed Matter Physics.''

[1] W. G. Unruh, Phys. Rev. Lett. **46**, 1351 (1981).
[2] M. Visser, ''Acoustic black holes,'' http://xxx.lanl.gov/abs/gr-qc/9901047, to appear in *Proceedings of the 1998 Peniscola Summer School on Particle Physics and Cosmology*, Springer-Verlag.
[3] T. A. Jacobson and G. E. Volovik, Phys. Rev. D **58**, 064021 (1998); JETP Lett. **68**, 874 (1998).
[4] M. Visser, Class. Quantum Grav. **15**, 1767 (1998).
[5] N. B. Kopnin and G. E. Volovik, JETP Lett. **67**, 140 (1998).
[6] N. B. Kopnin and G. E. Volovik, Phys. Rev. B **57**, 8526 (1998).
[7] I. D. Novikov and V. P. Frolov, *Physics of Black Holes*, Kluwer Academic, Dordrecht, 1989.
[8] L. A. Kofman, Phys. Lett. F **87**, 281 (1982).

Published in English in the original Russian journal. Edited by Steve Torstveit.